

Multi-enzyme complexes on DNA scaffolds capable of substrate channelling with an artificial swinging arm

Jinglin Fu^{1,2†‡*}, Yuhe Renee Yang^{1,3§}, Alexander Johnson-Buck⁴, Minghui Liu^{1,3}, Yan Liu^{1,3}, Nils G. Walter⁴, Neal W. Woodbury^{2,3} and Hao Yan^{1,3*}

Swinging arms are a key functional component of multistep catalytic transformations in many naturally occurring multi-enzyme complexes¹. This arm is typically a prosthetic chemical group that is covalently attached to the enzyme complex via a flexible linker, allowing the direct transfer of substrate molecules between multiple active sites within the complex^{2–4}. Mimicking this method of substrate channelling outside the cellular environment requires precise control over the spatial parameters of the individual components within the assembled complex. DNA nanostructures can be used to organize functional molecules with nanoscale precision^{5–7} and can also provide nanomechanical control^{8–11}. Until now, protein-DNA assemblies¹² have been used to organize cascades of enzymatic reactions by controlling the relative distance and orientation of enzymatic components^{13–16} or by facilitating the interface between enzymes/cofactors and electrode surfaces^{17,18}. Here, we show that a DNA nanostructure can be used to create a multi-enzyme complex in which an artificial swinging arm facilitates hydride transfer between two coupled dehydrogenases. By exploiting the programmability of DNA nanostructures, key parameters including position, stoichiometry and inter-enzyme distance can be manipulated for optimal activity.

The general design of the swinging-arm nanostructure complex is shown in Fig. 1a, where a two-enzyme cascade consisting of glucose-6-phosphate dehydrogenase (G6pDH)¹⁹ and malic dehydrogenase (MDH)²⁰ is displayed on a DNA double-crossover (DX) tile scaffold²¹ (for the DNA sequences for all structures used in this study see Supplementary Figs 1–7). G6pDH catalyses the oxidation of glucose-6-phosphate and the reduction of NAD⁺ to NADH. Subsequently, MDH catalyses the reduction of oxaloacetate to malic acid using the NADH produced by G6pDH. To facilitate channelling of NADH between G6pDH and MDH, an NAD⁺-functionalized poly(T)₂₀ oligonucleotide was attached to the DNA tile surface halfway between G6pDH and MDH (see Supplementary Figs 8–21 for a detailed description of the conjugation, assembly and purification of the nanostructured complex). Figure 1b presents the results of a native polyacrylamide gel electrophoresis (PAGE) analysis of the assembled enzyme complex, together with various subcomplexes. Both the gel results and a chromatogram obtained using size-exclusion chromatography (Supplementary Fig. 21) demonstrate assembly of the G6pDH-NAD⁺-MDH swinging arm cascade with >80% yield. The assembled mixture was further purified by size exclusion chromatography for enzyme activity

assays. Assembly of the complete complex was also visualized by atomic force microscopy (AFM) (Fig. 1c; see Supplementary Fig. 57 for larger-view images), with the presence of the enzymes on the structure confirmed by differences in height ('brightness') compared to the surface of the DNA tile.

To first explore the parameters and understand the kinetics and mechanism of the restricted diffusion mediated by the single-stranded DNA (ssDNA) swinging arm, we developed a simplified model system (Supplementary Fig. 22). In this model, a Cy3 reporter dye takes the place of NAD⁺ on the single-stranded poly(T)₂₀ arm, and a BHQ fluorescence quencher (Black Hole Quencher, Biosearch Technologies) and a Cy5 energy transfer acceptor dye replace one or both enzymes on selected probe positions surrounding the swinging arm (Fig. 2a). An oligonucleotide sequence (5'-ATA GTG AAA) was extended from the 5' end of the poly(T)₂₀ sequence and positioned halfway between the quencher and the acceptor, allowing the arm to transiently hybridize to the probes that each bear the complementary sequence (5'-TTT CAC TAT) in analogy to the binding of NAD⁺/NADH to the dehydrogenases. The diffusive transport mediated by the swinging arm was then monitored by single-molecule fluorescence resonance energy transfer (smFRET) between the attached reporter (Cy3) and either the quencher (BHQ, obliterating the reporter fluorescence) or the acceptor (Cy5, yielding a distinct red fluorescence signal) using total internal reflection fluorescence microscopy, as previously described²². Typical smFRET time traces are shown in Fig. 2a, where the fluorescence signal alternates between Cy3-BHQ quenching and Cy3-Cy5 energy transfer, indicating that the poly(T)₂₀ arm is swinging between the two probes and transiently hybridizing to them, thus confirming its local diffusive transport. The absence of observable low-FRET intermediates (Cy3 signal only) indicates that the transient movement of the swinging arm between the two bound states occurs much more rapidly than the 100 ms time resolution of our single-molecule measurements (see Supplementary Figs 22–25 for detailed smFRET analysis).

To characterize the distance dependence of the diffusive transport and binding mediated by the swinging arm using smFRET, we chose a design in which a single Cy5-labelled capture probe was placed at one of three topologically accessible distances from the Cy3-labelled arm: 7 nm (21 base pairs), 14 nm (42 base pairs) and 21 nm (63 base pairs). As shown in Fig. 2b, the most efficient hybridization to the capture probe was observed at 7 nm, where ~94% of all swinging arms were associated with the Cy5 probe at

¹Center for Molecular Design and Biomimicry, Biodesign Institute at Arizona State University, Tempe, Arizona 85287, USA, ²Center for Innovations in Medicine, Biodesign Institute at Arizona State University, Tempe, Arizona 85287, USA, ³Department of Chemistry and Biochemistry, Arizona State University, Tempe, Arizona 85287, USA, ⁴Single Molecule Analysis Group, Department of Chemistry, University of Michigan at Ann Arbor, Ann Arbor, Michigan 48109, USA. [†]Present address: Department of Chemistry, Center for Computational and Integrative Biology, Rutgers University at Camden, Camden, New Jersey 08102, USA. [‡]These authors contributed equally to this work. *e-mail: hao.yan@asu.edu; jinglin.fu@rutgers.edu

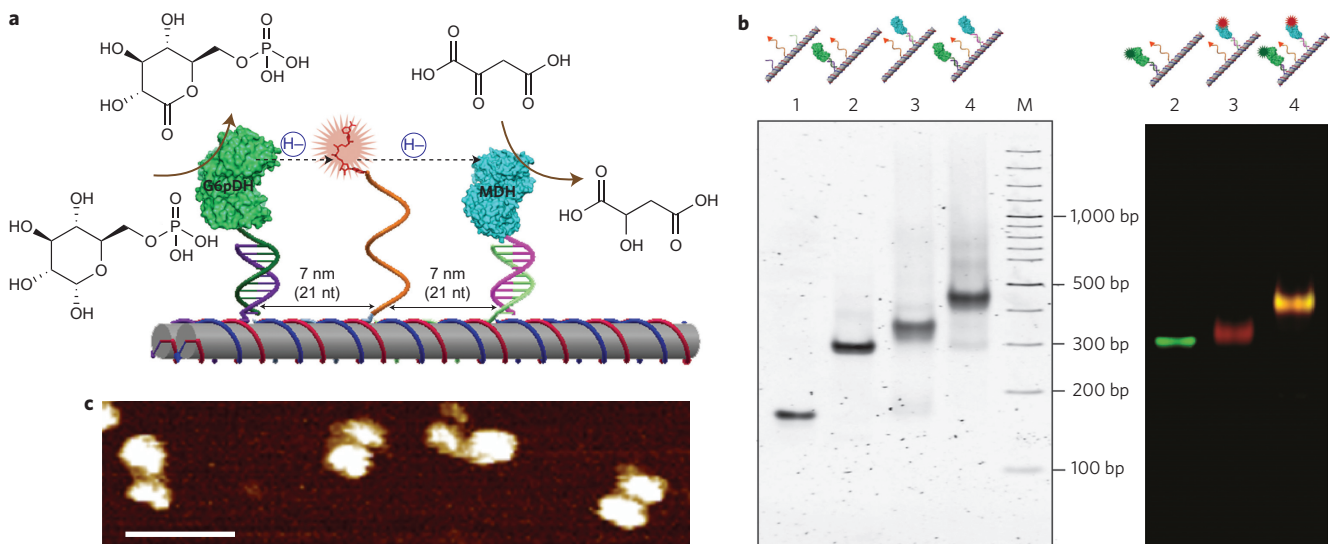


Figure 1 | Design and characterization of an NAD⁺-modified swinging arm providing restricted diffusion of NAD⁺/NADH between two dehydrogenases.

a, Schematic of the nanostructured complex consisting of G6pDH and MDH organized on a DNA DX tile. The NAD⁺-modified single-stranded poly(T)₂₀ is positioned halfway between the two enzymes, facilitating the transfer of hydrides. **b**, Left: Native PAGE (3%) characterization of the assembled swinging-arm enzyme complex: lane 1, DNA tile with NAD⁺-modified arm; lane 2, G6pDH-NAD⁺ semi-swinging arm; lane 3, MDH-NAD⁺ semi-swinging arm; lane 4, fully assembled G6pDH-NAD⁺-MDH swinging-arm structure. Right: Fluorescence gel image of an Alexa 555-labelled G6pDH-NAD⁺ structure (lane 2), an Alexa 647-labelled MDH-NAD⁺ structure (lane 3) and a dual-colour image of a G6pDH (AlexaFluor-555-labelled)-NAD⁺-MDH (AlexaFluor-647-labelled) swinging-arm structure (lane 4). M, double-stranded DNA ladder. **c**, AFM image of the G6pDH-NAD⁺-MDH swinging-arm structures. Scale bar, 50 nm.

equilibrium (leading to high FRET). As the distance increased, the equilibrium fraction of captured swinging arms decreased to ~58% at 14 nm and only ~10% at 21 nm (Fig. 2b and Supplementary Fig. 26) as a result of the less efficient binding mediated by a locally tethered arm at longer distances. Furthermore, titrating in free, unlabelled ssDNA (to directly compete with the swinging arm for hybridization to the capture probe) allowed us to estimate the effective local concentration of the swinging arm as ~250 μM for the 7 nm design and ~2.7 μM for the 14 nm construct (Supplementary Figs 27 and 28), demonstrating a steep distance dependence consistent with our predictions using a recent coarse-grained model²³ of the poly(T)₂₀ arm (Supplementary Fig. 29 and Supplementary Table 4). Based on these observations we predicted that our enzyme complexes would show a similar distance-dependent activity.

We next evaluated the ability of a NAD⁺-modified swinging arm to enhance dehydrogenase activity as a function of distance in complexes containing one enzyme coupled to a single NAD⁺ arm (Fig. 2c,d). The activity of each of the two enzymes was measured individually in bulk solution for the three swinging arm–enzyme distances (7, 14 and 21 nm) using a phenazine methosulphate-catalysed resazurin fluorescence assay (for more details see Supplementary Figs 30 and 33–35)^{8,24}. As predicted, the 7 nm distance resulted in the highest activity for both G6pDH and MDH. At this distance from the NAD⁺-modified swinging arm, the G6pDH-NAD⁺ assembly showed an activity enhancement of ~25-fold compared to an enzyme system in the presence of the same concentration (100 nM) of freely diffusing NAD⁺ (all freely diffusing NAD⁺ in the main text refers to aminoethyl-modified NAD⁺; Supplementary Fig. 14). A spacing smaller than 7 nm is predicted to result in steric crowding between adjacent proteins, thereby reducing the assembly yield (Supplementary Fig. 56). To examine possible effects of the relative orientations of the enzyme and swinging arm, we varied the angle between the NAD⁺-modified arm and the enzyme attachment site while maintaining an arm–enzyme distance of ~6–8 nm (Fig. 2e,f), and found the highest activity when the arm was attached to the ‘top’ surface of the

DNA nanostructure, approximately parallel to the enzyme (Supplementary Figs 36–39).

Based on an evaluation of the above model systems, a G6pDH-NAD⁺-MDH swinging-arm structure was constructed with the NAD⁺-modified arm positioned centrally, 7 nm from either enzyme in a parallel geometry. In Fig. 3a, the activity of this complete two-enzyme nanostructure is compared to that of partially assembled structures including a G6pDH-MDH assembly with freely diffusing NAD⁺, a G6pDH-NAD⁺ arm assembly with freely diffusing MDH, and an MDH-NAD⁺ arm assembly with freely diffusing G6pDH. For the same total NAD⁺ and enzyme concentrations (100 nM each), the activity of the complete swinging-arm structure is ~90-fold higher than that obtained using the same two-enzyme complex but with freely diffusing NAD⁺. Semi-swinging arm complexes with only one enzyme attached (G6pDH-NAD⁺ or MDH-NAD⁺) and the other enzyme freely diffusing in solution also resulted in somewhat higher activity than the two-enzyme complex without an NAD⁺-modified arm (~14-fold for G6pDH-NAD⁺ and ~4-fold for MDH-NAD⁺), but were still considerably less active than the complete G6pDH-NAD⁺-MDH enzyme cascade. The effective local NAD⁺ concentration for G6pDH-NAD⁺-MDH was determined to be ~20 μM by titrating free NAD⁺ into the G6pDH-MDH assembly until the activity was equivalent to that of the G6pDH-NAD⁺-MDH assembly (Fig. 3b; see Supplementary Figs 40–43 for detailed raw data). Notably, the effective local concentration of the NAD⁺-coupled swinging arm determined by enzyme catalysis (~20 μM at 7 nm) is significantly lower than the swinging arm concentration estimated from competitive hybridization in the model system described above (~250 μM at 7 nm in Supplementary Fig. 28). We suggest that this difference may be due to the stricter orientational and sterical constraints associated with the binding of tethered NAD⁺ to the active site of a nearby (anchored) enzyme. It is also possible that some enzymes or cofactors may be paired together permanently with inactive partners on the swinging-arm nanostructures and hence be unable to form an active complete cascade (for more discussion see Supplementary Fig. 43). Note that the effective local

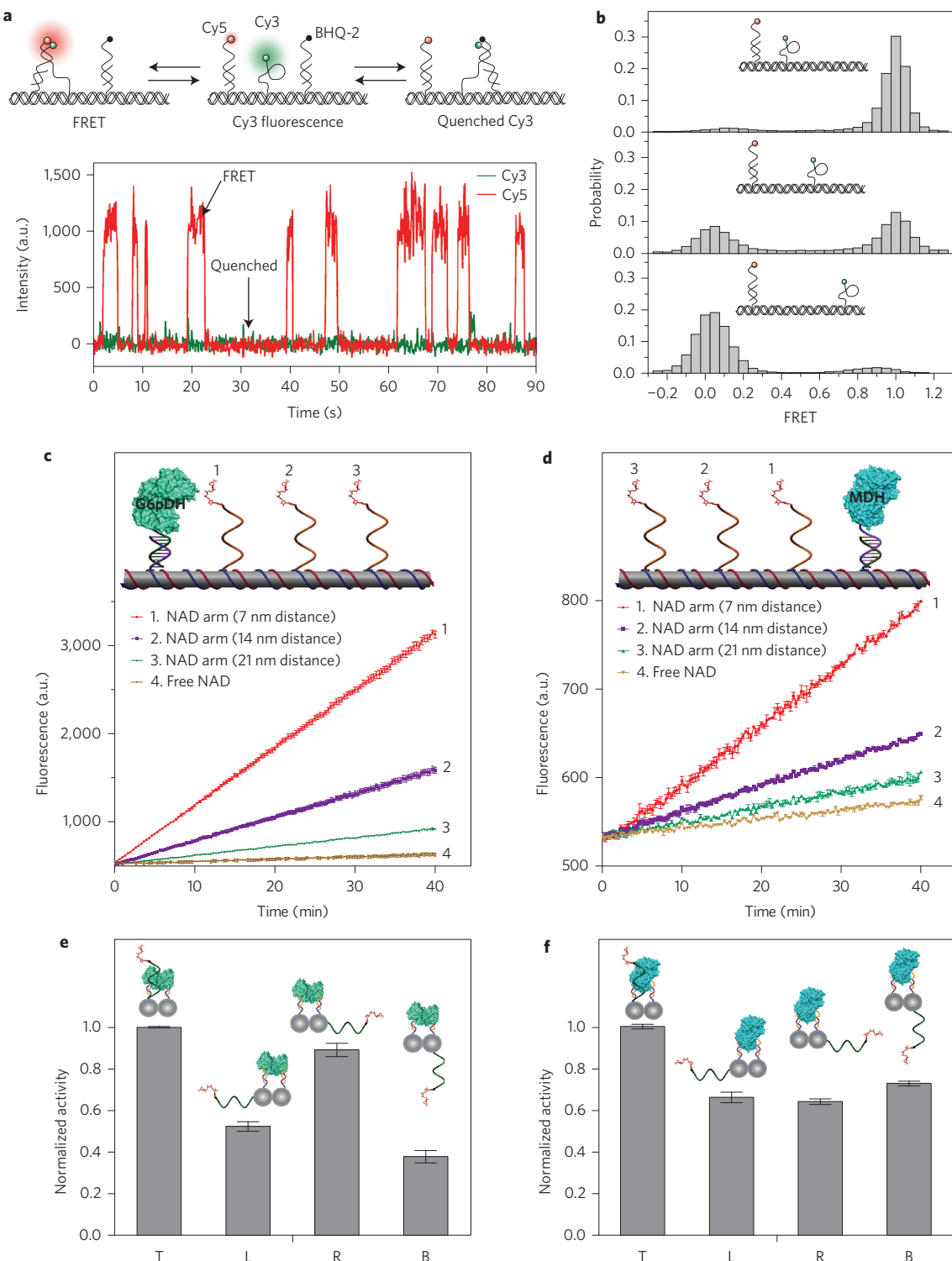


Figure 2 | Characterization of local diffusive transport by the poly(T)₂₀ swinging arm. **a**, smFRET characterization of the restricted diffusion of a single-stranded poly(T)₂₀ arm between two DNA probes anchored at either side of the structure. Top: Cy3-labelled poly(T)₂₀ with a 5' sticky end extension assembled between two capture probes that are modified with Cy5 (energy acceptor) and BHQ-2, respectively, at ~ 7 nm from the anchor position of the arm. The Cy3-Cy5 FRET signal (red emission) is observed when the arm swings and binds to the Cy5-labelled capture probe, while a Cy3-BHQ interaction quenches the fluorescence when the arm swings and binds to the BHQ-labelled capture probe. Bottom: smFRET monitoring of the swinging poly(T)₂₀ arm with alternating Cy3-BHQ quenching and Cy3-Cy5 FRET events. Charge-coupled device integration time = 0.1 s. **b**, smFRET characterization of distance-dependent hybridization of the poly(T)₂₀ arm, with 7 nm (top), 14 nm (middle) and 21 nm (bottom) enzyme-NAD-modified arm distances. **c,d**, Distance-dependent enzyme activity for complexes in which the NAD⁺-modified arm is coupled to either G6pDH (c) or MDH (d) with enzyme-NAD⁺-modified arm distances of 7 nm, 14 nm and 21 nm. **e,f**, Orientation-dependent enzyme activity for complexes in which the NAD⁺-modified arm is coupled to either G6pDH (e) or MDH (f) at various angles between the enzyme and arm attachment sites on the DNA scaffold. Angles of parallel (or $\sim 0^\circ$, T), left (or $\sim 90^\circ$, L), right (or $\sim 90^\circ$, R) and bottom (or $\sim 180^\circ$, B) were investigated. Error bars were generated as the standard error of the mean from at least three replicates.

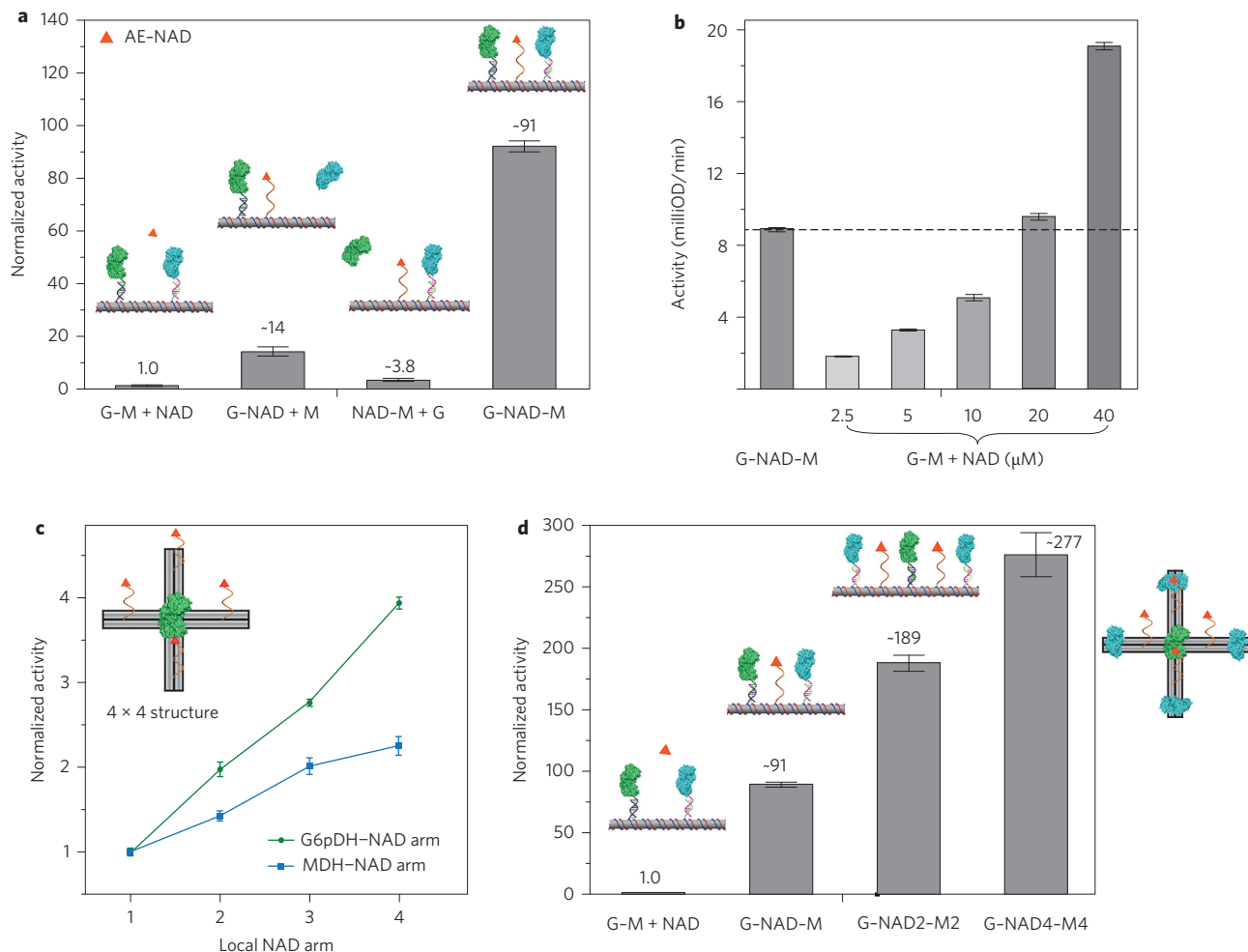


Figure 3 | Characterization of enzymatic activity in the G6pDH-NAD⁺-MDH swinging-arm structures. **a**, Normalized overall pathway activities for G6pDH-MDH assembly with free NAD⁺ (G-M + NAD), G6pDH-NAD⁺ semi-swinging arm with free MDH (G-NAD + M), MDH-NAD⁺ semi-swinging arm with free G6pDH (NAD-M + G) and the fully assembled G6pDH-NAD⁺-MDH swinging-arm structure (G-NAD-M). Total enzyme structure and NAD⁺ concentrations: each 100 nM. Substrate conditions: 1 mM glucose-6-phosphate and 1 mM oxaloacetic acid in 100 mM HEPES buffer (pH 8). **b**, Titration of the effective concentration of freely diffusing NAD⁺ into the G-M assembly with equivalent activity to the swinging-arm structure of G-NAD-M assembly: 100 nM G-M assemblies with free aminoethyl-modified NAD⁺ (AE-NAD) at 2.5, 5, 10, 20 and 40 μM . All NAD⁺ used in the assay refers to AE-NAD. The dashed line indicates the activity level of the fully assembled G-NAD-M swinging arm. **c**, Relative stoichiometric dependence of enzyme activity as the number of NAD⁺-modified arms on a 4 \times 4 DNA tile increases from 1 to 4. **d**, Improving the catalytic efficiency by adjusting the relative number of G6pDH and MDH molecules: G6pDH-MDH assembly with free NAD⁺ (G-M + NAD); G6pDH-NAD⁺-MDH swinging-arm structure (G-NAD-M); G6pDH-NAD₂⁺-MDH₂ swinging-arm structure (G-NAD₂-M₂) and G6pDH-NAD₄⁺-MDH₄ structure (G-NAD₄-M₄). Error bars were generated as the standard error of the mean from at least three replicates.

concentration of the single NAD⁺-coupled swinging arm ($\sim 20 \mu\text{M}$) is much lower than the average NAD⁺ concentration in cells ($\sim 300 \mu\text{M}$)²⁵. However, the activity of swinging-arm systems can be improved by positioning multiple NAD⁺ arms around a single enzyme, as will be discussed in the following. The activity of swinging arms may also be constructed using more stable and active biomimetic NAD⁺ analogues in the future.

In natural multi-enzyme complexes, the relative stoichiometry of the enzymes is optimized to maximize their catalytic efficiency. To this end, we investigated the dependence of enzymatic activity on the number of surrounding NAD⁺-modified swinging arms attached to a DNA-scaffolded 4 \times 4 tile (Fig. 3c)²⁶. For the G6pDH-NAD⁺ structure, the activity increased almost linearly as the number of NAD⁺-modified arms increased from one to four, indicating that G6pDH activity remains well below saturation. In contrast, the enzymatic activity of the MDH-NAD⁺ structure only improved twofold as the number of NAD⁺-

modified arms increased from one to four, suggesting that MDH is approaching activity saturation (Supplementary Figs 44–47). Kinetic measurements of isolated enzymes indicate that G6pDH has an approximately tenfold higher turnover number (k_{cat}) and an approximately eightfold larger Michaelis constant (K_m) than MDH (Supplementary Fig. 32), suggesting that the activity of multi-enzyme complexes might be further enhanced by increasing the ratio of MDH and NAD⁺ to G6pDH. We therefore engineered structures in which two MDH molecules surround a single G6pDH molecule, channelled by two NAD⁺-modified arms (G6pDH-NAD₂⁺-MDH₂), as shown in Fig. 3d. As predicted, this enzyme complex exhibited an additional approximately twofold increase in activity compared to the G6pDH-NAD⁺-MDH complex (Supplementary Figs 48 and 51). Furthermore, a complex consisting of four MDH molecules surrounding a single G6pDH molecule, channelled by four NAD⁺ arms (G6pDH-NAD₄⁺-MDH₄) showed an approximately threefold higher activity than G6pDH-

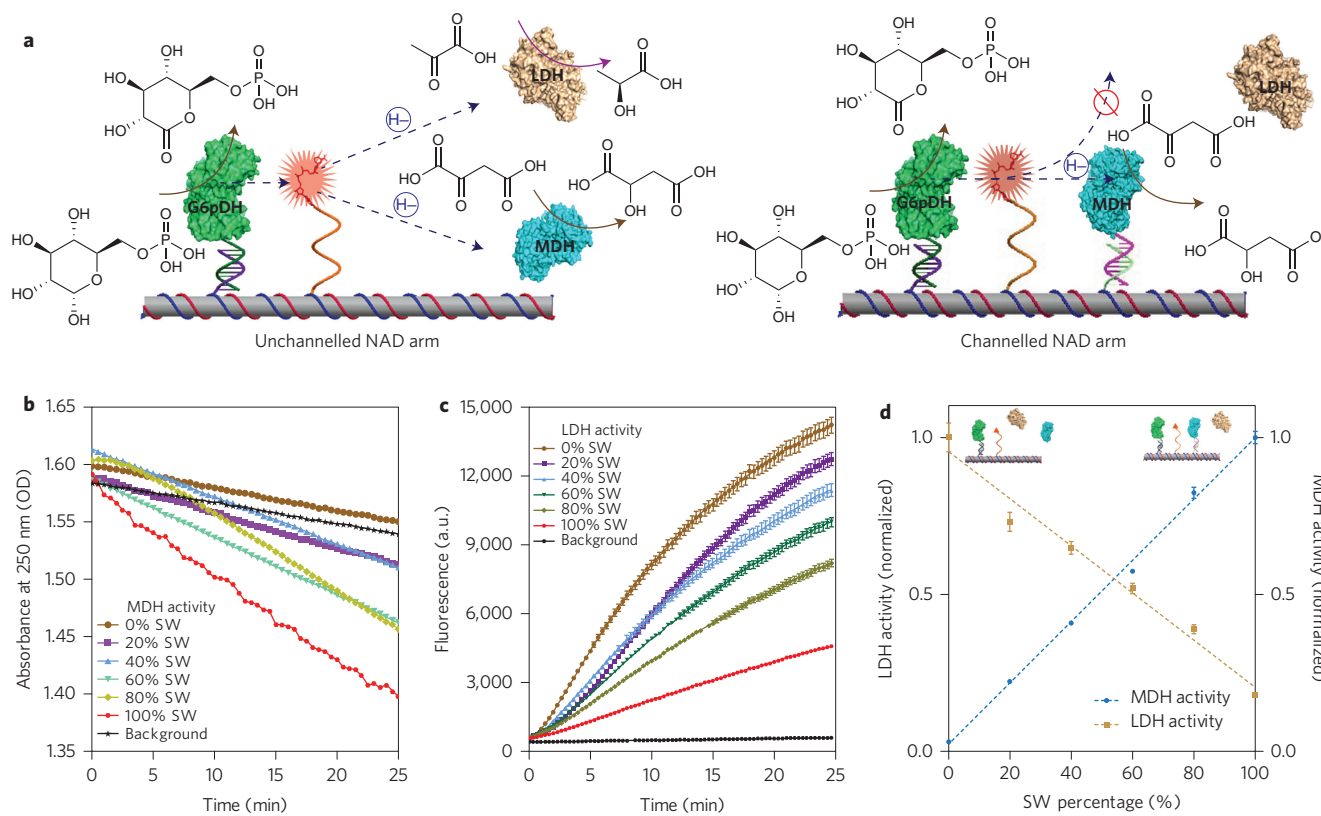


Figure 4 | Specificity of the G6pDH-NAD⁺-MDH swinging-arm structure when free LDH is introduced to compete for the NADH produced by G6pDH.

a, Schematic of the competition of free LDH with free MDH for the G6pDH-NAD⁺ semi-swinging arm (left). Schematic of free LDH with the fully assembled G6pDH-NAD⁺-MDH swinging-arm complex (right). **b**, Dependence of MDH activity on the fraction of fully assembled swinging-arm complex (SW). **c**, Dependence of LDH activity on the fraction of fully assembled swinging-arm complex. Assay conditions: 100 nM G6pDH-NAD⁺-MDH structure (total concentration including the half and fully assembled swinging-arm structures); 100 nM LDH; 1 mM glucose-6-phosphate, 1 mM oxaloacetic acid, 1 mM sodium pyruvate in 100 mM HEPES buffer (pH 8). Error bars were generated as the standard error of the mean from at least three replicates.

NAD⁺-MDH. The performance of the G6pDH-NAD⁺-MDH₄ complex is limited by the low yield (~50–60%) of correct assembly, which is possibly a consequence of steric crowding and the complexity of the design (Supplementary Figs 49–51). Attesting to their robustness, no degradation of the DNA structures was evident by PAGE analysis after 1 h of catalytic operation (Supplementary Fig. 52).

Another important advantage of an enzyme cascade with a central swinging arm is the increased reaction specificity that results from restricting the diffusion of intermediates. To explore this notion, free lactate dehydrogenase (LDH) was added to compete for NADH with the MDH on the G6pDH-NAD⁺-MDH nanostructure. The LDH is expected to consume a fraction of the NADH generated by the G6pDH, so it should interfere with the enzyme cascade, leading to decreased malic acid production (Supplementary Fig. 32). Figure 4 presents the results of using various mixtures of enzyme complexes containing different percentages of full G6pDH-NAD⁺-MDH swinging arm in competition with free LDH for NADH. As expected, for the G6pDH-NAD⁺ assembly with freely diffusing MDH and LDH we found strong competition between the two free enzymes, and the coupled activity of the G6pDH-MDH pathway was very low (Fig. 4b). As the percentage of G6pDH-NAD⁺-MDH construct was increased in the mixture (keeping the total enzyme concentrations constant), the MDH activity increased accordingly, indicating that the fully assembled G6pDH-NAD⁺-MDH complex was effectively channelling NADH from G6pDH to MDH, avoiding competition from free LDH. LDH behaved in the opposite

manner, exhibiting much lower activity as the amount of fully assembled G6pDH-NAD⁺-MDH increased (Fig. 4c). Figure 4d presents the normalized activities of MDH and LDH against the fraction of assembled complexes.

In summary, we have designed and constructed artificial swinging arm-channelled multi-enzyme complexes with NAD⁺-modified molecular arms to transfer hydrides between two dehydrogenase enzymes. The swinging arm not only significantly enhances enzymatic activity, but also affords high specificity in a complex environment. The concept of a flexible molecular-arm-channelled reaction should be applicable to the design and assembly of other multi-enzyme systems. For example, a similar approach can be used to construct swinging-arm enzyme cascades based on other reactive cofactors such as FAD, coenzyme A, adenosine triphosphate (ATP), lipoic acid, biotin or pantetheine, which are used in naturally occurring multi-enzyme complexes to carry intermediates. It is also possible to engineer artificial electron-transport chains by organizing multiple redox proteins and cofactors with swinging arms; these may find utility in biofuel production and bioenergy conversion. Artificial swinging-arm structures may also lead to new approaches for regulating the activity of enzymes by incorporating mechanisms for controlling the diffusion and motion of the arm. In a simple demonstration, we exchanged the ssDNA arm for a double-stranded DNA arm (dsDNA arm) by introducing a poly(A)₂₀ oligonucleotide into solution to hybridize with the NAD⁺-poly(T)₂₀ arm. We observed an ~30–50% decrease in enzyme activity for the enzyme complex with the dsDNA arm compared to the ssDNA arm, which Monte Carlo modelling and control

experiments with poly(A) complements of varying length suggest is due to the increased structural rigidity of a completely dsDNA arm (Supplementary Figs 53–55). The underlying DNA nanostructure scaffolds provide programmable frameworks for creating more complex enzymatic circuitry, and may find utility in the development of functional catalytic systems for the synthesis of high-value chemicals, the generation of energy, the conversion of materials, and as regulatory biological circuits for diagnostic and therapeutic applications.

Received 29 October 2013; accepted 14 April 2014;
published online 25 May 2014

References

- Perham, R. N. Swinging arms and swinging domains in multifunctional enzymes: catalytic machines for multistep reactions. *Annu. Rev. Biochem.* **69**, 961–1004 (2000).
- Mattevi, A. *et al.* Atomic structure of the cubic core of the pyruvate dehydrogenase multienzyme complex. *Science* **255**, 1544–1550 (1992).
- Jitrapakdee, S. *et al.* Structure, mechanism and regulation of pyruvate carboxylase. *Biochem. J.* **413**, 369–387 (2008).
- Zhou, P., Florova, G. & Reynolds, K. A. Polyketide synthase acyl carrier protein (ACP) as a substrate and a catalyst for malonyl ACP biosynthesis. *Chem. Biol.* **6**, 577–584 (1999).
- Seeman, N. C. Nanomaterials based on DNA. *Annu. Rev. Biochem.* **79**, 65–87 (2010).
- Fu, J., Liu, M., Liu, Y. & Yan, H. Spatially-interactive biomolecular networks organized by nucleic acid nanostructures. *Acc. Chem. Res.* **45**, 1215–1226 (2012).
- Pinheiro, A. V., Han, D., Shih, W. M. & Yan, H. Challenges and opportunities for structural DNA nanotechnology. *Nature Nanotech.* **6**, 763–772 (2011).
- Liu, M. *et al.* A DNA tweezer-actuated enzyme nanoreactor. *Nature Commun.* **4**, 2127 (2013).
- Liedl, T., Hogberg, B., Tytell, J., Ingber, D. E. & Shih, W. M. Self-assembly of three-dimensional prestressed tensegrity structures from DNA. *Nature Nanotech.* **5**, 520–524 (2010).
- Gu, H., Chao, J., Xiao, S. J. & Seeman, N. C. A proximity-based programmable DNA nanoscale assembly line. *Nature* **465**, 202–205 (2010).
- Andersen, E. S. *et al.* Self-assembly of a nanoscale DNA box with a controllable lid. *Nature* **459**, 73–76 (2009).
- Niemeyer, C. M. Semisynthetic DNA–protein conjugates for biosensing and nanofabrication. *Angew. Chem. Int. Ed.* **49**, 1200–1216 (2010).
- Erkelenz, M., Kuo, C.-H. & Niemeyer, C. M. DNA-mediated assembly of cytochrome P450 BM3 subdomains. *J. Am. Chem. Soc.* **133**, 16111–16118 (2011).
- Fu, J., Liu, M., Liu, Y., Woodbury, N. W. & Yan, H. Interenzyme substrate diffusion for an enzyme cascade organized on spatially addressable DNA nanostructures. *J. Am. Chem. Soc.* **134**, 5516–5519 (2012).
- Wilner, O. I. *et al.* Enzyme cascades activated on topologically programmed DNA scaffolds. *Nature Nanotech.* **4**, 249–254 (2009).
- Delebecque, C. J., Lindner, A. B., Silver, P. A. & Aldaye, F. A. Organization of intracellular reactions with rationally designed RNA assemblies. *Science* **333**, 470–474 (2011).
- Teller, C. & Willner, I. Organizing protein–DNA hybrids as nanostructures with programmed functionalities. *Trends Biotechnol.* **28**, 619–628 (2010).
- Piperberg, G., Wilner, O. I., Yehezkel, O., Tel-Vered, R. & Willner, I. Control of bioelectrocatalytic transformations on DNA scaffolds. *J. Am. Chem. Soc.* **131**, 8724–8725 (2009).
- Rowland, P., Basak, A. K., Gover, S., Levy, H. R. & Adams, H. J. The three-dimensional structure of glucose 6-phosphate dehydrogenase from *Leuconostoc mesenteroides* refined at 2.0 Å resolution. *Structure* **2**, 1073–1087 (1994).
- Chapman, A. D. M., Cortés, A., Dafforn, T. R., Clarke, A. R. & Brady, R. L. Structural basis of substrate specificity in malate dehydrogenases: crystal structure of a ternary complex of porcine cytoplasmic malate dehydrogenase, α-ketomalonate and tetrahydroNAD. *J. Mol. Biol.* **285**, 703–712 (1999).
- Fu, T. J. & Seeman, N. C. DNA double-crossover molecules. *Biochemistry* **32**, 3211–3220 (1993).
- Johnson-Buck, A., Nangreave, J., Jiang, S., Yan, H. & Walter, N. G. Multifactorial modulation of binding and dissociation kinetics on two-dimensional DNA nanostructure. *Nano Lett.* **13**, 2754–2759 (2013).
- Meisburger, S. P. *et al.* Polyelectrolyte properties of single stranded DNA measured using SAXS and single molecule FRET: beyond the wormlike chain model. *Biopolymers* **99**, 1032–1045 (2013).
- Candeias, L. P. *et al.* The catalysed NADH reduction of resazurin to resorufin. *J. Chem. Soc. Perkin Trans. 2* **11**, 2333–2334 (1998).
- Yang, H. *et al.* Nutrient-sensitive mitochondrial NAD⁺ levels dictate cell survival. *Cell* **130**, 1095–1107 (2007).
- Yan, H., Park, S. H., Finkelstein, G., Reif, J. H. & LaBean, T. H. DNA-templated self-assembly of protein arrays and highly conductive nanowires. *Science* **301**, 1882–1884 (2003).

Acknowledgements

This work was supported by an Army Research Office MURI award (no. W911NF-12-1-0420 to H.Y., N.G.W. and N.W.W.), a National Science Foundation grant (no. 1033222 to N.W.W. and H.Y.) and an Army Research Office grant (no. W911NF-11-1-0137 to H.Y. and Y.L.). H.Y. is supported by the Presidential Strategic Initiative Fund from Arizona State University. The authors are grateful to J. Nangreave for her help in editing the manuscript and W. Li for his assistance with the FastScan AFM.

Author contributions

J.F., H.Y. and N.W.W. conceived the concepts. J.F. and Y.Y. designed DNA nanostructures, performed the enzyme–DNA structure assembly and activity assay, and analysed data. A.J.B. performed the smFRET experiments and analysed data. M.L. performed the 4 × 4 enzyme structures experiments. J.F., A.J.B. and Y.Y. wrote the manuscript. H.Y., N.W.W., Y.L. and N.G.W. discussed the results and commented on the manuscript.

Additional information

Supplementary information is available in the online version of the paper. Reprints and permissions information is available online at www.nature.com/reprints. Correspondence and requests for materials should be addressed to H.Y. and J.F.

Competing financial interests

The authors declare no competing financial interests.

Multi-enzyme complexes on DNA scaffolds capable of substrate channelling with an artificial swinging arm

Jinglin Fu, Yuhe Renee Yang, Alexander Johnson-Buck, Minghui Liu, Yan Liu, Nils G. Walter,

Neal W. Woodbury and Hao Yan

Table of contents:

Section 1: Materials	Page S3
Section 2: Design, assembly, and characterization of DNA nanostructures	Page S4-19
Section 3: Preparation, purification, and characterization of protein-DNA conjugates	Page S20-30
Section 4: Preparation, purification, and characterization of NAD⁺-DNA conjugates	Page S31-43
Section 5: Assembly, purification, and characterization of proteins on DNA nanostructures	Page S44-46
Section 6: Single-molecule FRET (smFRET) characterization of swinging arm dynamics	Page S47-62
Section 7: Enzyme activity assay methods and Michaelis-Menten analysis	Page S63-70
Section 8: Dependence of G6pDH and MDH activity on the length, position, and orientation of the NAD⁺-modified swinging arm	Page S71-79
Section 9: Characterization of the assembly and activity of G6pDH-NAD⁺-MDH (G-NAD⁺-M) swinging arm structures and stoichiometry-optimized complexes (G-NAD₂⁺-M₂ and G-NAD₄⁺-M₄)	Page S80-101
Section 10. AFM images of the fully assembled G6PDH-NAD⁺-MDH swinging arm complex	Page S102-104
References	Page S105

Section 1: Materials

Enzymes: Glucose-6-phosphate dehydrogenase (G6pDH, *Leuconostoc mesenteroides*), malic dehydrogenase (MDH, *porcine heart*), lactate dehydrogenase (LDH, *rabbit muscle*), oxaloacetate decarboxylase (OAD, *Pseudomonas sp.*), lactate oxidase (LOX, *Pediococcus sp.*) and horseradish peroxidase (HRP) were purchased from Sigma (St. Louis, MO).

DNA strands: Single-stranded oligonucleotides, Cy3-, Cy5- and BHQ-2-labeled oligonucleotides, and 5'-amino- and 5'-thiol (C6 S-S)-modified oligonucleotides were purchased from IDT DNA (Integrated DNA Technologies, INC.). Dye-labeled oligonucleotides were HPLC-purified by the manufacturer.

Crosslinking reagents: *N*-Succinimidyl 3-(2-pyridyldithio)-propionate (SPDP) was ordered from Pierce. Disuccinimidyl suberate (DSS), N,N-Diisopropylethylamine (DIPEA), and Dimethyl sulfoxide (DMSO) were purchased from Sigma.

NAD⁺: β-Nicotinamide-N6-(2-aminoethyl) adenine dinucleotide (6AE-NAD⁺ or AE-NAD⁺) was ordered from BIOLOG (Bremen, Germany). Unmodified NAD⁺ was ordered from Sigma.

Substrates and activity assay reagents: Glucose-6-phosphate (G6p), sodium pyruvate, oxaloacetic acid (OAA), resazurin (RESA), and phenazine methosulfate (PMS) were purchased from Sigma. Amplex® Red for assaying peroxidase activity was purchased from Life Technologies.

Buffers: Phosphate buffered saline (PBS), HEPES sodium salt, Tris buffered saline (TBS), Tris base, acetic acid, EDTA, and magnesium acetate were also purchased from Sigma.

Dye-labeling reagents for proteins: AlexaFluor®555 and AlexaFluor®647 amine reactive dyes were ordered from Life Technologies.

Section 2: Design, assembly, and characterization of DNA nanostructures

1. DNA nanostructure design: The detailed sequence designs of the DNA double-crossover (DX) nanostructures are shown in Figures S1-S7. The computer programs of Tiamat, Cadnano and NanoEngineer (version 1.1.1, Nanorex INC.) were used to facilitate the structure design. To improve the assembly efficiency of protein onto the DNA tiles, two identical capture probes were displayed on the DNA scaffolds with a sequence complementary to the DNA strands conjugated to proteins.

2. Denaturing PAGE purification of oligonucleotides: Oligonucleotides purchased from IDT (Integrated DNA Technologies, INC.) were purified using denaturing polyacrylamide gel electrophoresis (PAGE). Denaturing (6–8 %) PAGE gels (8.3 M urea) were prepared at room temperature. The crude DNA strands were loaded in the wells and run for 1 to 1.5 hours at 35 °C at a constant current of 90 mA and subsequently stained with ethidium bromide (EB). The bands corresponding to the correct strand length were cut from the gel, chopped into small pieces, and incubated for 1 hour in elution buffer (500 mM ammonium acetate, 10 mM magnesium acetate, 2 mM sodium ethylenediaminetetraacetic acid, pH 8.0). The DNA strands were extracted from the gel pieces by centrifugation using a Costar Spin X filtration device (Corning, cellulose acetate membrane with 0.22 µm size). The filtrate was subjected to butanol extraction to remove the EB stain, then the DNA was ethanol precipitated, washed by ethanol and vacuum dried. The DNA strands were dissolved in nanopure water and the concentrations of the individual purified strands were measured by UV absorbance at 260 nm using the extinction coefficient provided by the manufacturer.

3. DNA nanostructure assembly: The DNA strands constituting each DNA structure were mixed in 1×TAE/Mg²⁺ buffer (40 mM Tris, 20 mM acetic acid, 2 mM EDTA and 12.5 mM magnesium acetate, pH 8.0) to reach a final concentration of 1 µM per strand, except for the NAD⁺-conjugated DNA strands, which were added to the mixture at a final concentration of 1.5 µM (with 50% excess to ensure efficient incorporation of the NAD⁺-labeled strand in the DX tile). All samples were annealed using an Eppendorf Mastercycler using the annealing protocol shown in Table S1, with the temperature decreasing from 90 °C to 72 °C over 10 min (a relatively steep gradient to avoid thermal damage to NAD⁺), decreasing from 68 °C to 24 °C over 60 min, and finally holding at 15 °C. The formation of the DNA structures was characterized by native

PAGE. Excess NAD⁺-conjugated DNA strands were removed by size-exclusion chromatography as described in Section 5.

4. Native PAGE characterization of DNA structures: 3% Native PAGE gels were prepared at room temperature and run for 2.5 to 3.5 hours at a constant voltage of 200V and subsequently stained with SYBR® Green.

5. Quantifying the concentration of the purified DX tiles and the yield of protein-DNA tile assembly: The concentrations of the purified DX tiles were measured using OD₂₆₀ based on the extinction coefficients of the DX tile estimated by summing the extinction coefficients of all the DNA strands involved (dsDNA value). The measured concentrations of the DX tiles were within 5% of the theoretical concentration, as shown in Table S2.

Table S2 also shows the estimated extinction coefficients for the different protein-DNA tile assemblies. The theoretical extinction coefficients of ssDNA and dsDNA were obtained from the web site IDT Biophysics-DNA Thermodynamics & Hybridization (<http://biophysics.idtdna.com/UVSpectrum.html>)

Temperature	Time
90 °C	1 min
88 °C	1 min
86 °C	1 min
84 °C	1 min
82 °C	1 min
80 °C	1 min
78 °C	1 min
76 °C	2 min
72 °C	2 min
68 °C	5 min
64 °C	5 min
60 °C	5 min
56 °C	5 min
52 °C	5 min
48 °C	5 min
44 °C	5 min
40 °C	5 min
36 °C	5 min
32 °C	5 min
28 °C	5 min
24 °C	5 min
15°C	hold

Table S1. Thermal annealing program for assembling all DNA nanostructures. Note: Fast process from 90°C – 72°C is performed to avoid thermal damage of NAD+.

Structures	Theoretical ϵ_{260} ($M^{-1} cm^{-1}$)	Prepared Conc.(nM)	Measured A_{260}	Calculated conc. (nM)	Error (%)
7-nm MDH-NAD ⁺ semi-swinging arm	3735503	200	0.778	208	+ 4.1
14-nm MDH-NAD ⁺ semi-swinging arm	3735503	200	0.773	207	+ 3.5
21-nm MDH-NAD ⁺ semi-swinging arm	3735503	200	0.783	210	+ 4.8
DNA tile	3187221.6	1000	3.15	988	-1.2

Structure	Theoretical ϵ_{260} ($M^{-1} cm^{-1}$)
NAD ⁺ -DNA tile structure in Figure S1 without assembled protein	3187221.6
MDH-NAD ⁺ semi arm structure in Figure S2 with assembled MDH	3735503.2
MDH-DNA tile (structure similar to Figure S2 without NAD arm) + free NAD ⁺	3554526.8
G6pDH-NAD ⁺ semi-swinging arm structure in Figure S1 with assembled G6pDH	3785354.2
G6pDH-DNA tile (structure similar to Figure S2 but without NAD arm) + free NAD ⁺	3604377.8
G6pDH-NAD ⁺ -MDH full swinging arm in Figure S3 with assembled G6pDH and MDH	3799466.2
G6pDH-MDH assembly (structure similar to Figure S3 but without NAD arm) + free NAD ⁺	3618489.8
G6pDH-NAD ⁺ ₂ -MDH ₂ in Figure S5 with assembled G6pDH and MDH	4398701
G6pDH-NAD ⁺ ₄ -MDH ₄ in Figure S7 with assembled G6pDH and MDH	5695362

Table S2. Theoretical vs. measured concentrations and extinction coefficients of all structures used in enzyme studies. The theoretical extinction coefficients were obtained by summing the extinction coefficients of all the DNA strands involved (dsDNA value) and protein/NAD⁺ components. G6pDH: $\epsilon_{260} \sim 61594 M^{-1} cm^{-1}$; MDH: $\epsilon_{260} \sim 14112 M^{-1} cm^{-1}$; 6AE-NAD⁺: $\epsilon_{260} \sim 21000 M^{-1} cm^{-1}$ (provided by Biolog).

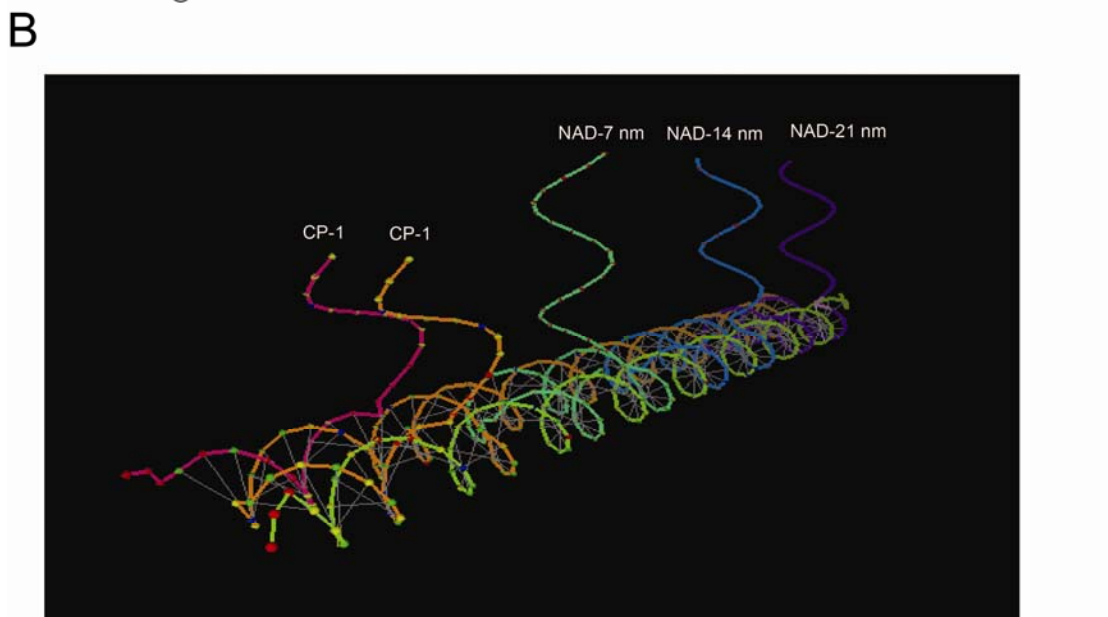
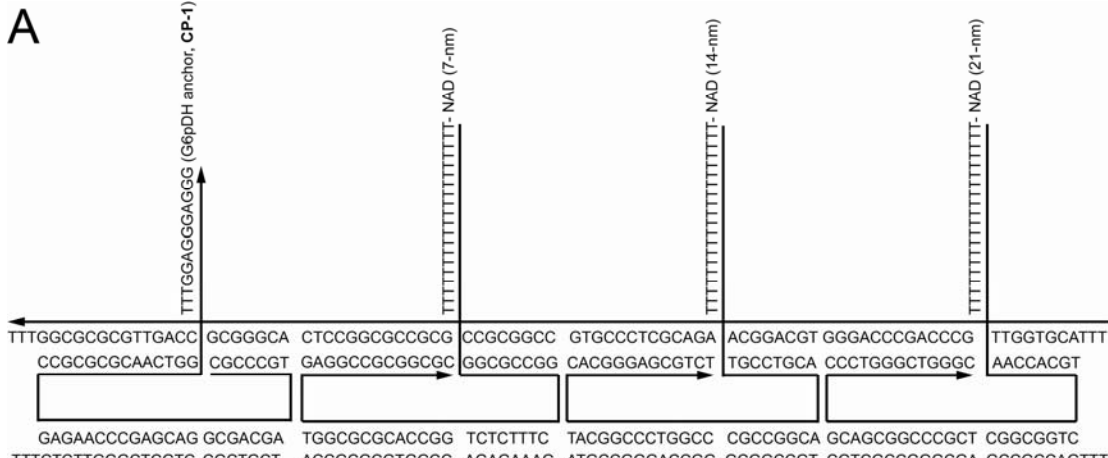
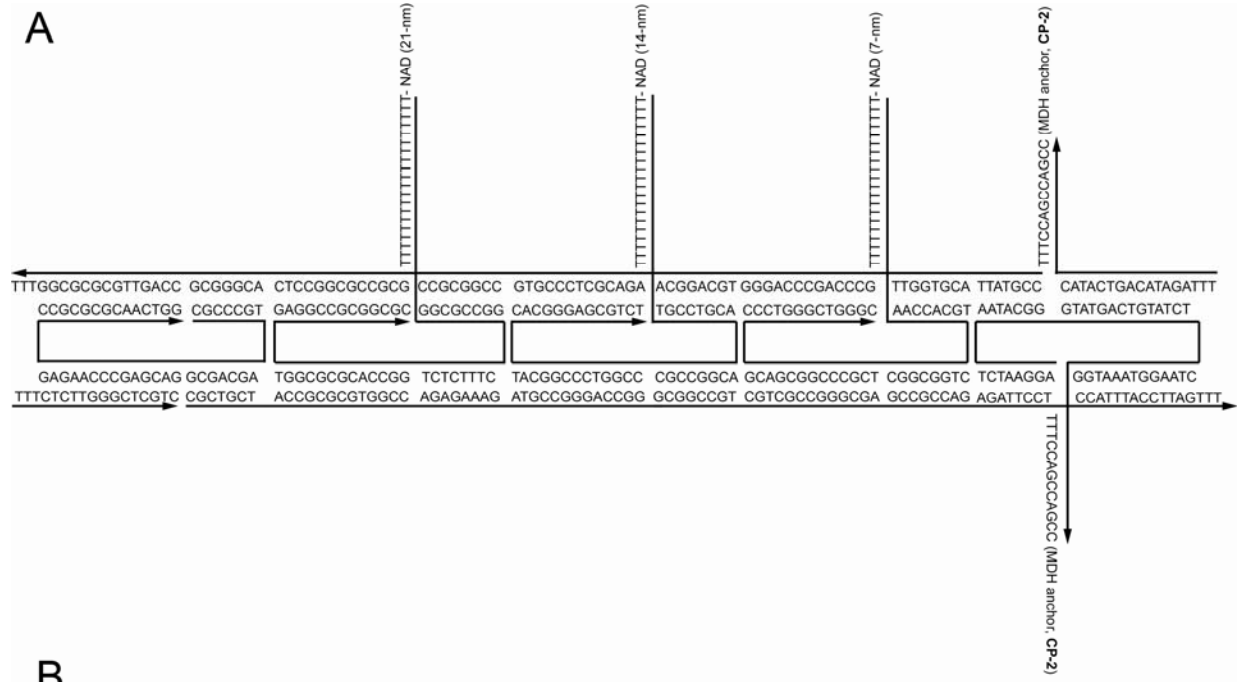


Figure S1. DNA sequence design for characterizing the distance-dependent activity of the G6pDH-NAD⁺ semi-swinging arm. **(A)** The structure incorporates two identical capture probes (CP) with the sequence **CP-1** (5'-TTTGGAGGGAGGG), which are extended from 3'-ends of the respective stands and 7 bps from the nearest crossover on the helics. The theoretical angle between the anchor point of the CP-1 probes and the surface of the DNA scaffolds is ~240°(34.5°×7), facing to the top of the surface of the DNA scaffolds. The pair of CPs are expected to cooperatively recruit one G6pDH that is labeled with two DNA molecules with the sequence **P-1** (5'-TTTTCCCTCCCTCC). For each experiment, only one of the three positions, 21, 42 or 63 bp away from the protein anchor position, is extended with the NAD⁺-modified poly(T)₂₀, which acts as the swinging arm at a distance of 7 nm, 14 nm or 21 nm from the anchor site of the enzyme. The CP-1 and poly(T)₂₀ strands are all designed to project from the same side of the DX tile. **(B)** Computer modeling (Tiamat) of DNA nanostructures: two capture probes (CP-1) and NAD⁺ arms are all facing to the same side of the structure.

A



B

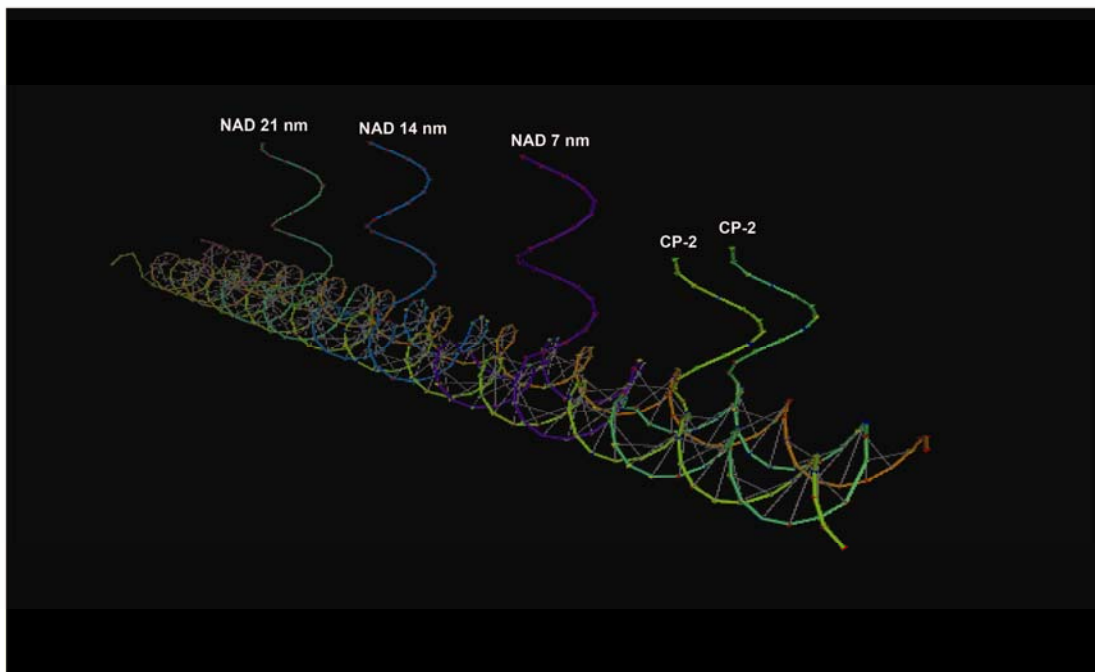


Figure S2. DNA sequence design for characterizing the distance-dependent activity of an MDH-NAD⁺ semi-swinging arm structure. (A) The structure incorporates two identical capture probes with the sequence **CP-2** (5'-TTTCCAGGCCAGCC), which are extended from 3'-ends of the respective stands and 7 bps from the nearest crossover on the helics. The theoretical angle between the anchor point of the CP-2 probes and the surface of the DNA scaffolds is ~240°(34.5°×7), facing to the top of the surface of the DNA scaffolds. The two CP-2 probes are expected to cooperatively recruit one MDH that is labeled with two DNA molecules with the sequence **P-2** (5'-TTTTGGCTGGCTGG). For each experiment, only one of the three positions, 21, 42 or 63 bp away from the MDH anchor position, is extended with the NAD⁺-modified poly(T)₂₀, which acts as the swinging arm at a distance of 7 nm, 14 nm or 21 nm away from the anchor site of the enzyme. The CP-2 and poly(T)₂₀ strands are all designed to project from the same side of the DX tile. (B) Computer modeling (Tiamat) of DNA nanostructures: two capture probes (CP-2) and NAD⁺ arms are all facing to the same side of the structure.

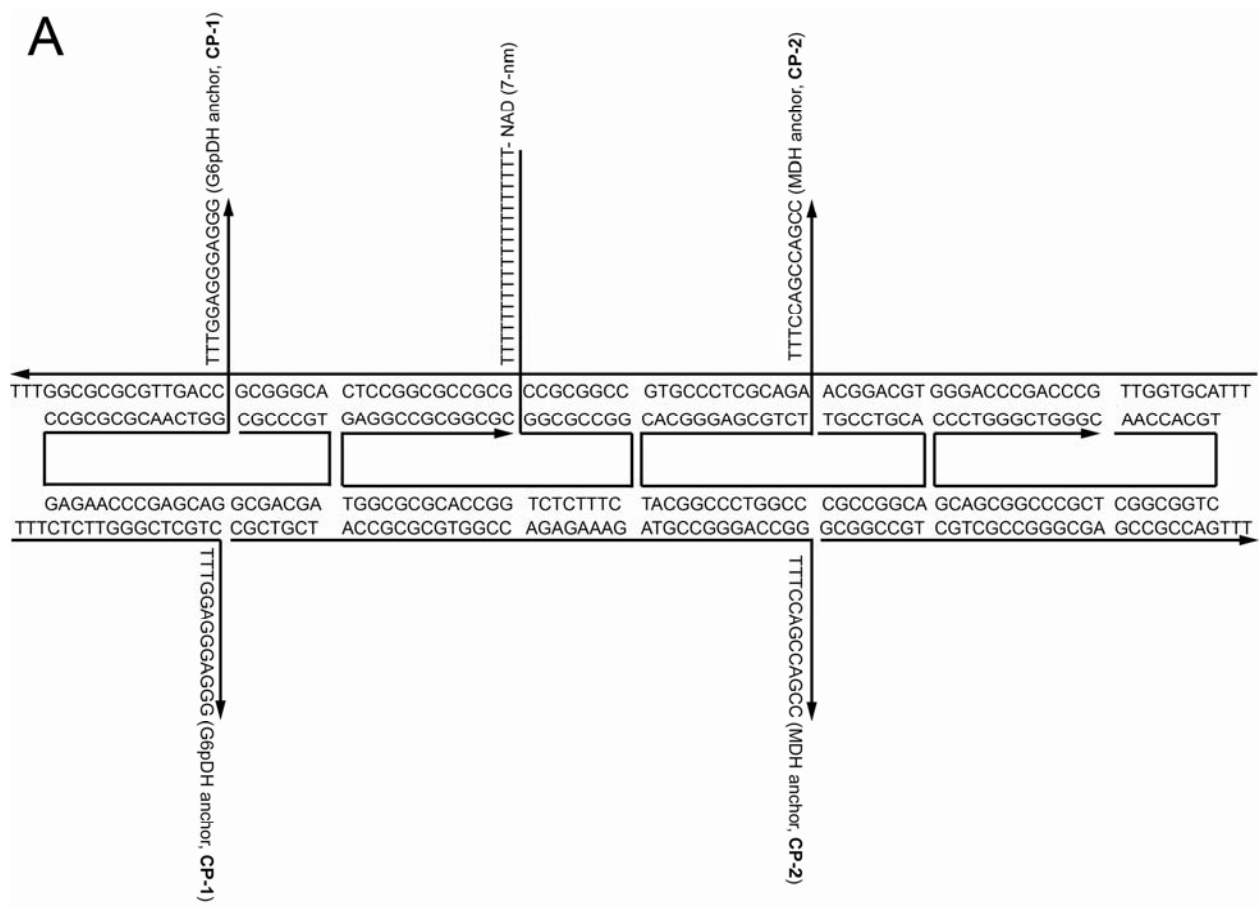
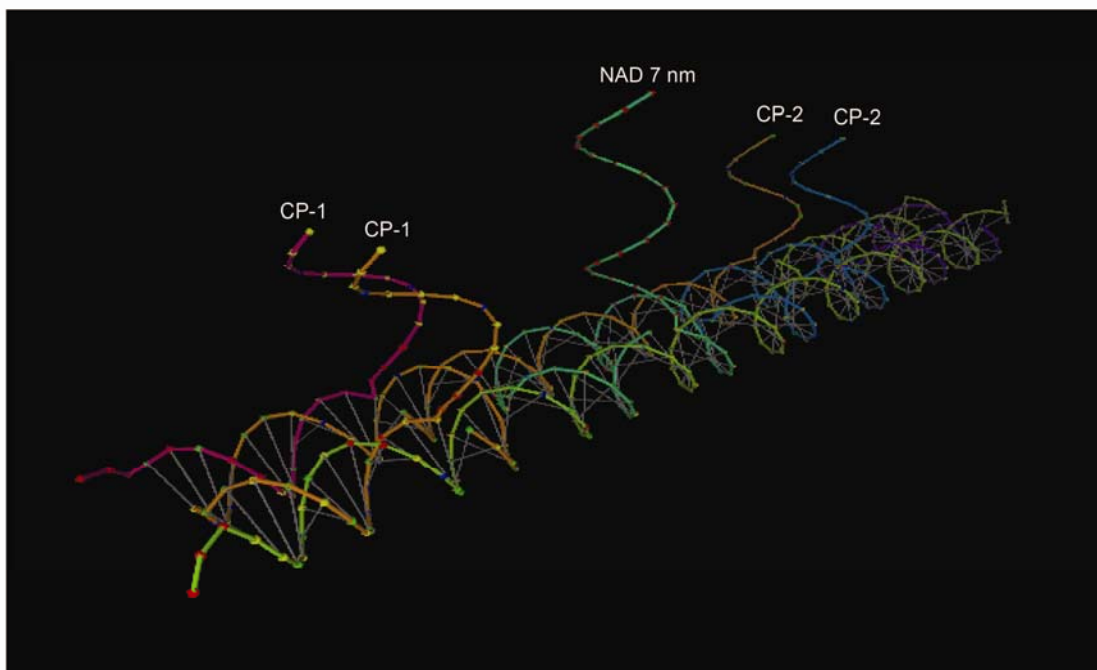
A**B**

Figure S3. DNA sequence design for the G6pDH-NAD⁺-MDH swinging arm structure. (A) The structure incorporates one pair of each of the capture probes **CP-1** (TTTGGAGGGAGGG) and **CP-2** (TTTCCACCAGGCC), which serve as anchors for G6pDH and MDH, respectively. The NAD⁺-modified poly(T)₂₀ swinging arm is located in the middle and designed to be anchored 7 nm away from the anchoring points of either enzyme. All the probes and poly(T)₂₀ strand are designed to project from the same face of the tile. (B) Computer modeling (Tiamat) of DNA nanostructures: capture probes (CP-1 and CP-2) and NAD⁺ arms are all facing to the same side of the structure.

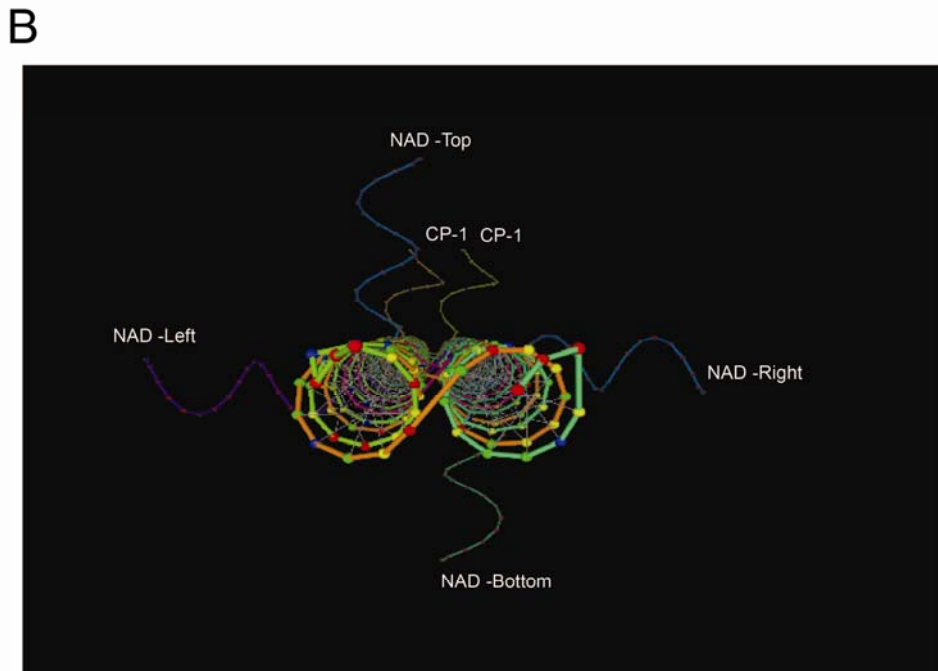
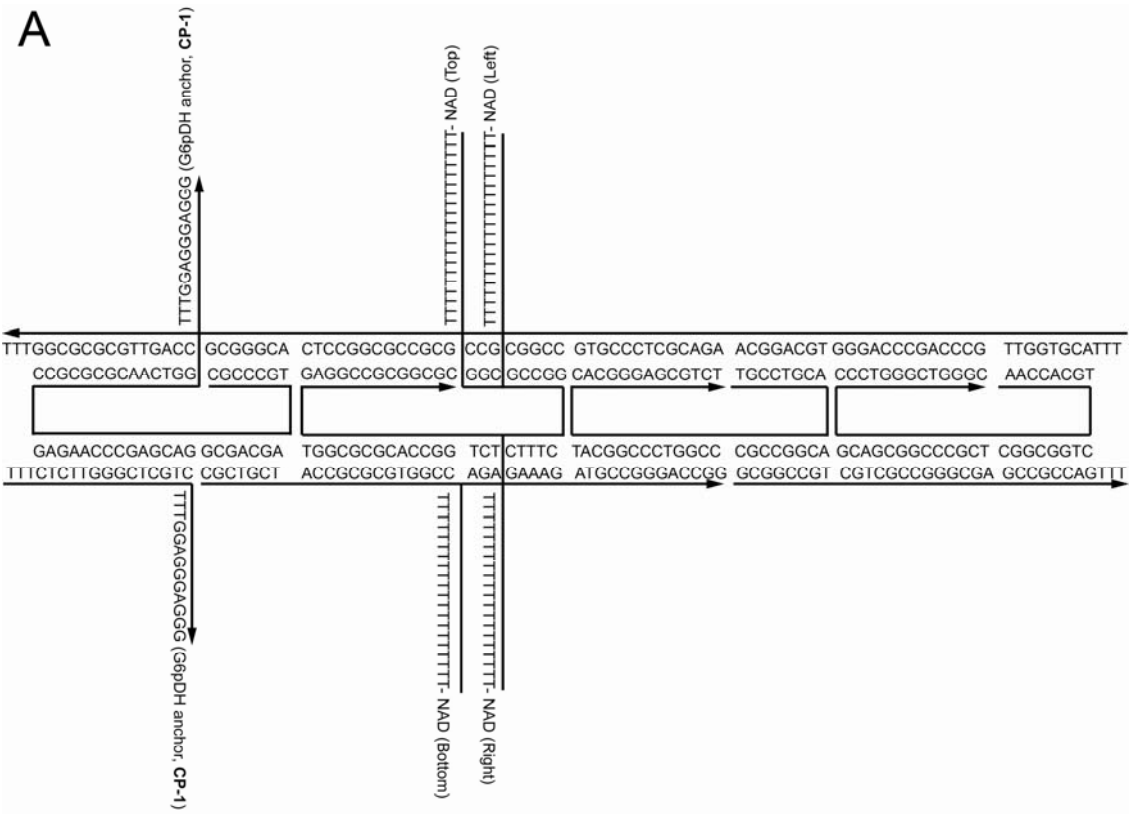


Figure S4. DNA sequence design for Orientation dependent enzyme-NAD⁺ arm activity for complexes. **(A)** The structure incorporates one pair of the capture probes **CP-1** (TTTGGAGGGAGGG), which serve as anchors for G6pDH and MDH, respectively. The NAD⁺-modified poly(T)₂₀ swinging arms are located at four different positions: **NAD-Top**, 21 bps (~ 7 nm) from CP-1 probes on the same helix, and 8 bps from the nearest crossover position. The theoretical angle between the anchor point of the NAD-Top probe and the surface of the DNA scaffolds is ~ 270°(34.5°×8), facing to the top side of the DNA scaffolds. **NAD-Left**, 24 bps (~ 8 nm) from CP-1 probes on the same helix, and 5 bps from the nearest crossover position. The theoretical angle between the anchor point of the NAD-Top probe and the surface of the DNA scaffolds is ~ 172°(34.5°×5), facing to the left side of the DNA scaffolds. **NAD-Right**, 24 bps (~ 8 nm) from CP-1 probes on the same helix, and 5 bps from the nearest crossover position. The theoretical angle between the anchor point of the NAD-Right probe and the surface of the DNA scaffolds is ~ -172°(-34.5°×5), facing to the right side of the DNA scaffolds. **NAD-Bottom**, 21 bps (~ 7 nm) from CP-1 probes on the same helix, and 8 bps from the nearest crossover position. The theoretical angle between the anchor point of the NAD-Bottom probe and the surface of the DNA scaffolds is ~ -240°(-34.5°×7), facing to the bottom side of the DNA scaffolds. **(B)** Computer modeling (Tiamat) of DNA nanostructures.

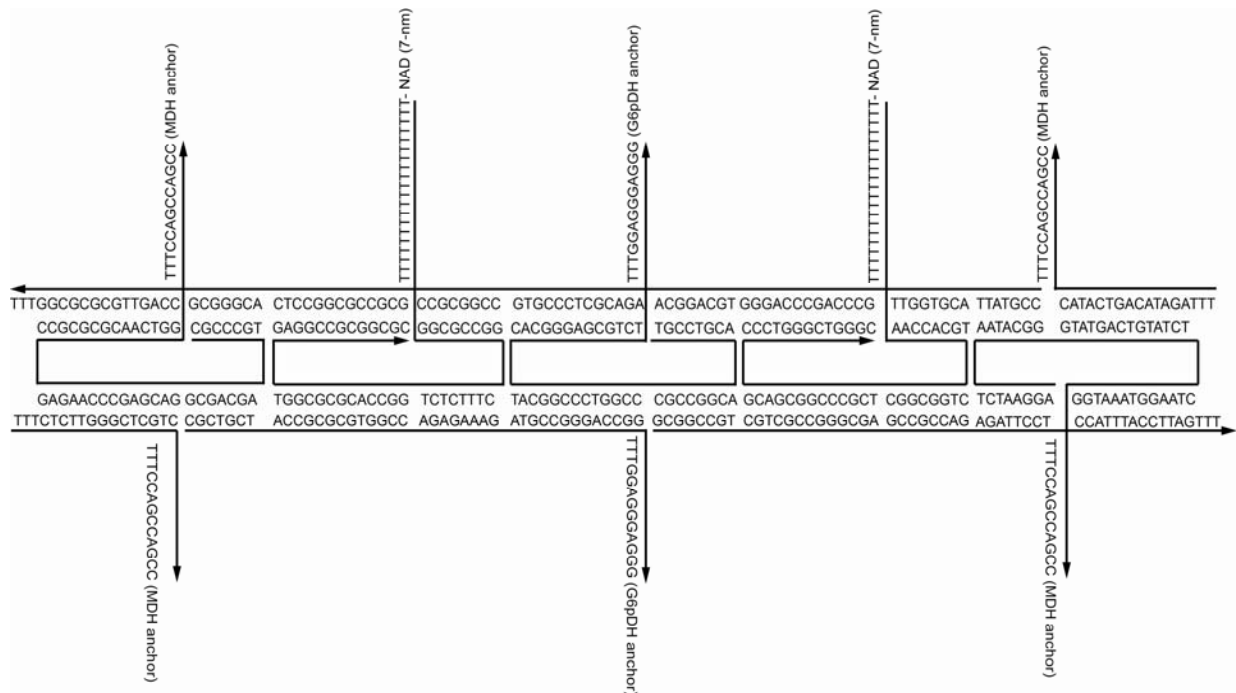


Figure S5. The DNA sequence design for the G6pDH-NAD⁺₂-MDH₂ swinging arm structure. The structure incorporates one pair of CP-1 strands to anchor G6pDH, two pairs of CP2 probes to anchor MDH, and two NAD⁺-modified poly(T)₂₀ swinging arms located in between the G6pDH and MDH anchor sites. The anchoring points of the swinging arms are designed to be 7 nm from the nearest molecules of G6pDH and MDH. All the probes and poly(T)₂₀ strand are designed to project from the same face of the tile.

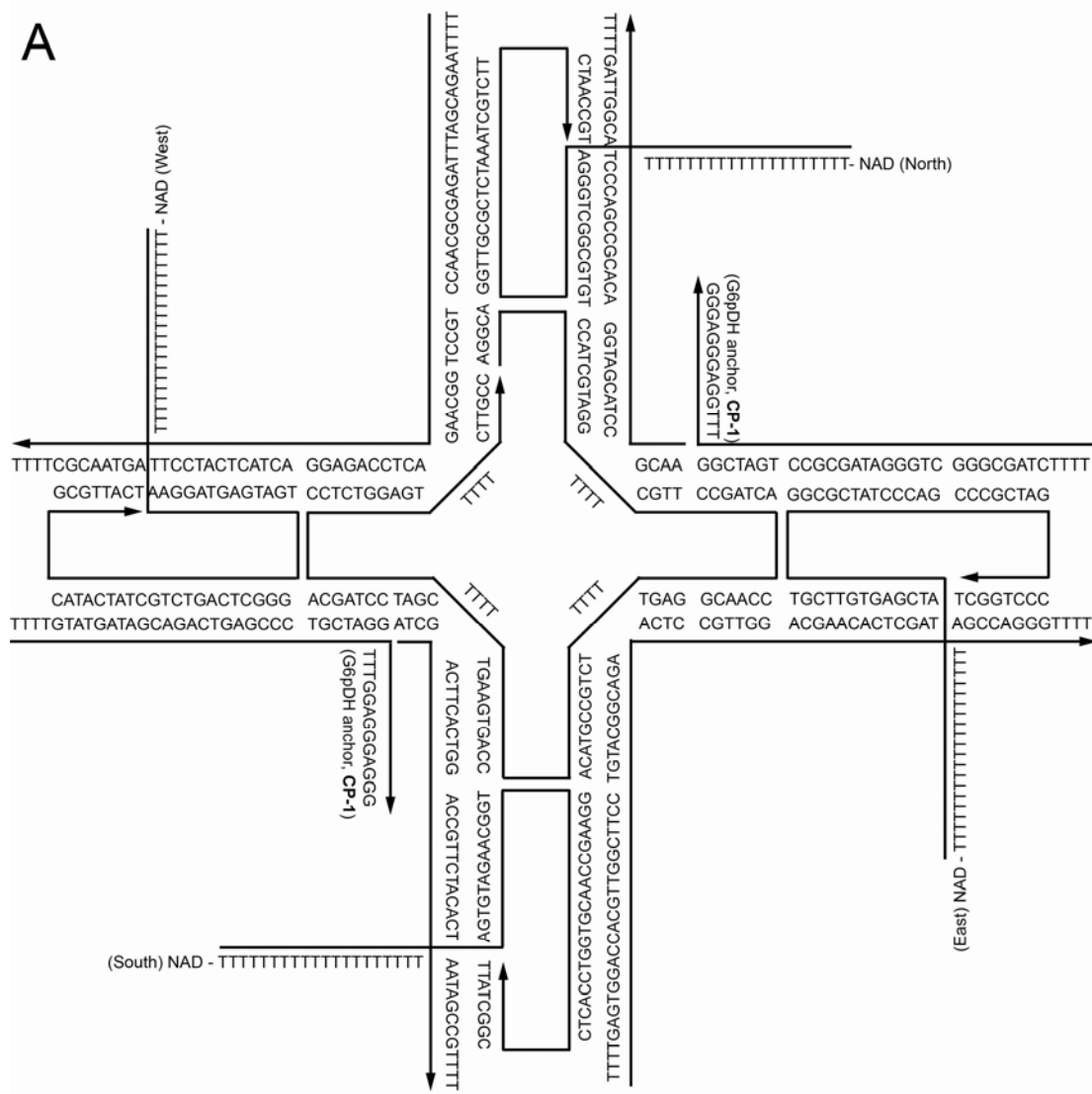
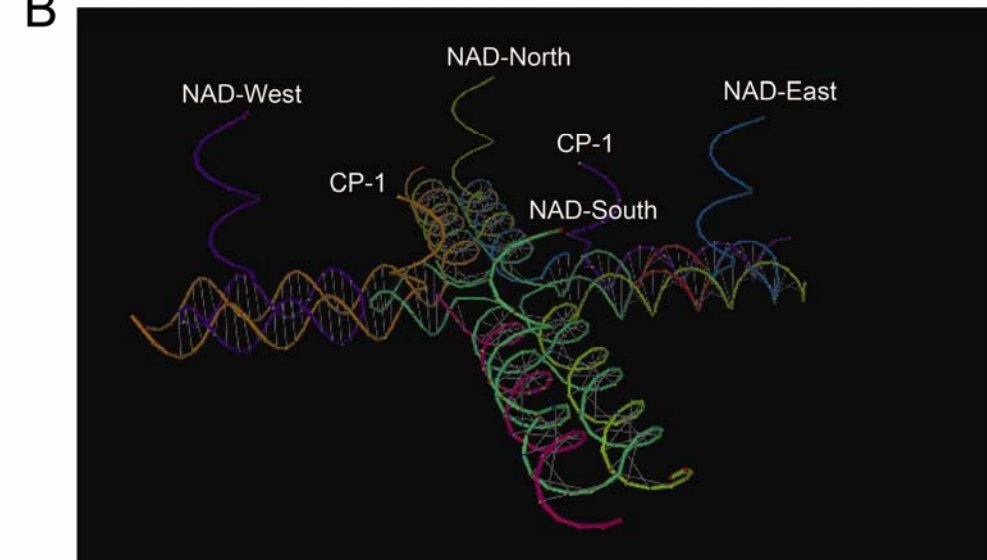
A**B**

Figure S6. DNA sequence design for the G6pDH–NAD⁺₄ swinging arm structure based on the 4×4 tile design. The structure incorporates two CP-1 strands that anchor G6pDH near the center of the tile, and four NAD⁺ modified poly(T)₂₀ located on the four arms of the tile (North, East, South, and West) are the swinging arms. All the probes and poly(T)₂₀ strands are designed to project from the same face of the 4×4 tile, with approximately 7-8 nm between the swinging arms and the enzyme at the center of the tile. (B) Computer modeling (Tiamat) of DNA nanostructures.

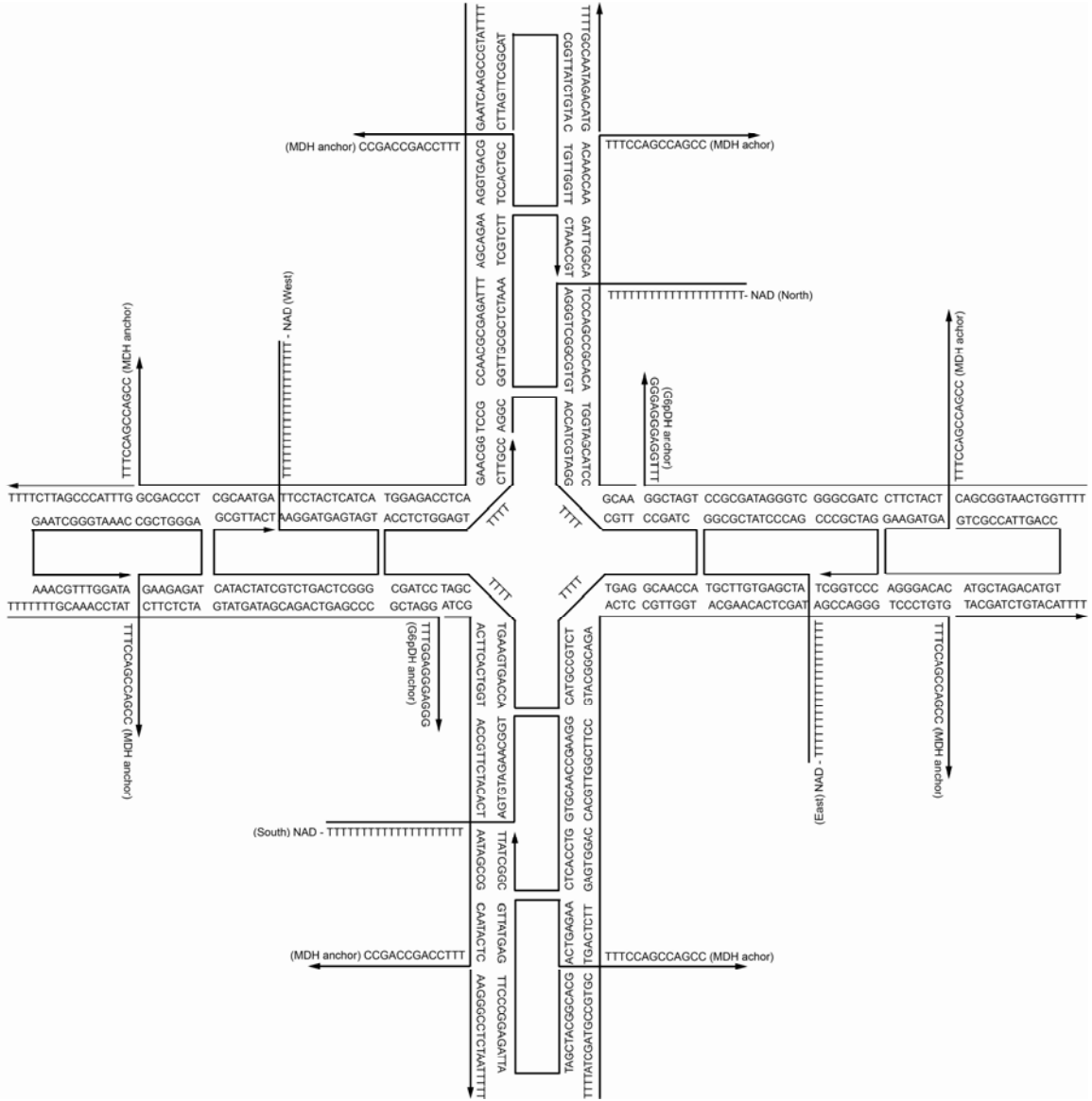


Figure S7. The DNA sequence design for the G6pDH-NAD⁺₄ -MDH₄ swinging arm structure based on the 4×4 tile design. The structure incorporates two CP-1 strands to assemble a single molecule of G6pDH near the center of the tile, four pairs of CP-2 strands to anchor MDH near the end of each of the four arms, and one NAD⁺-modified poly(T)₂₀ in the middle of each arm, ~5–8 nm away from each enzyme. All the probes are designed to project from the same face of the 4×4 tile.

Section 3: Preparation, purification, and characterization of protein-DNA conjugates

1. Protein-DNA conjugation

A. Pretreatment of proteins before conjugation to DNA: G6pDH (dimeric, ~ 100 kDa) ordered from Sigma (1) was washed with 10 mM sodium HEPES buffer (pH 7.4) using an Amicon-30 kD cutoff filter to get rid of small-molecular weight impurities. The crude MDH received from Sigma was found to form large protein aggregates. To reduce these aggregates, MDH was first washed with 10 mM sodium HEPES buffer (pH 7.4) using an Amicon-100 kD cutoff filter to remove impurities larger than 100 kD. Then the filtrate was concentrated with an Amicon-30 kD cutoff filter to collect the dimeric MDH (~ 70 kD) (2). The concentration of the enzymes was measured using UV absorbance at 280 nm and their respective extinction coefficients provided by the company ($115200 \text{ M}^{-1}\text{cm}^{-1}$ for G6pDH and $19600 \text{ M}^{-1}\text{cm}^{-1}$ for MDH).

B. DNA-protein conjugation reactions: The method used to link the enzyme to single-stranded oligonucleotides is similar to that described in a previous study (3). As shown in Figure S8A, SPDP was used to crosslink G6pDH to a 5' thiol-modified oligo (**P-1**: 5'-HS-TTT TTC CCT CCC TCC), and MDH (dimeric, ~ 70 kD) with another 5' thiol-modified oligo (**P-2**: 5'-HS-TTT TTG GCT GGC TGG). The conjugation reaction occurs in two steps, followed by multiple purification steps:

- a. First, 1000 μL of 40 μM enzyme solution was reacted with SPDP in 10 mM sodium HEPES (pH 8-8.5) for one hour, allowing amine-reactive N-hydroxysuccinimide (NHS) esters to react with the lysine residues on the protein surface. For G6pDH-SPDP conjugation, a 2-fold excess of SPDP was used, while for MDH-SPDP conjugation a 3.5-fold excess of SPDP was used. The optimal fold excess of SPDP was chosen by titrating varied ratios of SPDP to protein with the aim to label ~ 1-2 SPDP per protein on average. The SPDP label number determines the maximum number of DNA oligos that can be linked to the protein.
- b. Excess SPDP was removed by washing with 10 mM HEPES buffer using Amicon-30 kD cutoff filters. The SPDP coupling efficiency was evaluated by monitoring the increase in absorbance at 343 nm due to the release of pyridine-2-thione (extinction coefficient: 8080

$\text{M}^{-1}\text{cm}^{-1}$). Quantification of MDH-SPDP and G6pDH-SPDP modification *via* absorbance spectra is shown in Figure S8B and C).

- c. Next, the SPDP-modified protein was conjugated to a thiol-modified oligo ((P-1 for G6pDH and P-2 for MDH, 8-fold excess) through a disulfide bond exchange of the activated pyridyldithiol group. The reaction mixture was incubated in 10 mM sodium HEPES with 150 mM NaCl (pH 8-8.5) for one hour. The probability of SPDP reacting with cysteine on the protein surface is very low due to the very few available reduced cysteine on the protein surfaces, much more slow reaction diffusion of larger proteins as compared to smaller, and linear DNA molecules and over excess of DNA molecules over proteins in the solution.
- d. The excess oligo was removed by the filtration using Amicon-30 kD cutoff filters and washing one time with 100 mM HEPES (pH 7.4) containing 1 M NaCl, and three times with 1×PBS (pH 7.4). The high salt concentration in the first washing buffer helps to remove nonspecifically bound DNA from the surface of the protein due to electrostatic interactions. MDH-oligo conjugates were washed one extra time with 10 mM HEPES containing 150 mM NaCl and 0.05% (v/v) P-20 detergent to remove additional nonspecifically bound DNA.

2. FPLC purification of DNA-protein conjugates: Due to the presence of multiple lysine residues on the surface of both proteins, the reaction product is a mixture of protein-DNA conjugates with different numbers of DNA oligos per protein (and even for the conjugates with the same DNA labeling ratio, the labeling sites on the protein may also vary). To isolate a homogeneous population of enzymes modified with the same number of oligonucleotides, the DNA-conjugated proteins obtained in the above procedures were then purified by anion-exchange chromatography using AKTA fast-protein liquid chromatography (FPLC, GE Healthcare). For a typical purification, ~ 500 μL 50 μM G6pDH-P1 solution with an average labeling ratio of ~ 1.5 DNA molecules per protein was loaded into FPLC with an anion exchange column (MonoQ 4.6/100 PE, GE Healthcare) using an elution gradient (Figure S9) from 20% 50 mM sodium phosphate, 1 M NaCl to 55% 50 mM sodium phosphate, 1 M NaCl, with a flow rate of 1.5 mL/min. Multiple peaks from the purification chromatogram were collected and were identified respectively to be the unmodified protein, proteins with 1, 2, 3 and 4 DNA labels, and free DNA molecules which are determined by the UV-absorbance measurement (Figure S10 and

Table S3). The collected fractions were concentrated using Amicon-30 kD cutoff filters. After use, the FPLC system was cleaned by flowing with 30 mL pure water, and stored in 20% ethanol-water solution.

3. Characterization of the activity of DNA–protein conjugates:

A. Method for concentration measurements: The concentration of the DNA-conjugated protein in fractions collected during FPLC purification was quantified by absorbance at 260 and 280 nm (Table S3).

B. Activity assay: Activity of the purified DNA-labeled dehydrogenases was measured as dependent function of the number of DNA labels, as shown in Figure S11. Enzyme activities are evaluated by the rate of reduction of NAD⁺ to NADH (for G6pDH) or oxidation of NADH to NAD⁺ (for MDH) with absorbance change at 340 nm. The assay was performed with 1 mM glucose-6 phosphate or pyruvate (for MDH), 1 mM NAD⁺ or NADH(for MDH) in pH 8 HEPES buffer. G6pDH labeled with two DNA molecules maintained ~ 40% activity of the wild type, while labeling with 3 or 4 DNA molecules diminished activity further. In contrast, MDH is less sensitive to DNA labeling: MDH labeled with two DNA molecules maintained ~80% activity of the wild type.

4. Characterization of the assembly efficiency of DNA-protein conjugates on DNA nanostructures: The DNA-conjugated proteins with different DNA labeling ratios were tested for their efficiency of assembly on the DNA tiles, as shown in Figure S12. Both G6pDH and MDH labeled with two DNA molecules gave the highest proportion of the predominant product, presumably representing one protein per DX tile, with >80% yield.

5. Alexa dye labeling of DNA-conjugated proteins: The DNA-conjugated proteins were further labeled with spectrally distinct fluorescent dye molecules, which allow us to use native gel electrophoresis to unambiguously confirm the correct assembly of both proteins on the DNA tiles (Figure 1B in the main text). For a typical reaction, ~100 µL of 20 µM DNA-conjugated protein was incubated with a 10-fold molar excess of AlexaFluor 555 or AlexaFluor 647 in 1× PBS buffer for one hour in the dark (the AlexaFluor dyes are activated with an NHS ester, and react with lysine residues on the protein surface). 10 µL of 1 M sodium bicarbonate was added

into the solution to adjust the pH between 8–8.5. After incubation, the extra unreacted dye molecules were removed by washing the protein solution with 1× PBS buffer three times using an Amicon-30 kD cutoff filter, spun at 4,000 rpm (rcf would be more universal than rpm) for 10 minutes at 4°C. The UV-Vis absorbance spectra of the purified dye-labeled proteins are shown in Figure S13, and were used to quantify the concentration and labeling ratio of the dye-labeled proteins together with the extinction coefficients of the dye ($150,000 \text{ M}^{-1} \text{ cm}^{-1}$ for Alexa555 at 546 nm; $250,000 \text{ M}^{-1} \text{ cm}^{-1}$ for Alexa647 at 647 nm) and the protein-DNA conjugates (quantification is similar to that shown in Table S3).

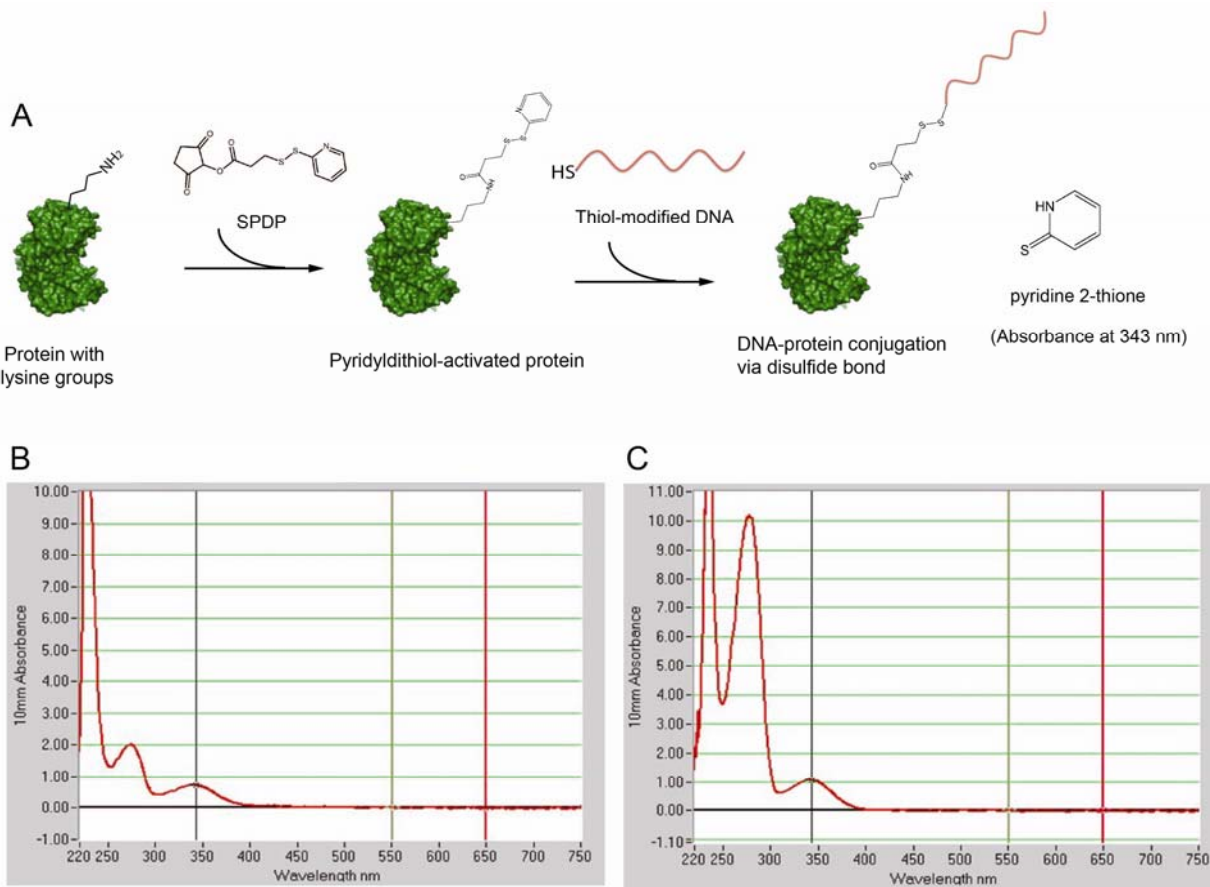


Figure S8. Protein-DNA conjugation using a SPDP cross-linker. (A) A schematic illustration of the conjugation chemistry. First, SPDP is coupled to the primary amine groups of the lysine residues at the protein surface; then, it is further reacted with thiol-modified DNA to couple the DNA to the protein. The reaction side product 2-thiopyridine has an absorbance at 343 nm with an extinction coefficient $8080 \text{ M}^{-1} \text{ cm}^{-1}$ which can be used to quantify the number of SPDP labeled per protein(4). (B) Quantification of MDH-SPDP modification by absorbance spectrum. ΔA_{343} upon SPDP conjugation and T-CEP treatment is ~ 0.72 , corresponding to $\sim 90 \mu\text{M}$ SPDP coupled to $70 \mu\text{M}$ MDH ($\epsilon=19600 \text{ M}^{-1} \text{ cm}^{-1}$ at 280 nm for MDH) (C) Quantification of G6pDH-SPDP modification by absorbance spectrum. ΔA_{343} upon SPDP conjugation is ~ 1.07 , corresponding to $\sim 130 \mu\text{M}$ SPDP coupled with $90 \mu\text{M}$ G6pDH ($\epsilon=115200 \text{ M}^{-1} \text{ cm}^{-1}$ at 280 nm for G6pDH). The SPDP labeling ratio was determined by adding 1 μL of 20 mM T-CEP (pH 7.4) to 20 μL SPDP-labeled protein in 10 mM sodium HEPES buffer (pH 7.4). T-CEP cleaves the disulfide bond and releases pyridine 2-thione with strong absorbance at 343 nm. T-CEP cleavage causes a slight absorbance increase at 280 nm, so it is necessary to record the protein concentration before performing the cleavage.

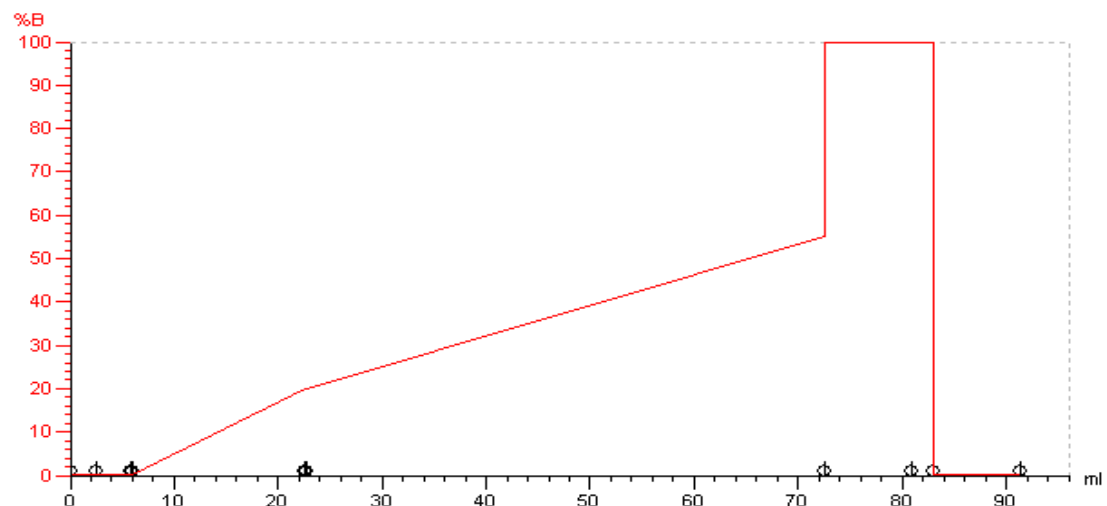


Figure S9. Elution gradient for anion-exchange chromatography. Buffer A: 50 mM sodium phosphate (pH 7.5); buffer B: 50 mM sodium phosphate and 1 M NaCl (pH 7.5).

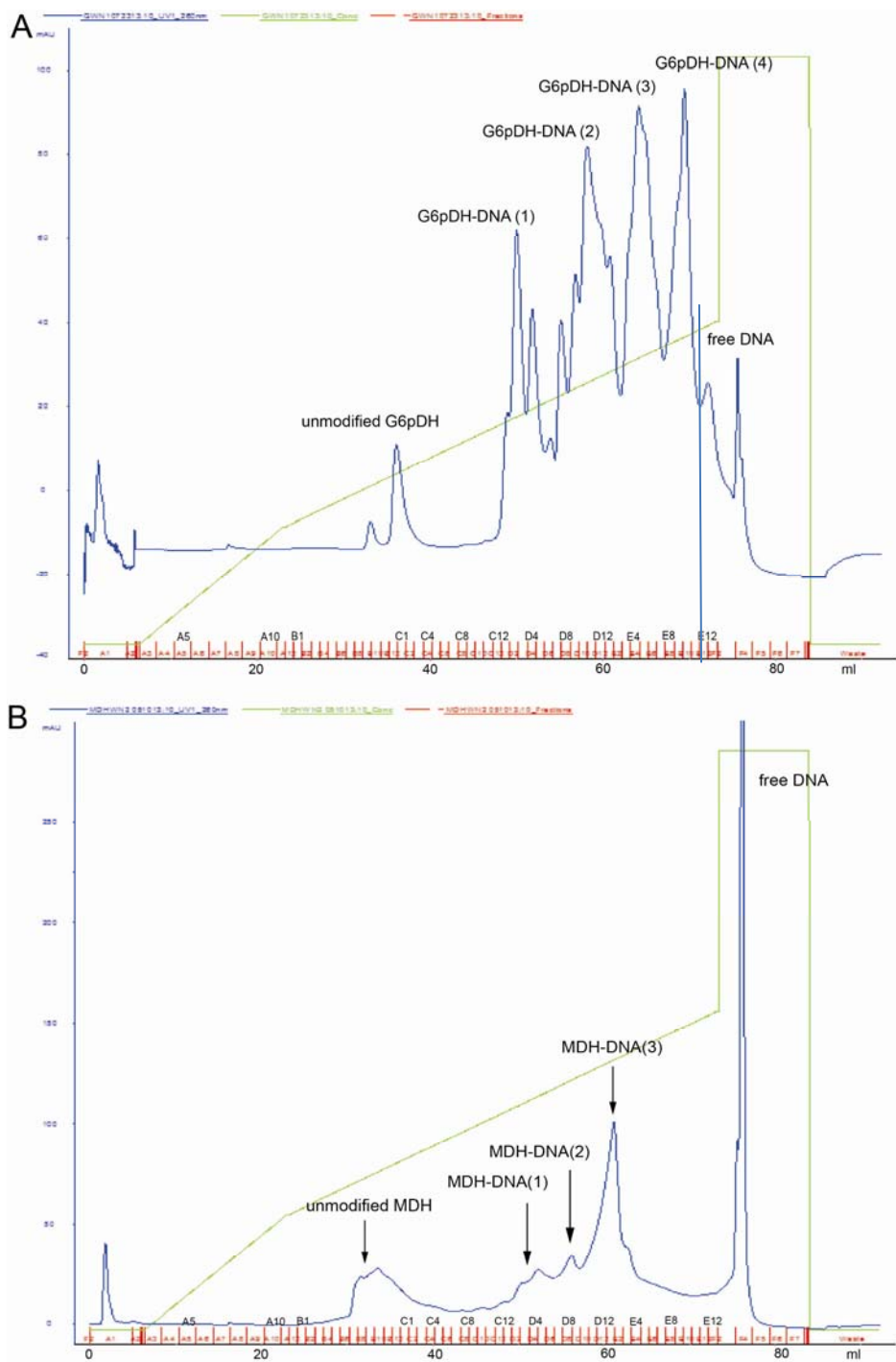


Figure S10. Anion-exchange FPLC to purify DNA conjugated proteins. (A) G6pDH-DNA conjugates, and (B) MDH-DNA conjugates. The proteins with different DNA label ratios were separated into distinct peaks that were collected in fractions. Condition: buffer A, 50 mM sodium phosphate (pH7.5); buffer B, 50 mM sodium phosphate, 1 M NaCl (pH 7.5). The identities of the distinct peaks were assigned using the A260 and A280 data (Table S3).

DNA	A260/A280	ϵ_{260} (M ⁻¹ cm ⁻¹)	ϵ_{280} (M ⁻¹ cm ⁻¹)	Protein	A260/A280	ϵ_{260} (M ⁻¹ cm ⁻¹)	ϵ_{280} (M ⁻¹ cm ⁻¹)	FPLC Fractions	A260/A280	A260	A280	DNA - to- Protein Ratio	Protein Conc. (uM)
P-1	1.27	115200	90709	G6pDH	0.52	61594	118450	D1-D5	0.86	1.28	1.49	1.08	6.88
P-1	1.27	115200	90709	G6pDH	0.52	61594	118450	D9-E2	0.96	6.651	6.90	1.89	23.80
P-1	1.27	115200	90709	G6pDH	0.52	61594	118450	E3-E7	1.03	8.557	8.30	2.80	22.29
P-1	1.27	115200	90709	G6pDH	0.52	61594	118450	E8-E11	1.08	6.855	6.34	3.88	13.47
P-2	1.60	130100	81313	MDH	0.72	14112	19600	D2-D6	1.42	1.73	1.22	0.92	12.87
P-2	1.60	130100	81313	MDH	0.72	14112	19600	D7-D10	1.50	2.05	1.37	1.81	8.23
P-2	1.60	130100	81313	MDH	0.72	14112	19600	E1-E4	1.53	6.16	4.014	2.97	15.39

Table S3. Quantification of the concentration and DNA labeling ratio of the purified G6pDH-DNA (P-1) and MDH-DNA (P-2) conjugates by measuring the absorbance at 260 and 280 nm, and using the following equations:

$$A_{260}(DNA - protein) = \epsilon_{260}(protein) * Conc.(protein) + \epsilon_{260}(DNA) * Conc.(DNA)$$

$$A_{280}(DNA - protein) = \epsilon_{280}(protein) * Conc.(protein) + \epsilon_{280}(DNA) * Conc.(DNA)$$

$$Ratio\left(\frac{DNA}{protein}\right) = \frac{Conc.(DNA)}{Conc.(protein)}$$

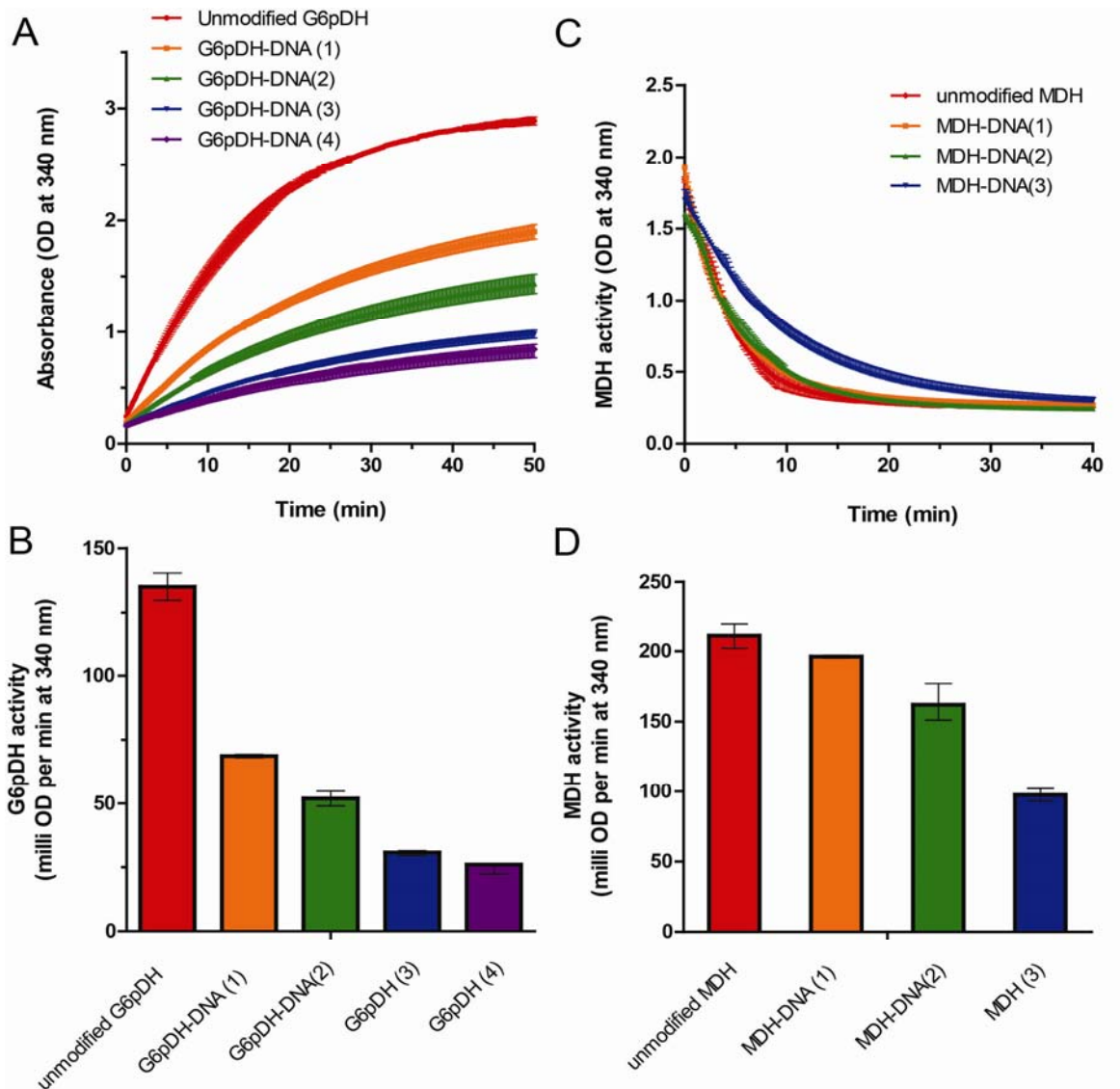


Figure S11. Dependence of the activity of the DNA-conjugated dehydrogenases on the DNA:protein labeling ratio. (A-B) G6pDH-DNA conjugates with DNA:protein labeling ratios of 0, 1, 2, 3 and 4, collected from FPLC in Figure S10A. Assay conditions: 2 nM G6pDH-DNA conjugate with 1 mM G6p and 1 mM NAD⁺ in 100 mM HEPES (pH 8). Enzyme activity is measured by the initial velocity of OD increase in absorbance at 340 nm due to the reduction of NAD⁺ to NADH. (C-D) MDH-DNA conjugates with DNA:protein labeling ratios of 0, 1, 2 and 3, collected from FPLC in Figure S10B. Assay conditions: 20 nM MDH-DNA conjugate with 1 mM oxaloacetic acid and 1 mM NADH in 100 mM HEPES (pH 8). Enzyme activity is measured by the initial velocity of OD decrease in absorbance at 340 nm due to the oxidation of NADH to NAD⁺. The details of the assay are in supplemental section 7.

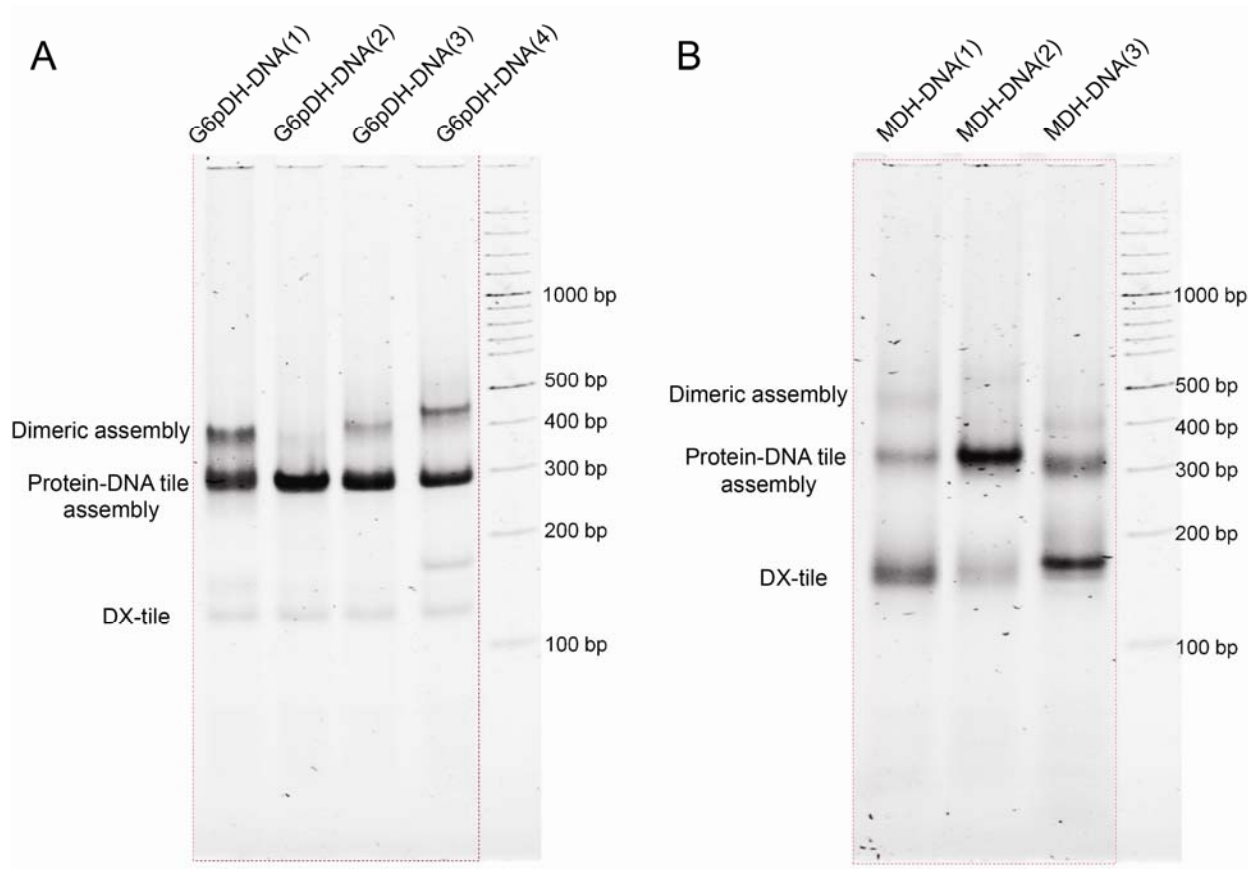
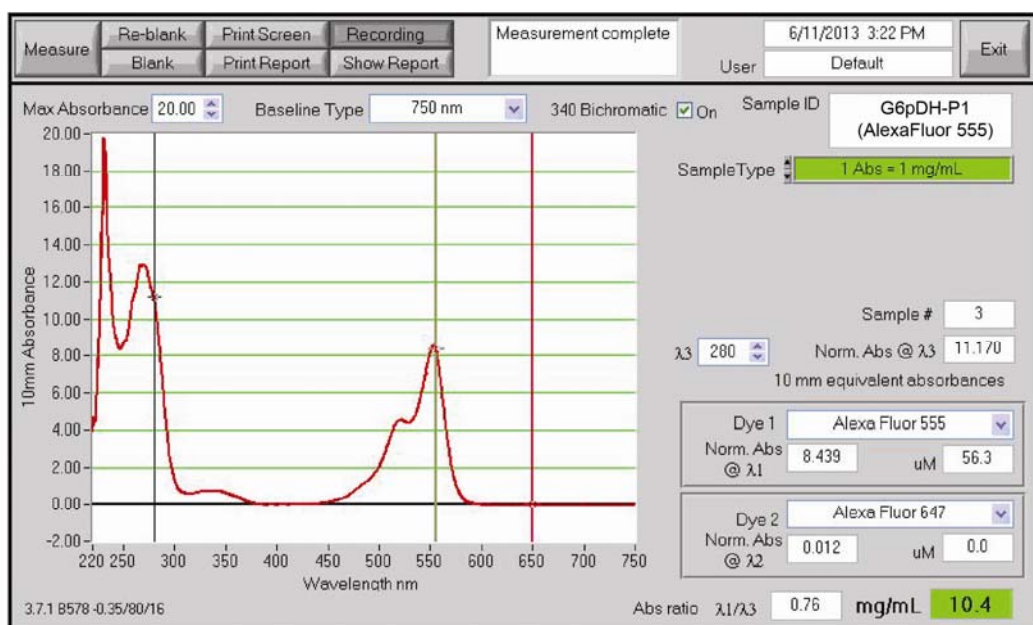


Figure S12. Native gel assay of the DNA labeling ratio on the assembly efficiency of the DNA-conjugated proteins on the DNA tile. (A) G6pDH-DNA conjugates and (B) MDH-DNA conjugates. DNA-conjugated proteins were purified using FPLC as shown in Figure S10. A twofold molar excess of protein-DNA conjugates was used for the assembly. The gels were stained with SYBR®Green to reveal the mobility of the assembled DNA structures. DX tile structures were similar as shown in Figure S1 and S2.

Discussion: For both G6pDH and MDH, the FPLC fractions labeled with two DNA molecules per protein gave the highest proportion of the predominant product, presumably representing one protein per DX tile, with >80% yield. Proteins labeled with one DNA molecule resulted in lower assembly yield and formation of a secondary product with lower mobility in the gel, which is likely to consist of two proteins bound to adjacent probes on the same DNA tile. Proteins labeled with three or four DNA molecules also resulted in aggregated, lower-mobility structures, possibly due to one protein molecule bridging two or more DNA tiles.

A



B

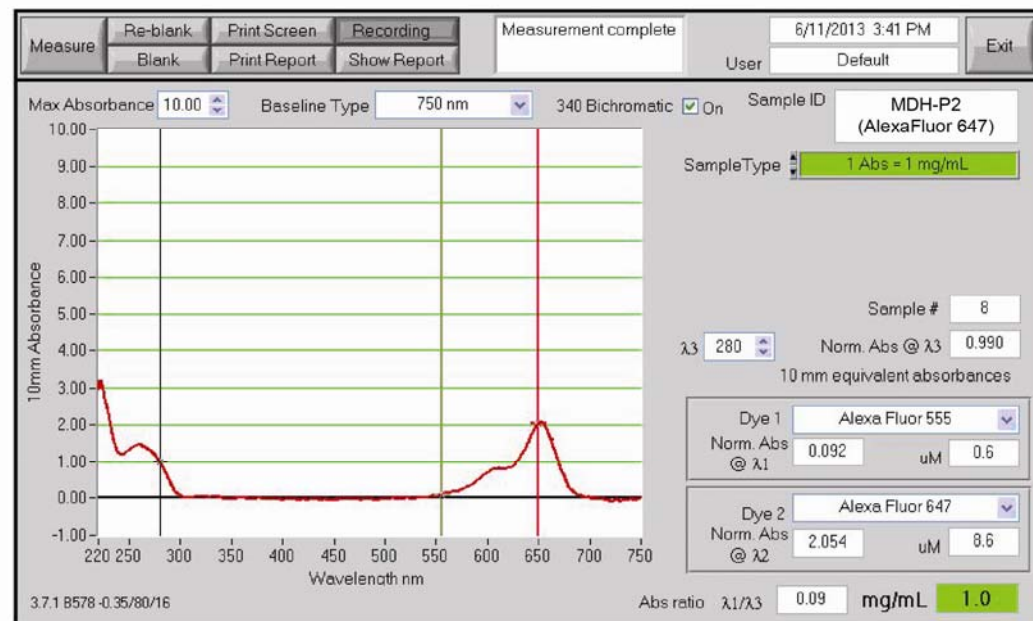


Figure S13. Quantification of fluorescent dye-labeled enzyme-DNA conjugates using UV-Vis absorbance spectroscopy. (A) AlexaFluor 555-labeled G6pDH-P1 with dye:protein labeling ratio about 2:1. (B) AlexaFluor 647-labeled MDH-P2 with dye:protein labeling ratio about 1.4:1.

Section 4: Preparation, purification, and characterization of NAD⁺-DNA conjugates

1) NAD⁺-DNA conjugation: The method for the conjugation approach is similar to that reported in a previous publication (4). Figure S14 shows the detailed reaction pathway of the conjugation of Aminoethyl NAD⁺ (AE-NAD⁺) to a 5'-amine-modified single-stranded oligonucleotide. A 200- μ L sample of 100 μ M 5'-amine-modified oligo was first immobilized onto 200 μ L anion-exchange DEAE-Sepharose resin (Sigma) by charge adsorption. Unbound oligo and water were removed by washing with DMF and filtering the resin in a Sigma Prep Spin column (pore size 7-30 μ m). A 200- μ L portion of 150 mM DSS was prepared in DMF with 2% (v/v) DIPEA. The oligo-bound resin was incubated with DSS for one hour. Excess DSS crosslinker was removed by washing the resin with DMF. To couple NAD⁺ to an oligo, a 10-fold excess of AE-NAD⁺ was incubated with the oligo-bound resin in 1 M HEPES, pH 8 for one hour. After the reaction, the oligo-bound resin was spun down at 3000 rpm to remove any unreacted AE-NAD⁺. To elute DNA molecules from the resin, DNA-bound resin was incubated with 50 mM HEPES containing 1.5 M NaCl (pH 8) for 10 min and spun down to collect the filtrate. AE-NAD⁺ was purified from the filtrate using HPLC (Agilent 1200) with an elution gradient of 25% methanol, 100 mM TEAA to 35% methanol, 100 mM TEAA (Figure S15A). Purified NAD⁺ conjugated DNA was characterized by MALDI-TOF Mass Spectrometry as shown in Figure S15B-D.

2) Characterization of the activity of the NAD⁺-DNA conjugates: Since the NAD⁺-modified DNA must undergo thermal annealing to form DNA nanostructures, the thermal stability of the NAD⁺-coupled oligo was measured by incubating them at varied temperatures (25-95°C) for different times (0-60 min) and then measuring the dehydrogenase activity using G6pDH/NAD⁺ catalyzed reactions, as shown in Figure S16. AE-NAD⁺ activity was evaluated via the reduction of NAD⁺ to NADH by G6pDH, followed by a coupled PMS-catalyzed resazurin reaction as described in Figure S30A. The relative enzyme activity was calculated by analyzing the slopes of the product vs. time traces, which were obtained by fitting the raw time traces in (Figure S16b-d) with a linear regression. Assay conditions: 50 nM G6pDH, 50 μ M AE-NAD⁺, 1 mM glucose-6-phosphate, 200 μ M PMS and 400 μ M resazurin in 1×TBS with 1 mM MgCl₂ at pH 7.5, at room temperature. The results indicate that NAD⁺ maintains most of its

activity after incubation at temperatures $< 75^{\circ}\text{C}$, but is dramatically inactivated by incubation at temperatures higher than 85°C for even a short time (10 min).

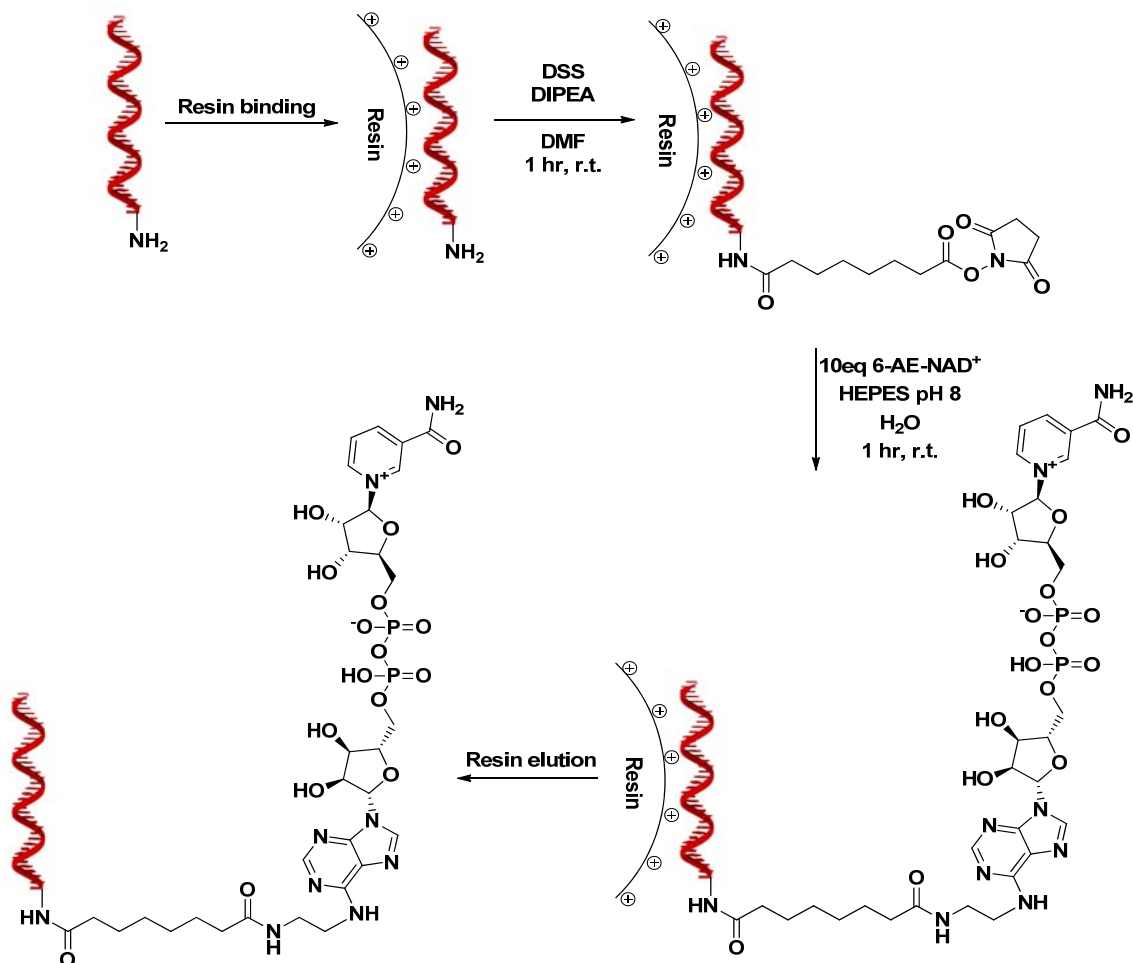


Figure S14. Reaction pathway for the conjugation of aminoethyl NAD⁺ to 5' amine-modified DNA strands using resin-based DSS crosslinking chemistry. First the 5'-amine-modified DNA strand is adsorbed on the surface of positively charged resin by electrostatic interactions. A solution of DSS and DIPEA in DMF is added to the resin for 1 hour to activate the amine group on DNA. The excess DSS and DIPEA are removed by washing the resin with DMF. 10 equivalents of 6-AE-NAD⁺ in HEPES buffer (pH 8) are added to the resin and incubated for 1 hour, coupling the NAD⁺ to the DNA. The NAD⁺-DNA is eluted from the resin with 50 mM HEPES containing 1.5 M NaCl, then further purified by HPLC and characterized by MALDI-MS (Figure S15) (4).

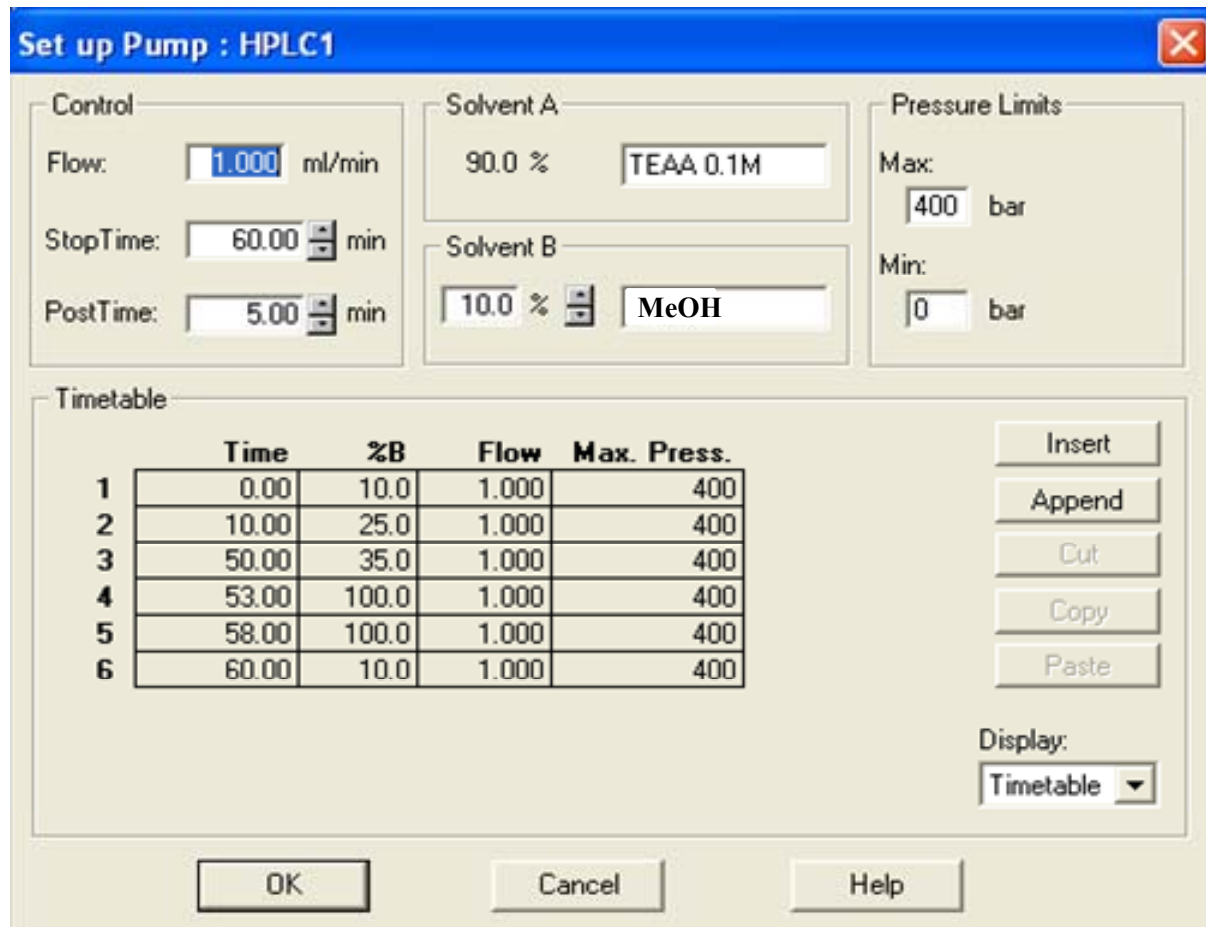
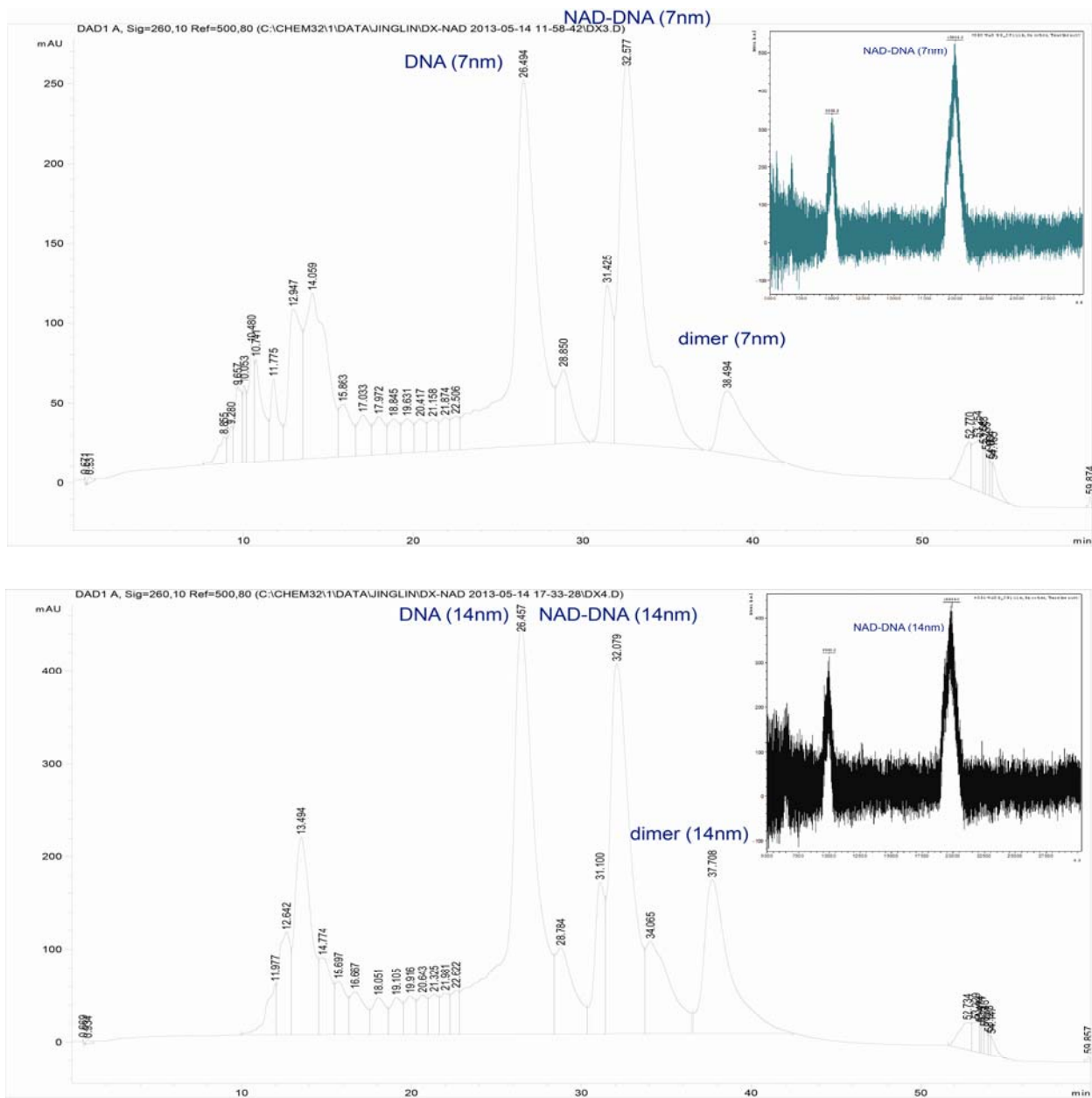


Figure S15 A. HPLC elution gradient for purifying DNA-NAD⁺ conjugates. Buffer A: 100 mM Triethylammonium acetate (TEAA); Buffer B: Methanol.



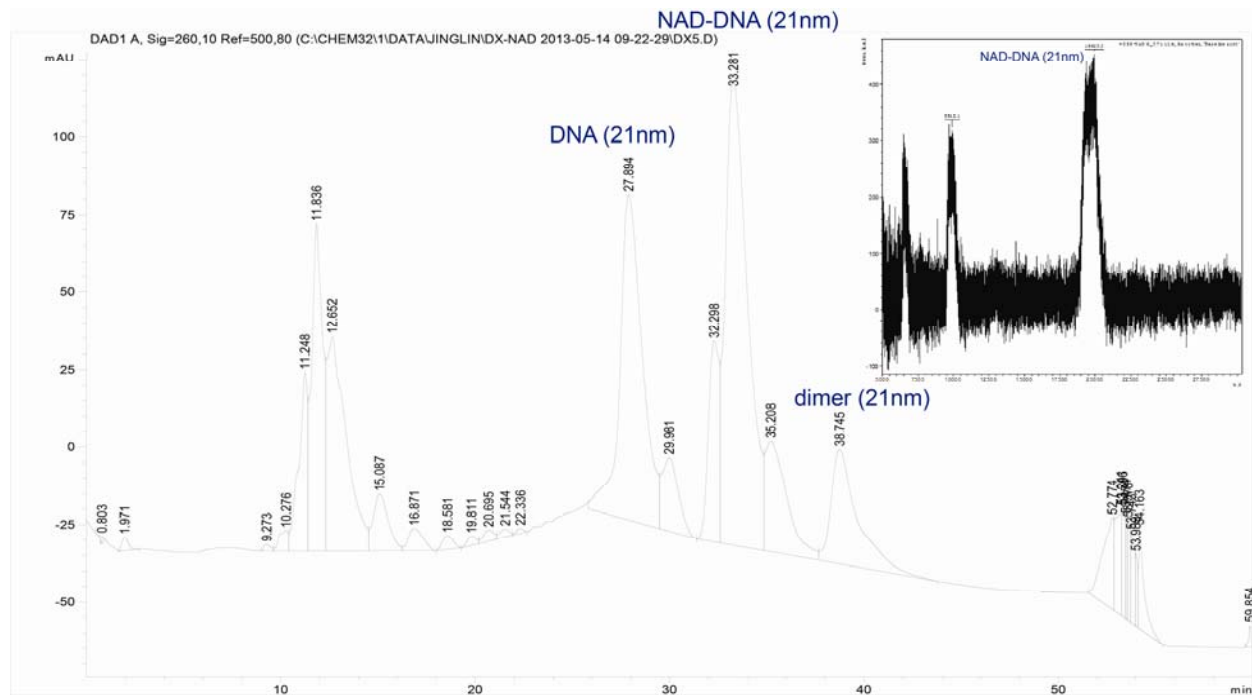
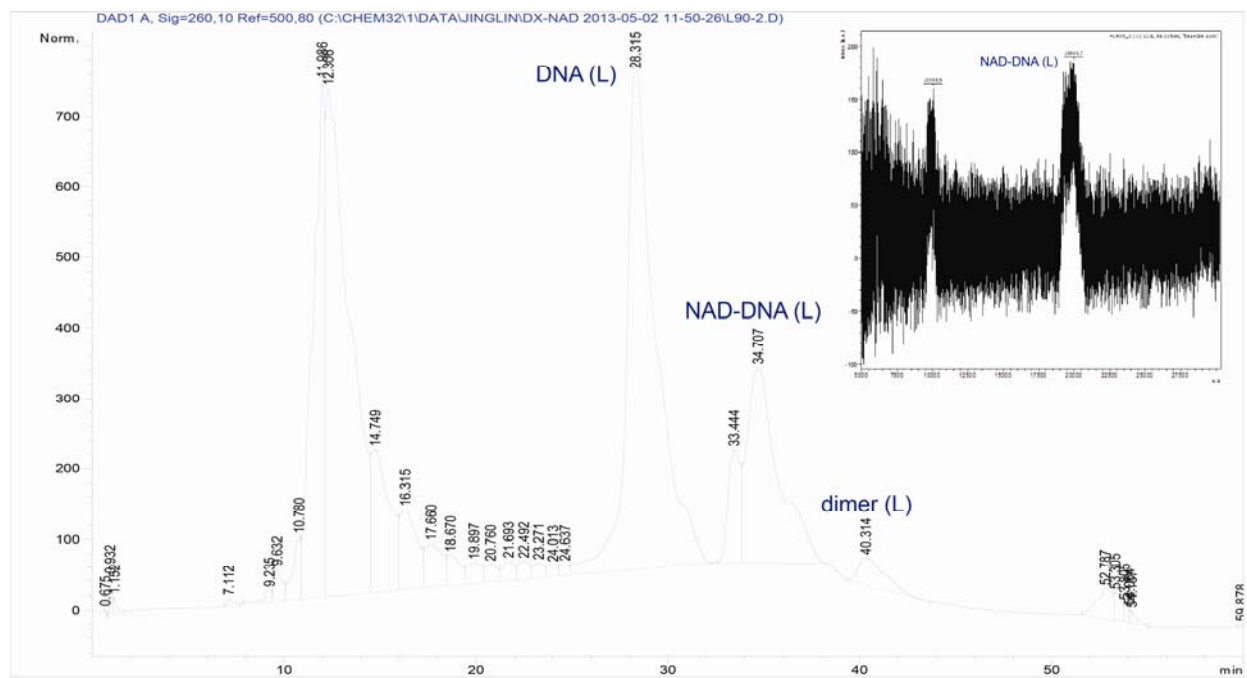
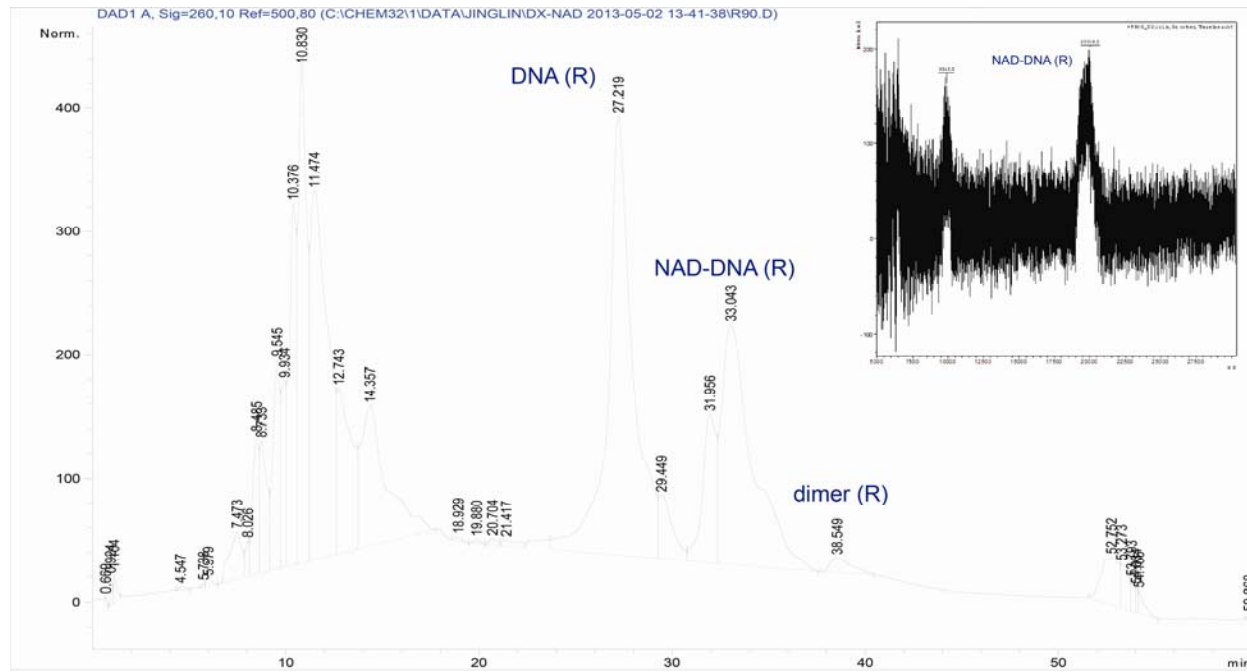


Figure S15 B. HPLC purification and MS characterization (inset, upper right) of NAD^+ -modified poly(T)₂₀ oligos that are designed to be anchored 7-nm, 14-nm and 21-nm away from G6pDH as shown in Figure S1 and Figure 2C and D in the main text. The MALDI-MS characterization of the HPLC-purified sample shows peaks for product carrying both one and two positive charges, the latter appearing at half the molecular weight of the former.



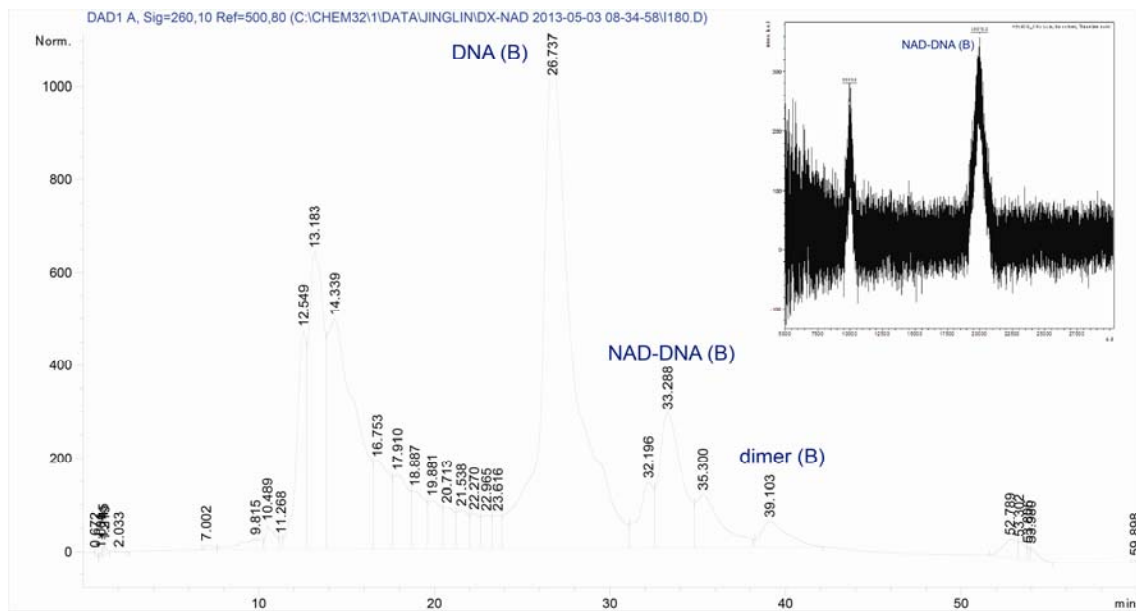
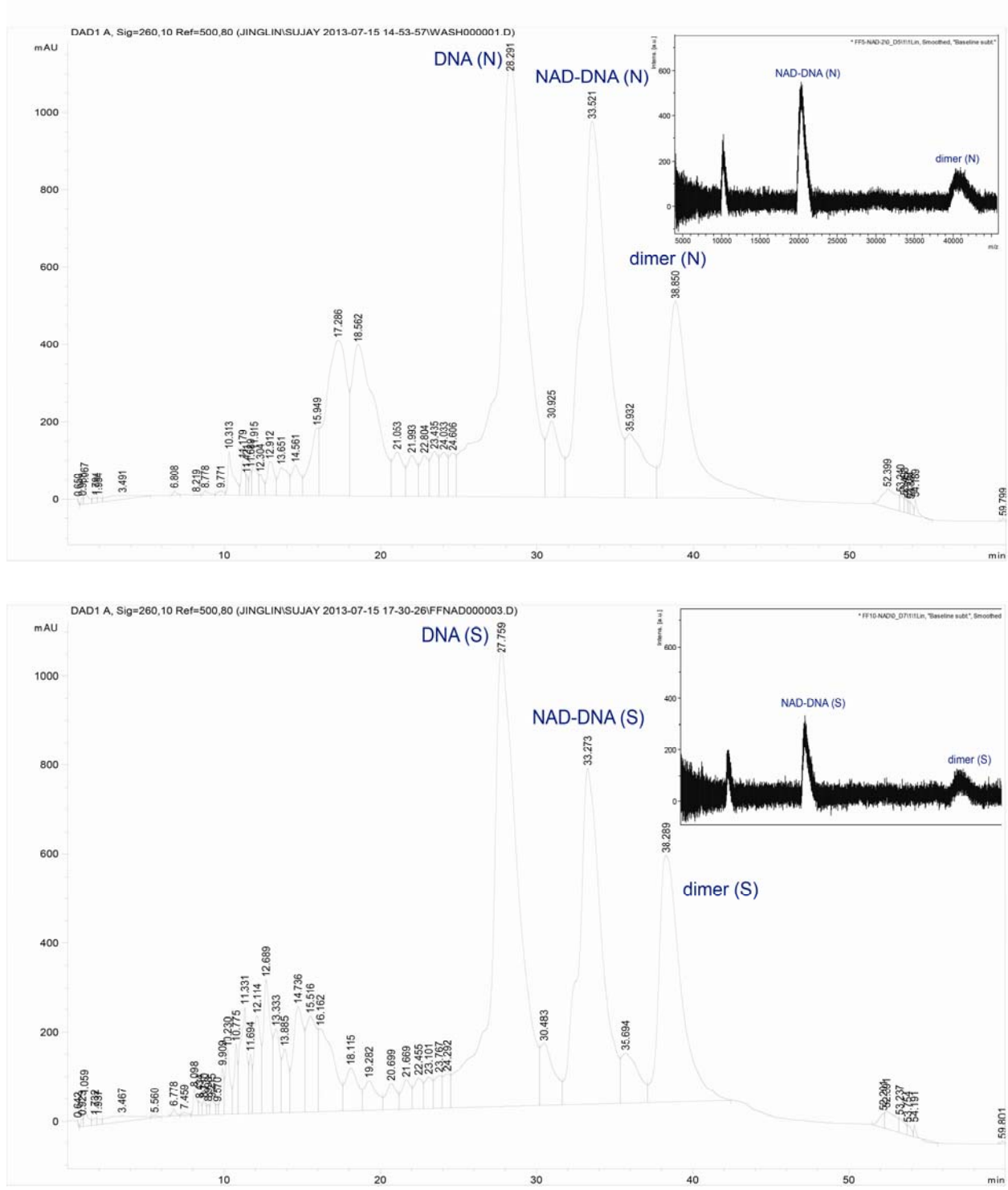


Figure S15 C. HPLC purification and MS characterization of NAD^+ -modified poly(T)₂₀ strands that are designed to be anchored at the left, right and bottom relative to the anchoring position of the enzymes as shown in Figure 2E and F in the main text and Figure S4. The MALDI-MS characterization of the HPLC-purified sample shows peaks for product carrying both one and two positive charges, the latter appearing at half the molecular weight of the former.



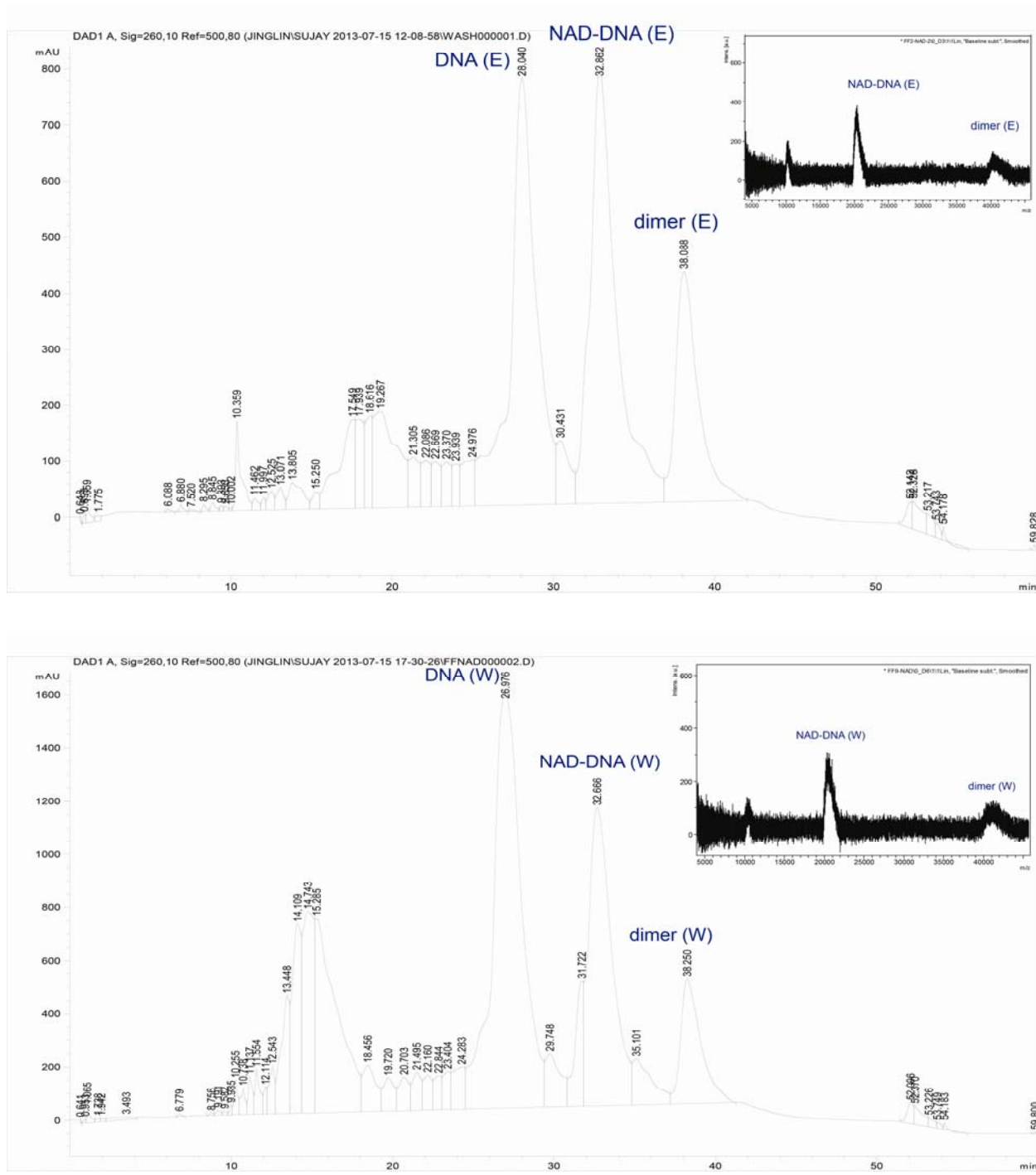


Figure S15 D. HPLC purification and MS characterization of NAD^+ -modified poly(T)₂₀ strands that are designed to be anchored on the 4x4 tile as shown in Figure S6 and S7. (N), (S), (E), (W) indicate the strands located on the North, South, East and West arms of the 4x4 tile, respectively. The observed mass of each of the NAD^+ -DNA conjugates matches the expected mass well.

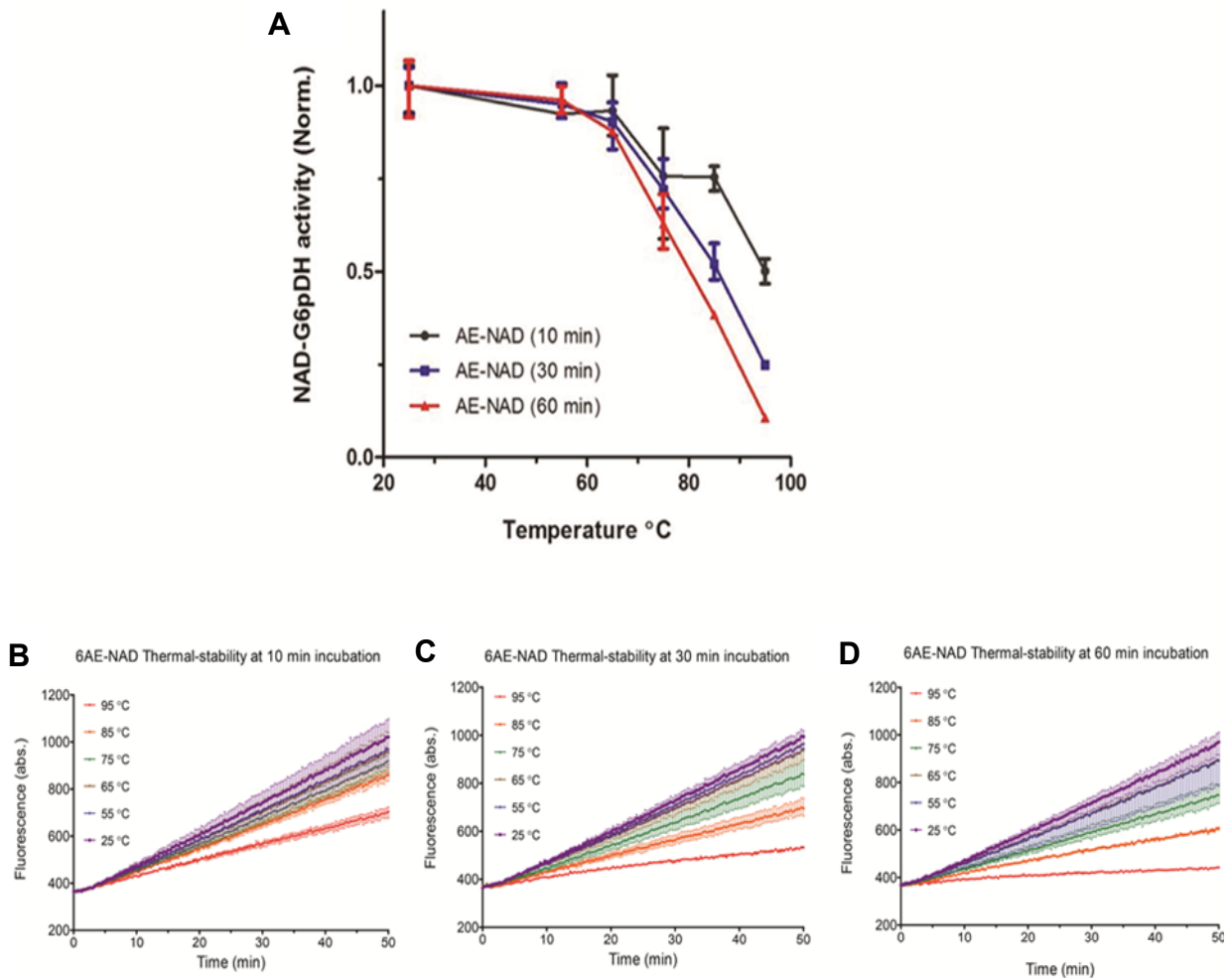


Figure S16. Evaluation of the thermal stability of aminoethyl-modified NAD⁺ (AE-NAD⁺). (A) Normalized G6pDH/AE-NAD⁺ activity after incubating the AE-NAD⁺ at various temperatures then adding it to the enzyme-substrate reaction mixture. AE-NAD⁺ was incubated at a series of temperatures ranging from 25 to 95°C for 10 min (black), 30 min (blue) and 60 min (red), respectively. Activity under all conditions was normalized to that of the sample incubated at 25°C. (B-D) Raw activity traces for G6pDH/AE-NAD⁺ after AE-NAD⁺ was pre-incubated at various temperatures for 10, 30 and 60 min, respectively (4).

Discussion: The activity of AE-NAD⁺ is significantly diminished after incubation at temperatures higher than 70°C, even briefly (10 minutes). Incubation at temperatures up to 60°C for 1 hour did not cause significant reduction of NAD⁺ activity. In order to assemble the DNA nanostructures, a thermal annealing process is required which involved an increase of the temperature and then slowly cool down. Based on the thermal stability studies here, a

modification of the annealing program with a very quick temperature drop in the high temperature range (Table S1) is necessary to avoid losing the activity of NAD⁺ carried on the DNA structure.

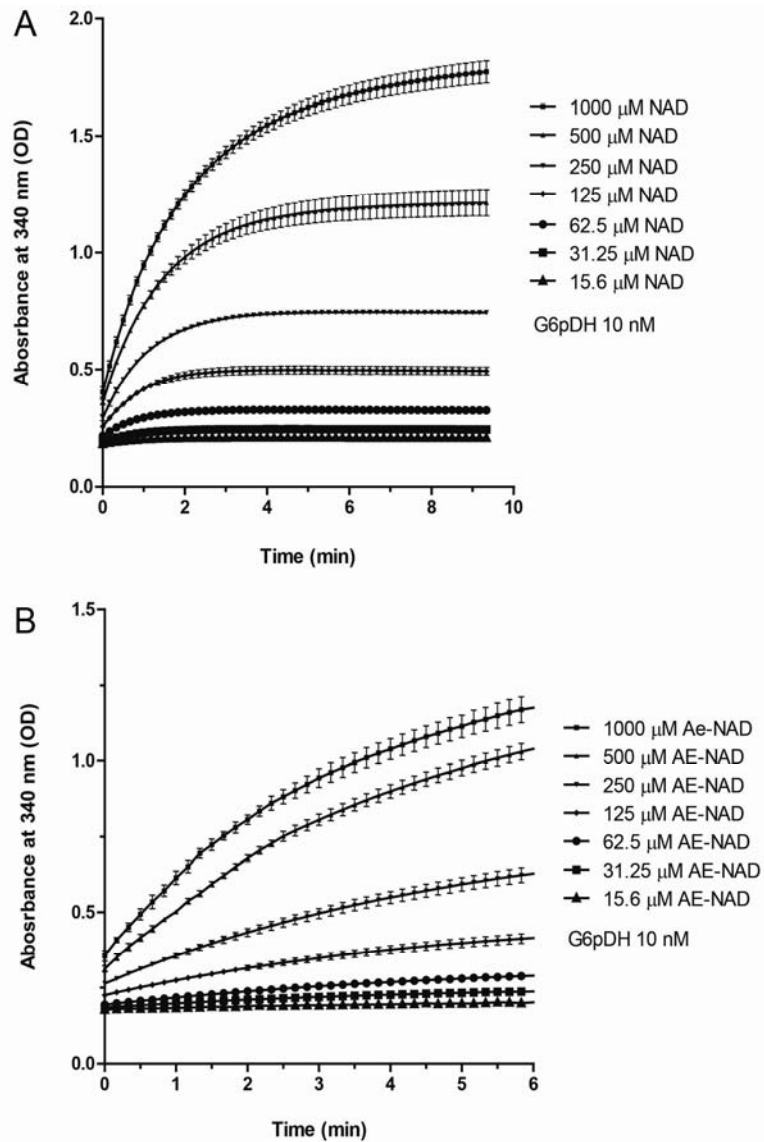


Figure S17. Raw data showing the dependence of G6pDH activity on cofactor concentration. Time traces are shown for the (A) G6pDH/NAD⁺ pair and (B) G6pDH/AE-NAD⁺ pair. Assay conditions: 10 nM G6pDH (unmodified), 1 mM G6p, 15.6-1000 μ M NAD⁺ or AE-NAD⁺ in 100 mM HEPES (pH 8). The production of NADH was monitored by following absorbance at 340 nm over time.

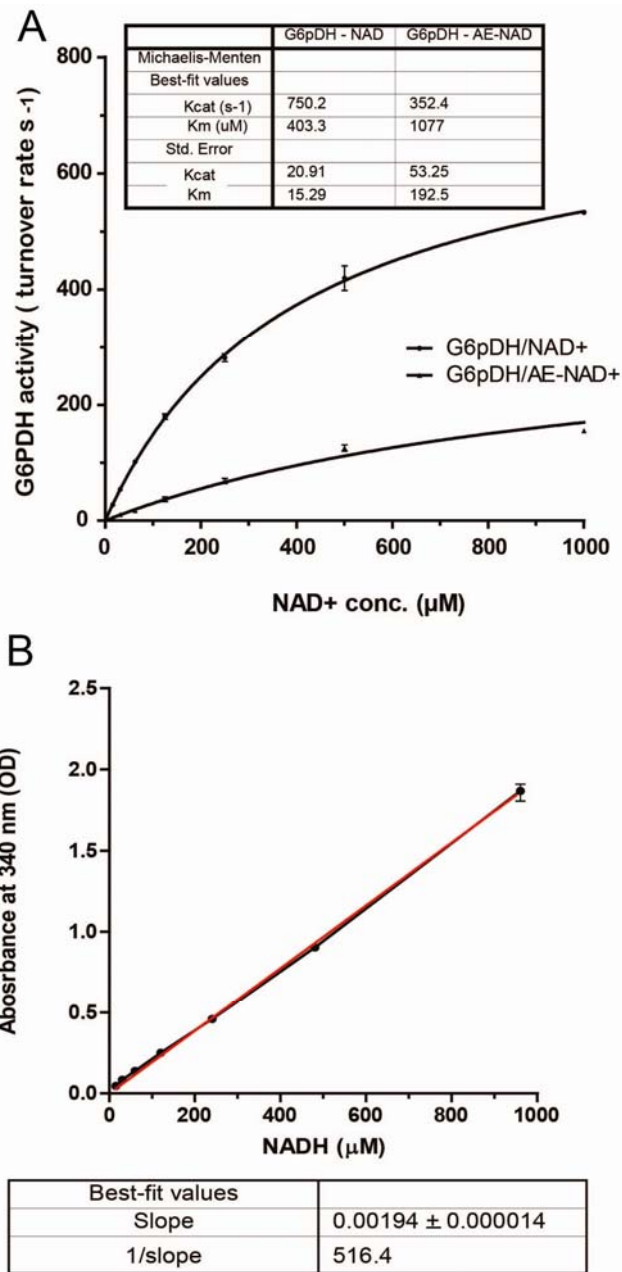


Figure S18. (A) Michaelis-Menten plot for G6pDH activity (turnover rate) vs. NAD⁺ and AE-NAD⁺ concentration. Enzyme turnover rate was calculated by fitting the initial velocity (linear activity range) of raw activity traces in Figure S17 to a straight line. (B) Standard curve of Absorbance vs. NADH concentration for converting the OD value to the molar concentration of NADH produced by G6pDH. The standard curve fitting sets the condition of X=0, Y=0. GraphPad Prism 6 is used for the Michaelis-Menten fitting. All the tests were performed with free enzymes and free NAD⁺ molecules.

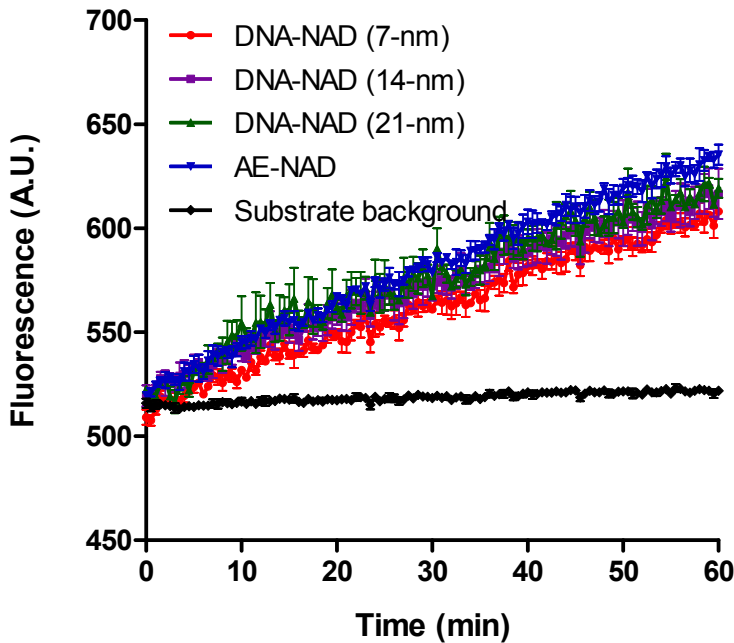


Figure S19. Comparison of the activity of DNA-NAD⁺-conjugates with that of AE-NAD⁺.

All three DNA- NAD⁺ conjugates with different sequences (for the 7-nm, 14-nm and 21-nm swinging arms, as shown in Figure S1 have similar activities. AE-NAD⁺ shows comparable activity with those of the DNA-NAD⁺ conjugates – only slightly (10%-20%) higher. Conditions: 100 nM G6pDH and 100 nM DNA-NAD⁺-conjugate or AE-NAD⁺ assayed with 1 mM G6p and 500 μ M PMS/resazurin in 1×TBS buffer (pH 7.5). The reaction is monitored by the fluorescence increase of PMS/resazurin at 590 nm with excitation at 544 nm.

Discussion: The activity of DNA-NAD⁺ conjugates was compared with those of AE-NAD⁺ and unmodified NAD⁺ by a G6pDH-catalyzed reaction. Figures S16 and S17 show that the G6pDH/AE-NAD⁺ pair maintains $\sim 20\%$ catalytic efficiency (k_{cat}/K_m) of the G6pDH/NAD⁺ pair. The NAD⁺-DNA conjugates exhibit slightly lower activity ($\sim 10\text{--}20\%$ less active) than that of AE-NAD⁺, as shown in Figure S19. The activity of NAD⁺-DNA conjugates with different DNA sequences of the same length (for the 7, 14 and 21-nm distances) is similar, indicating that the activity of NAD⁺-DNA conjugates is independent of the sequence of the attached DNA.

Section 5: Assembly, purification, and characterization of proteins on DNA nanostructures

1) DNA tile assembly: was described in section 2 and used the thermal annealing program shown in Table S1.

2) Protein-DNA tile Assembly: The assembly of protein-DNA nanostructures was optimized by combining the DNA tiles with a one-, two-, or threefold molar excess of protein as shown in Figure S20. An optimal assembly yield of more than 80% was achieved with a twofold molar excess of DNA-conjugated G6pDH or MDH; a threefold excess gave no significant improvement. Proteins were assembled onto DNA structures using a one-hour annealing program in which the temperature was first held at 37 °C for 5 min and then decreased from 36 °C to 16 °C at 2 min/ °C and finally held at 15 °C.

3) Size-exclusion purification of protein-DNA tile assemblies: After assembly, excess proteins and aggregates were removed by size-exclusion chromatography using a Superdex 200 HR 10/30 column (GE Healthcare) and a fast protein liquid chromatograph (FPLC) system (AKATA, GE Healthcare). For a typical purification, ~ 500 µL, 750 nM protein-DNA tile assemblies were loaded onto the FPLC column and eluted with 100 mM HEPES containing 100 mM NaCl (pH 8) at a flow rate of 0.25 mL/min. An example chromatogram from the purification of G6pDH-NAD⁺-MDH swinging arm structures is shown in Figure S21.

4) Native gel characterization of the purified assembly: The fractions collected from the FPLC column were characterized with native PAGE to identify assembled structures based on comparison with an unpurified sample. The purified protein-DNA tile structures were quantified by absorbance at 260 nm (see data in Table S2).

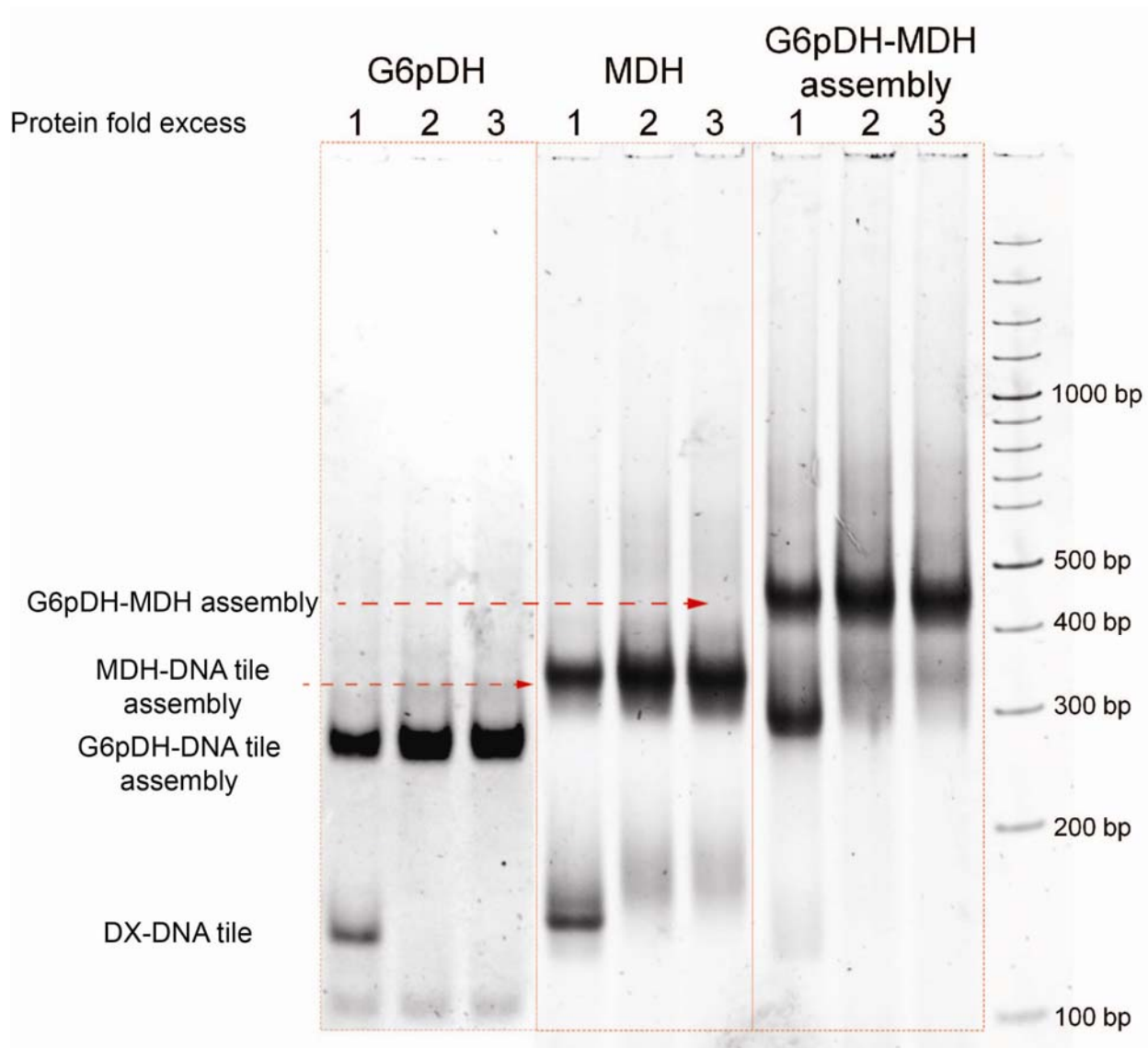


Figure S20. Native 3% PAGE characterization of the assembly of protein-DNA conjugates with DNA tiles. Each assembly is carried out with a protein:DNA tile molar ratio of 1:1, 2:1 and 3:1. The DNA-conjugated G6pDH and MDH possess ~2 DNA labels per protein and have been purified using anion exchange chromatography as shown in Figure S10 A&B. A twofold molar excess of DNA-conjugated G6pDH and/or MDH gave the high assembly yield of more than 80% according to the gel results (product band intensity divided by the intensity of the entire lane) and FPLC.

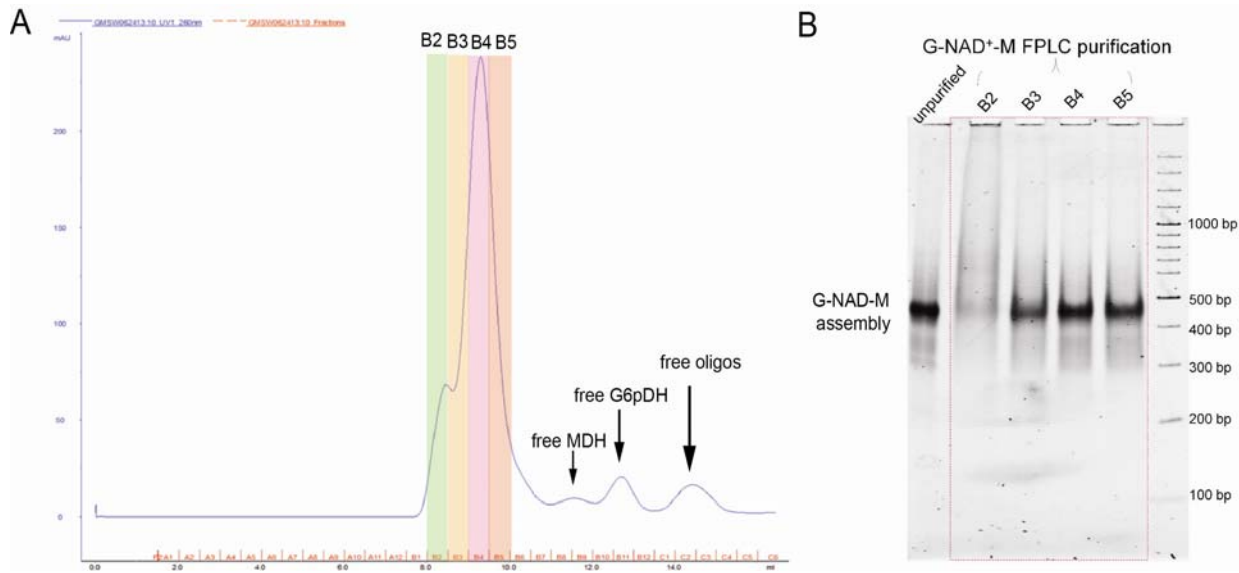


Figure S21. Purification of G6pDH-NAD⁺-MDH swinging arm structures. (A) Chromatogram from size-exclusion FPLC purification of assembled G6pDH-NAD⁺-MDH swinging arm structures to remove excess enzymes and free DNA oligoes. Fractions B2-B5 were collected, representing the fully assembled structure incorporating both the enzymes and the NAD⁺-labeled poly(T)₂₀. (B) Native 3% PAGE characterization the fractions collected in size-exclusion FPLC; fraction B2 contains a large proportion of aggregated structures (smear band). Fractions B3 to B5 consist primarily of fully assembled swinging arm structures. Unpurified swinging arm structure is also shown in the left lane as a control.

Section 6: Single-molecule FRET (smFRET) characterization of swinging arm dynamics

1. Design of DNA nanostructures. The designs of the DNA-only models of the swinging arm system for single-molecule FRET experiments are shown in Figure S22. These include (a) a full swinging arm system with 7 nm between the anchoring points of the Cy3-labeled swinging arm and each of two probes, labeled with Cy5 or BHQ-2; and (b) a semi-swinging arm system with varying distance (7, 14, or 21 nm) between the anchoring points of a Cy5-labeled probe and the Cy3-labeled swinging arm. The DNA tiles are also biotinylated to allow immobilization on a streptavidin-coated microscope slide.

2. Instrument and methods. Single-molecule FRET experiments were carried out on an inverted total internal reflection fluorescence (TIRF) microscope with a 1.2 NA 60 \times water-immersion objective (IX71, Olympus) in a darkened room at an environmentally controlled temperature of 20 ± 3 °C. Fluorescence excitation was provided by a 532-nm green laser (CrystaLaser CL532-050-L, 50 mW, attenuated and focused to give an illumination intensity of \sim 100 W/cm² in the sample plane); presence of an active FRET acceptor was confirmed at the beginning and end of each experiment by brief excitation with a 640-nm red laser (Coherent CUBE 635-25C, 25 mW). The Cy3 and Cy5 emission signals were separated by a dichroic mirror with a cutoff wavelength of 610 nm (Chroma) and projected side-by-side onto an ICCD camera chip (iPentamax HQ Gen III, Roper Scientific, Inc.) with a full-frame acquisition rate of 10 Hz. The Cy3 channel image was passed through a bandpass filter (HQ580/60m, Chroma) and the Cy5 channel was passed through a long-pass filter (HQ655LP, Chroma). A Newport ST-UT2 vibration isolation table was used in all experiments to reduce instrument interference. In all smFRET measurements, an oxygen scavenger system (OSS \equiv 5 mM 3,4-dihydroxybenzoic acid, Sigma P5630; 2 mM Trolox, Acros 218940050; and 50 nM protocatechuate dioxygenase, Sigma-Aldrich P8279) was included in the imaging buffer to retard photobleaching (5).

3. Sample preparation for smFRET experiments. Microscope slides were constructed with flow channels and coated with biotinylated BSA and streptavidin as described previously (6) to permit surface immobilization of biotinylated DX tiles bearing the swinging arm and complementary probe(s). A solution containing 20 nM of a DX tile and either 0.2 μ M (in the case of half-arm structures) or 2 μ M (in the case of the full swinging arm structure) of **P*-1** (5'-

CCC TCC CTC CTT TAT AGT GAA ATT), **Cy5-P*-1** (5'-CCC TCC CTC CTT TAT AGT GAA ATT-Cy5), **P*-2** (5'-GGC TGG CTG GTT TAT AGT GAA ATT), and/or **BHQ2-P*-2** (5'-GGC TGG CTG GTT TAT AGT GAA ATT-BHQ2) strands was incubated for 30 min at 37 °C in the presence of 1×TAE-Mg²⁺ (see Figure S22 for DNA sequence design). The sample was kept on ice in the dark until use. About 10 min prior to each experiment, a portion of the sample was diluted to a DX tile concentration of ~200 pM in 1×TAE-Mg²⁺ buffer. Then, the sample was immobilized on a streptavidin-coated microscope slide, and the excess sample flushed away with 1×TAE-Mg²⁺ buffer, followed by imaging buffer. In the case of single-molecule competition experiments, the buffer was supplemented with 0.5-320 μM of inhibitor DNA molecule **I** (5'-AAT TTC ACT ATT TTT TTT TTT TTT TTT TTT T). The inhibitor contains a stretch of 11 bases (labeled in red) complementary to the (5'-AT AGT GAA ATT) probe sequence of **Cy5-P*-1**, and was designed to compete with the Cy3-labeled swinging arm for hybridization to **Cy5-P*-1**.

4. Data analysis for smFRET: Figure S24 shows CCD images of representative fields of view from smFRET measurements. Analysis of single-molecule FRET trajectories and inhibition experiments was performed with custom-written IDL and MATLAB scripts as previously described (7). A given smFRET trajectory was used in subsequent analysis only if it (1) exhibited total fluorescence of Cy3 and Cy5 exceeding 500 counts/frame; (2) showed clear evidence of both Cy3 + Cy5; and (3) showed no evidence of multiple identical fluorophores, for example, multiple photobleaching steps or overlapping point-spread functions in the CCD image.

In the case of the full Cy3-Cy5-BHQ-2 swinging arm complex, which exhibits a wider variety of behaviors due to the presence of three labels (any of which may be missing or oxidized prior to observation), other observed behaviors were catalogued with interpretations as to the most likely cause of each behavior (Figure S25A). FRET histograms were constructed from the first 400 frames of each molecule. The equilibrium fraction of high-FRET molecules ($f_{high-FRET}$) was determined by thresholding with a cutoff of FRET = 0.5, which is approximately halfway between the low- and high-FRET states (or quenched and fluorescent states, in the case of the Cy3-Cy5-BHQ2 complex) of 0-0.2 and ~1.0, respectively.

Semi-swinging arm complexes within a given sample exhibited heterogeneous FRET dynamics. Histograms of the number of observed semi-swinging arm complexes spending a given fraction of the time in the high-FRET state are shown in Figure S26 (in contrast, the FRET histograms in Figure 2B represent the total fraction of time spent by *all* complexes of each type in a given FRET state).

5. Determination of equilibrium dissociation constants of DNA hybridization for probe strands for model swinging arm structures by ensemble FRET. Ensemble FRET experiments were performed at 20 °C on an Aminco-Bowman Series 2 Luminescence Spectrometer with an excitation wavelength of 500 nm (0.5 nm bandwidth). As with smFRET experiments, all ensemble FRET measurements were performed in an imaging buffer consisting of 1×TAE-Mg²⁺ + OSS.

To determine the equilibrium dissociation constant (K_d) of hybridization between **Cy3-poly(T)₂₀** (5'-Cy3-TTT TTC ACT ATT TTT TTT TTT TTT TTT TTT TTT) and **Cy5-P*-1** or **BHQ2-P*-2**, 0.5 μM **Cy3-poly(T)₂₀** was mixed with 0-8 μM of **Cy5-P*-1** or **BHQ2-P*-2** (all are final concentrations), resulting in quenching of Cy3 as determined from fluorescence emission scans. To simulate the duplex that normally holds **Cy5-P*-1** or **BHQ2-P*-2** on the DX tile, a twofold excess of the appropriate capture sequence (**CP-1:** 5'-GGA GGG AGG G; or **CP-2:** 5'-CCA GCC AGC C) was added to each reaction prior to mixing with **Cy3-poly(T)₂₀**. Reactions were incubated in the dark at room temperature for 5 min, at which point the hybridization had reached equilibrium as verified by successive fluorescence measurements on the same sample. The intensity of Cy3 fluorescence was plotted as a function of **Cy5-P*-1** or **BHQ2-P*-2** concentration and fit with the equation:

$$y = A \frac{(x+T+K_d)-\sqrt{(-x-T-K_d)^2-4Tx}}{2} + y_0 \quad (1)$$

where T is the concentration of **Cy3-poly(T)₂₀**, x is the concentration of **Cy5-P*-1** or **BHQ2-P*-2**, and A and y_0 are constants, yielding K_d estimates of ~0.3 μM for both reactions (Figure S27A). The use of this exact equation was necessary because the relatively large concentration of **Cy3-poly(T)₂₀** resulted in significant differences between free and total concentrations of the reactants(8).

6. Determination of the inhibition constant of an inhibitor DNA that blocks hybridization of the swinging arm: To determine the inhibition constant K_I of the inhibitor I , 0.5 μM Cy3-poly(T)₂₀ was mixed with 0.5 μM of **Cy5-P*-1** or **BHQ2-P*-2** (pre-bound to **CP-1** or **CP-2**, as described above), and 0-3.2 μM of I was added, resulting in a concentration-dependent dequenching of Cy3. The intensity of Cy3 fluorescence was plotted as a function of inhibitor concentration and fit to the logistic function:

$$y = \frac{M-N}{1+I/IC_{50}} + N \quad (2)$$

where M and N are constants and I is the inhibitor concentration, to determine IC_{50} . The true K_I was estimated to be $\sim 0.06 \mu\text{M}$ (Figure S27B) using the correction(9):

$$K_I = \frac{IC_{50}}{1 + \frac{T(r_0+2)}{2 \times K_d(r_0+1)}} - K_d \left(\frac{r_0}{r_0+2} \right) \quad (3)$$

where r_0 is the ratio of bound to free **Cy3-poly(T)₂₀** in the absence of inhibitor.

The 5-fold increase in the binding affinity of the inhibitor ($\sim 0.06 \mu\text{M}$) compared to Cy5-P*-1 ($\sim 0.3 \mu\text{M}$), provided by the 2 extra base-pairs, suffices to inhibit hybridization between the swinging arm and Cy5-P*-1, even at the shortest anchor spacing of 7 nm (see Section 7 and Figure S28).

7. Estimation of effective concentration. The local effective concentration $C_{eff,meas}$ of the swinging arm was estimated by plotting the fraction of time spent in the high-FRET state as a function of inhibitor concentration and fitting with the following equation(10):

$$f_{high-FRET} = A * \frac{C_{eff,meas}}{C_{eff,meas} + K_d * \left(1 + \frac{I}{K_I} \right)} + y_0 \quad (4)$$

where A and y_0 are constants, I is the concentration of inhibitor, and K_d and K_I are the equilibrium dissociation and inhibition constants for **Cy5-P*-1** and the inhibitor, respectively, as determined by solution measurements (Figure S28). The estimated local effective concentration of the swinging arm in the vicinity of Cy5-P*-1 is $\sim 250 \mu\text{M}$ for the 7-nm complex and $2.7 \mu\text{M}$ for the 14-nm complex (Table S4).

Simulation of swinging arm conformation and prediction of local effective concentration. Metropolis Monte Carlo simulations (11) were performed using a recently published coarse-grained model of ssDNA that explicitly accounts for excluded volume effects and intra-strand electrostatic repulsion (12). Using the parameterization for 10 mM Mg²⁺ (virtual bond angle $\theta = 57.8^\circ$, virtual bond length $l_0 = 0.369$ nm, radii of closest approach $a = d = 0.56$ nm, and charge renormalization factor $f = 0.229$) and prohibiting chain excursions below the plane of the DX tile, 10⁶ chain conformations were sampled. A conformation was considered compatible with hybridization if it placed the proximal end of the sticky-ended probe of the poly(T)₂₀ arm within a hemispherical shell S representing the volume swept out by the proximal end of the probe sequence of Cy5-P*-1 (Figure S29). The inner and outer radii of S were estimated as $3.4 + 1.4 \pm 1.4$ nm, taking into account the rigid 10-bp anchor duplex and two 3T linkers on either side of the duplex, assuming that the 3T linker distal to the tile is rotationally unhindered and using a wormlike chain model with a persistence length of 1 nm to predict the root-mean-square end-to-end distance of ssDNA(13). The predicted local effective concentration ($C_{\text{eff,pred}}$) was calculated as:

$$C_{\text{eff,pred}} = \frac{f_{\text{hyb}}}{N_A \times V_S} \quad (5)$$

where f_{hyb} is the fraction of conformations compatible with hybridization, N_A is Avogadro's number and V_S is the volume of S in liters. We find that the value of $C_{\text{eff,pred}}$ is rather insensitive to the thickness of S , since any change will affect f_{hyb} and V_S approximately proportionally. The predicted local effective concentration of the swinging arm at the two closest distances is shown in Table S4: ~ 607 μM for the 7-nm complex, and 4.7 μM for 14-nm complex.

To model the double-stranded poly(T)₂₀ + poly(A)₂₀ arm (Fig. S54), the calculations were performed in an identical manner, except that the swinging arm was instead modeled as a rigid rod of length 6.8 nm (B-type DNA, 20 bp) that isotropically explores a spherical section bounded by a minimum angle φ_{\min} above the plane of the tile.

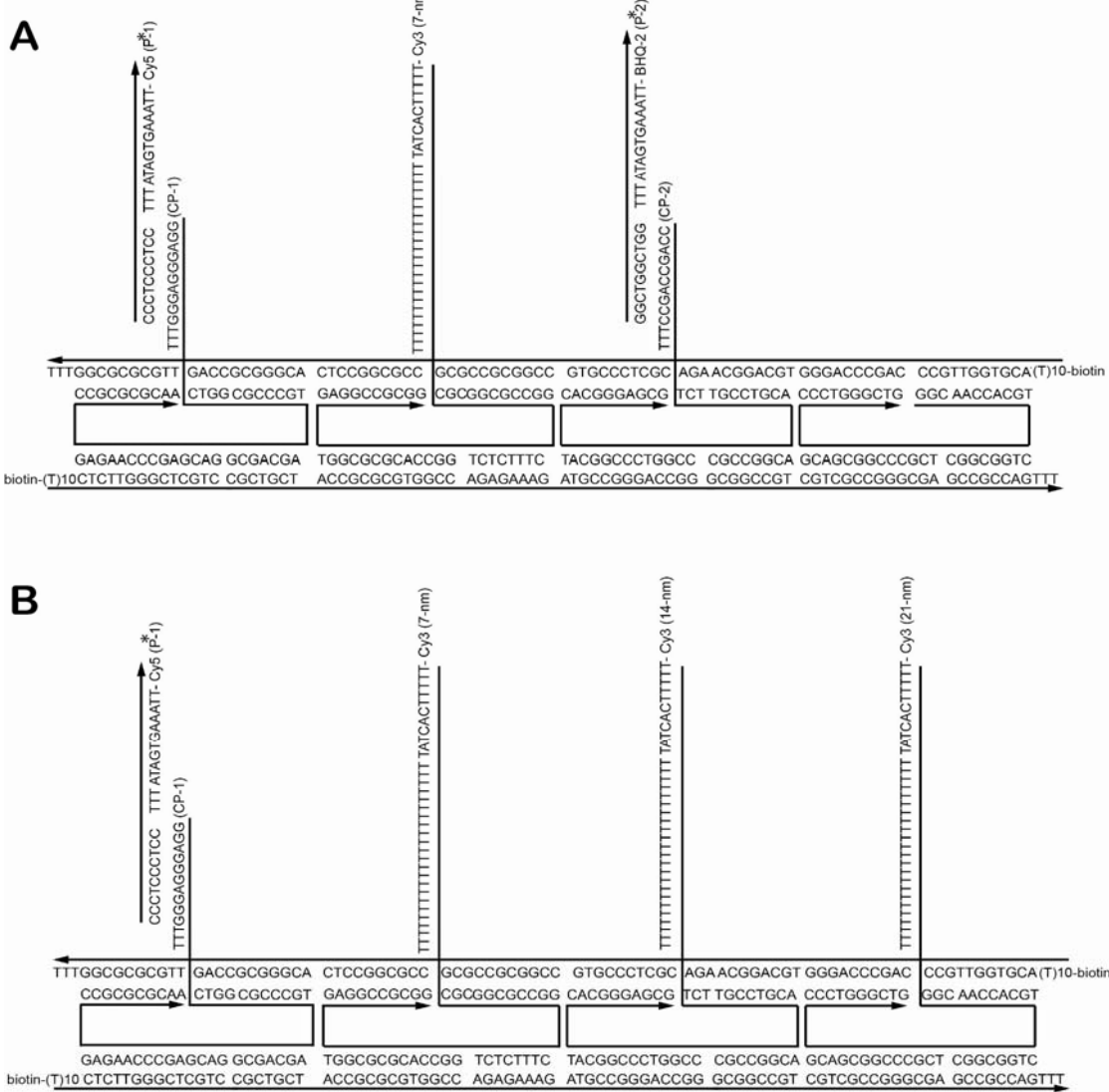


Figure S22. Sequence maps of the DNA-only models of swinging arm structures for single-molecule FRET experiments. (A) Cy3-Cy5-BHQ-2 swinging arm complex, in which the Cy5, Cy3 and BHQ-2 labeled strands are designed to extend from the same surface of the tile, with 7 nm between their anchor positions. The 5'-extension of the Cy3-labeled poly(T)₂₀ strand is complementary to the 3'-extensions on P*-1 and P*-2, and is designed to swing between the two binding sites in analogy to the G6pDH-NAD⁺-MDH system (Figure S3), resulting in energy transfer from Cy3 to Cy5 or quenching by BHQ-2. **(B)** Cy3-Cy5 semi-swinging arm complex, designed to test the distance dependence of binding mediated by the poly(T)₂₀ in analogy to the systems in Figures S1 and S2. Only one of three scaffold strands (7, 14, or 21 nm from the P*-1 anchor site) bears the 5'-Cy3-poly(T)₂₀ extension in a given complex design.

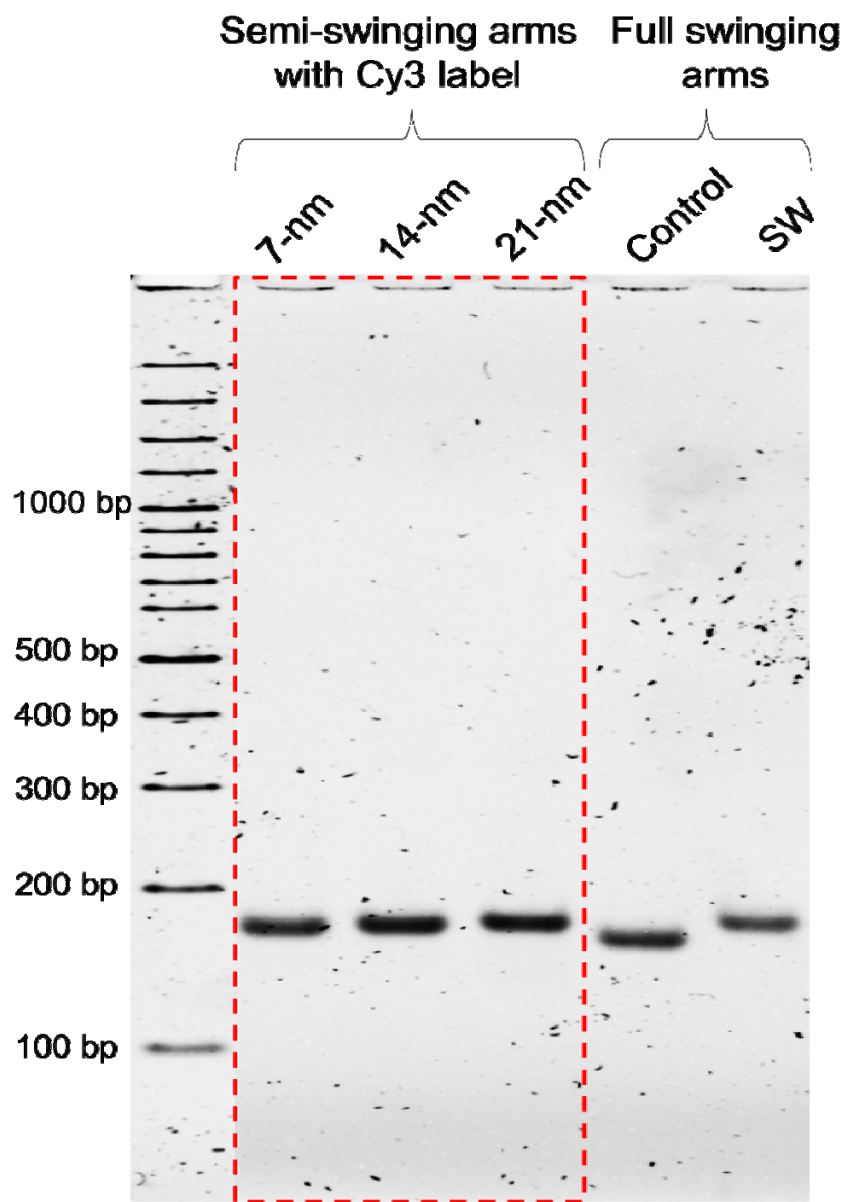


Figure S23. Native 3% PAGE characterization of assembled DNA structures shown in Figure S22. The left three lanes show the Cy3-labeled semi-swinging arms structures with 7, 14 and 21 nm between anchor sites, corresponding to the structures in Figure S22B. The fourth lane from the left is a control structure with the Cy3-poly(T)₂₀ as shown in Figure S22 A but lacking the 3'-extensions of CP1 and CP2. The fifth lane is the same structure as lane 4 but with the capture strands CP1 and CP2.

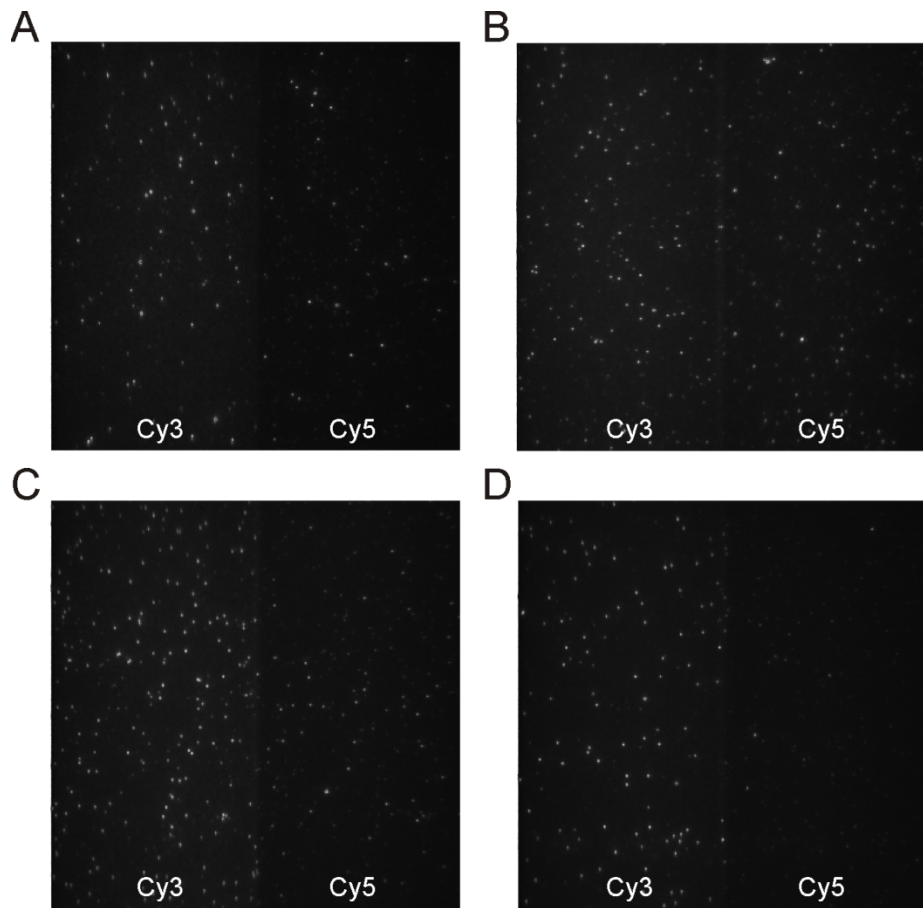


Figure S24. Representative fields of view from smFRET measurements. (A) Cy3-Cy5-BHQ-2 swinging arm complex (as shown in Figure S22A). (B-D) Cy3/Cy5 labeled semi-swinging arm complexes (as shown in Figure S22B) with distances of 7 nm (B), 14 nm (C), and 21 nm (D) between the anchor positions of the **Cy3 labeled poly(T)₂₀** and the **Cy5 labeled P-1 strand**.

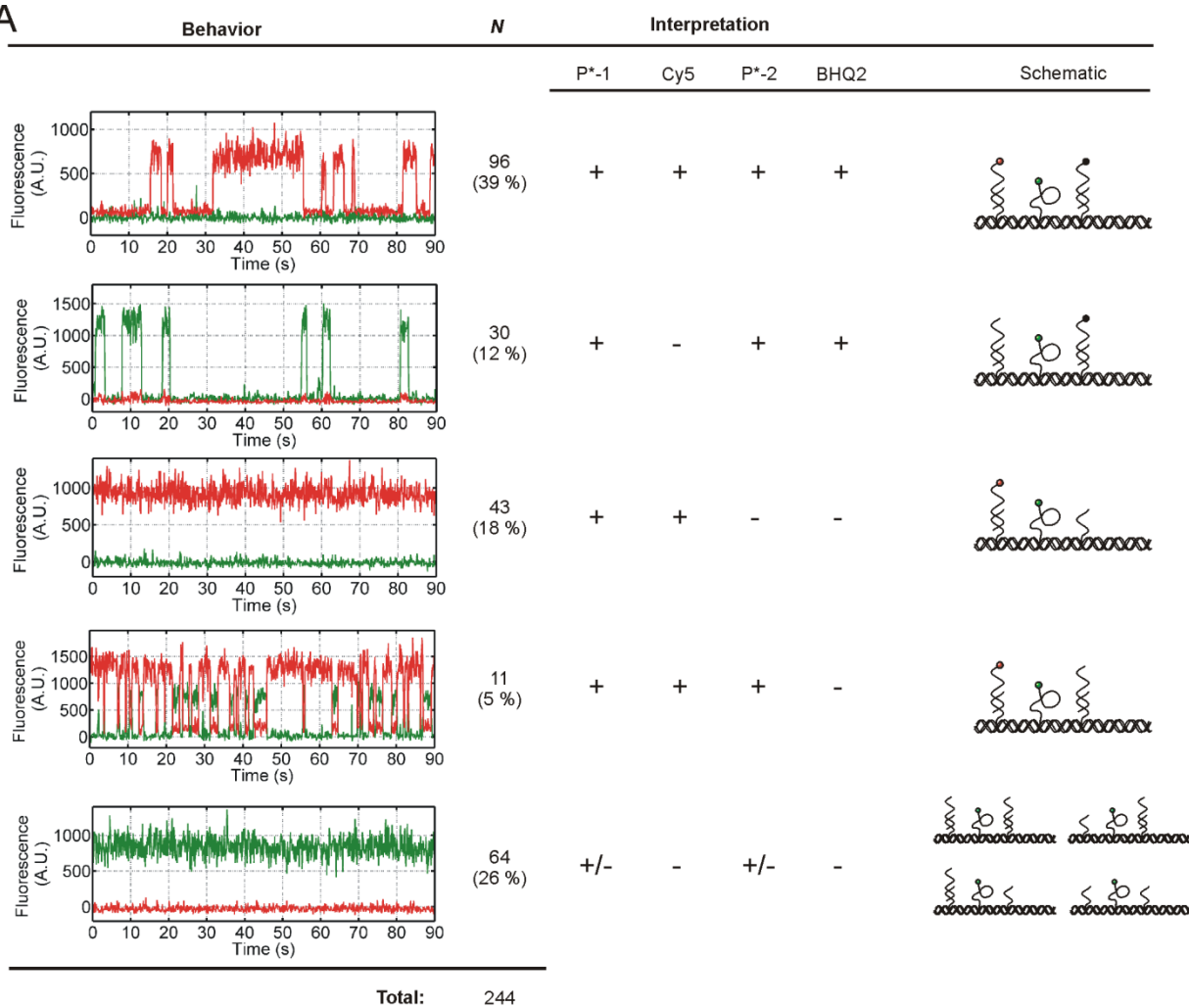
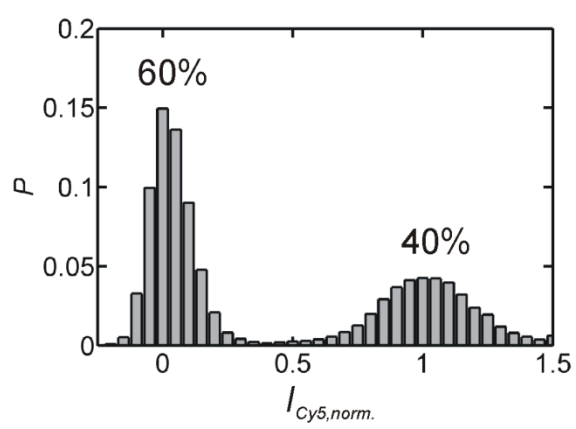
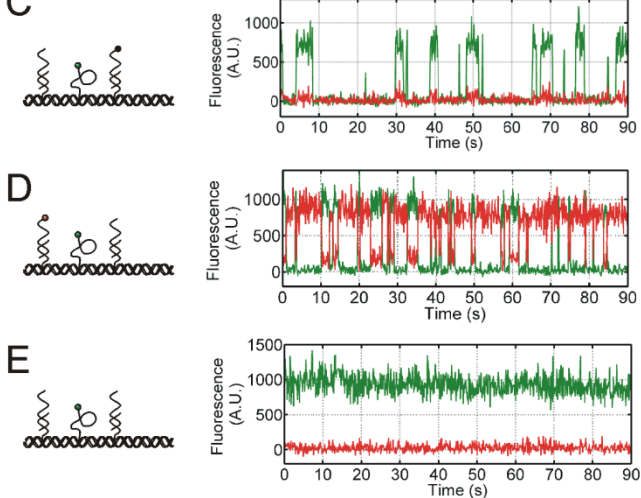
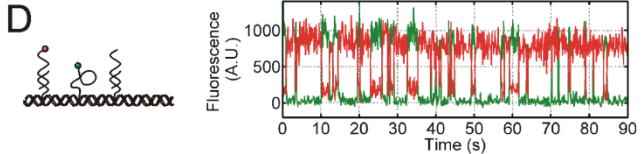
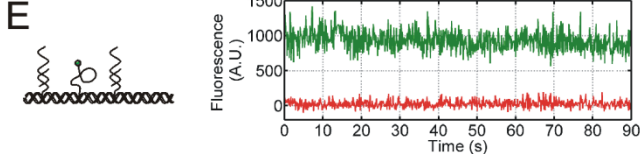
A**B****C****D****E**

Figure S25. smFRET characterization of fully assembled swinging arm structures with energy transfer between Cy3-Cy5 and Cy3-BHQ-2. (A) Tabulated smFRET behaviors of full Cy3-Cy5-BHQ-2 swinging arm complexes, along with representative single-molecule fluorescence intensity trajectories (Cy3 in green, Cy5 in red) and the interpretation regarding the presence or absence of **P*-1**, **Cy5**, **P*-2**, and **BHQ-2**. Complexes with **P*-2** and **BHQ-2** but lacking **P*-1** are not likely to be observable since Cy3 fluorescence will be strongly quenched the majority of the time. (B) Histogram of normalized Cy5 intensity for complexes exhibiting alternating high-FRET and quenched states (i.e., “++++” behavior in (A), interpreted as the fully assembled and three-dye labeled complexes). Only the first 20 s of each trajectory whose length exceeded 20 s were included ($N = 81$). (C)-(E) Representative single-molecule intensity vs. time trajectories of control complexes prepared with (C) unlabeled **P*-1**, (D) unlabeled **P*-2**, or (E) unlabeled **P*-1** and **P*-2**.

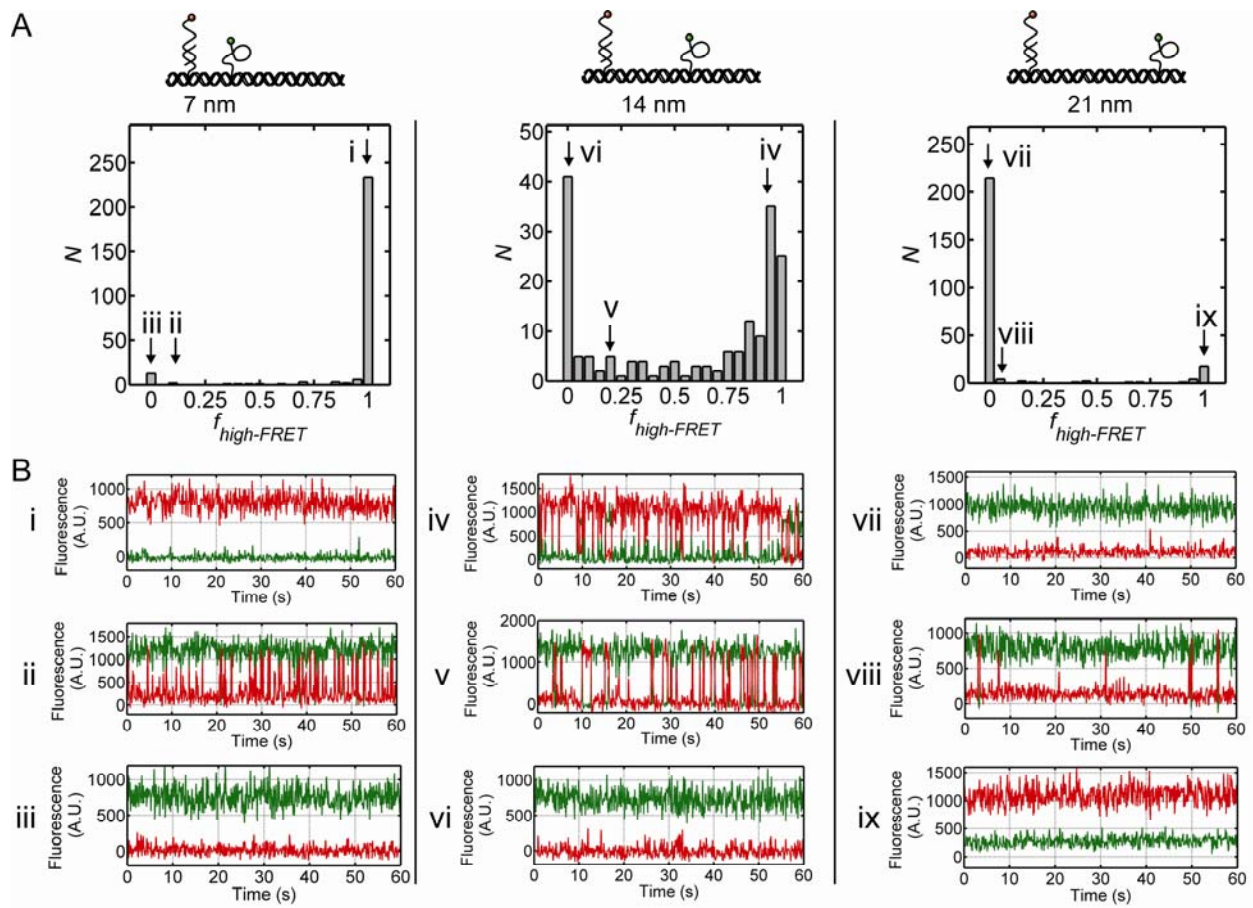


Figure S26. Heterogeneous behavior of single semi-swinging arm complexes. (A) Histograms of the number of observed complexes of each type ($d = 7, 14$, or 21 nm) spending a given fraction of time in the high-FRET state ($\text{FRET} > 0.5$). The vertical arrows show the positions of the corresponding molecules whose smFRET trajectories are shown in panel B (i-ix) (B) Selected smFRET trajectories showing the diversity of behaviors exhibited by individual complexes of each type. The majority of complexes with a spacing of 7 nm show high FRET, slightly more than half (~ 60%) of the complexes with a 14 nm spacing show high FRET, and only a small fraction (< 10%) of the complexes with a 21 nm spacing show high FRET. Thus, binding between the swinging arm and target probe is most efficient with a 7 nm spacing, somewhat less efficient at 14 nm, and generally not possible at 21 nm.

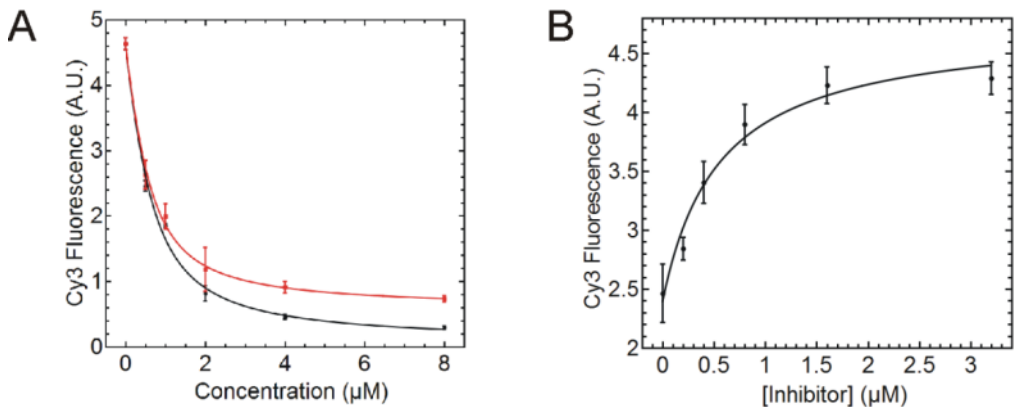


Figure S27. Determination of binding constants of **Cy5-P*-1 and **BHQ2-P*-2**, and the inhibition constant of **I**.** (A) Ensemble FRET binding titration of free **Cy3-poly(T)₂₀** with **Cy5-P*-1** (red) and **BHQ2-P*-2** (black) in 1×TAE-Mg²⁺. The lines are nonlinear least-squares fits yielding K_d values of $0.31 \pm 0.05 \mu\text{M}$ for **Cy5-P*-1** and $0.36 \pm 0.08 \mu\text{M}$ for **BHQ2-P*-2**. (B) Ensemble inhibition of binding between **Cy3-poly(T)₂₀** and **Cy5-P*-1** by titration with **I** (which forms an 11-bp duplex with **Cy5-P*-1**). Dequenching of Cy3 is modeled by a logistic function (line) yielding an IC₅₀ of $0.47 \pm 0.24 \mu\text{M}$ and an estimated K_I of $0.06 \mu\text{M}$ (calculated as described in the Methods section). Error bars shown are 1 standard error of the mean from three independent measurements.

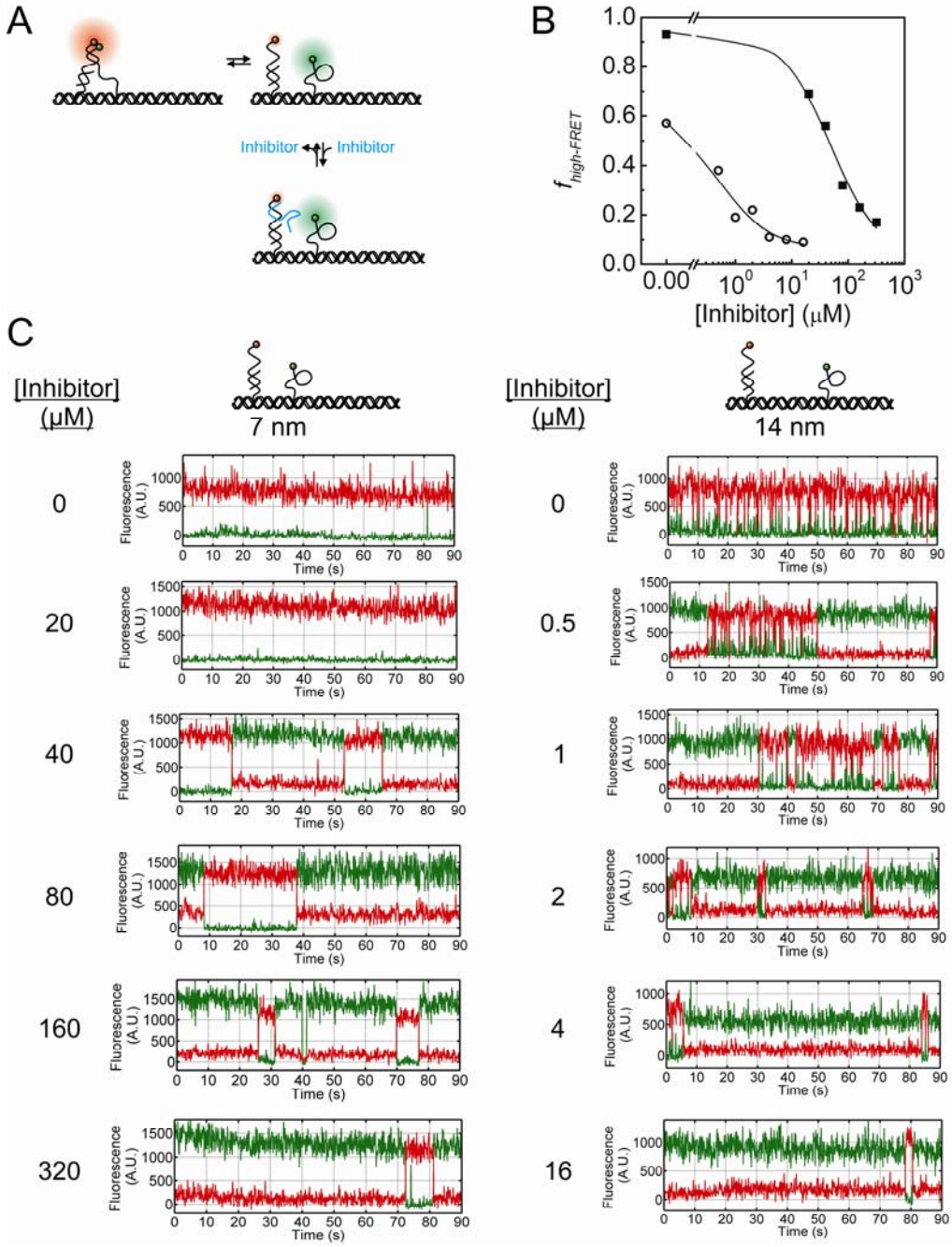


Figure S28. smFRET competition assays. **(A)** Schematic illustration of smFRET competition assays for the determination of local effective swinging arm concentration. **(B)** Determination of the local effective concentration of the Cy3-arm in the vicinity of a **Cy5-P*-1** probe displaced by 7 nm (squares) or 14 nm (circles). The fraction of Cy5-labeled probe hybridized to the Cy3-labeled arm ($K_d \sim 0.31 \mu\text{M}$) in the presence of varying concentrations of Inhibitor strand ($K_i \sim 0.06 \mu\text{M}$) is fit with a competitive binding model (solid lines) as described in the Methods, yielding the effective concentration estimates in Table S4. **(C)** Representative single-molecule trajectories for the $d = 7 \text{ nm}$ and $d = 14 \text{ nm}$ complexes in the presence of varying concentrations of inhibitor.

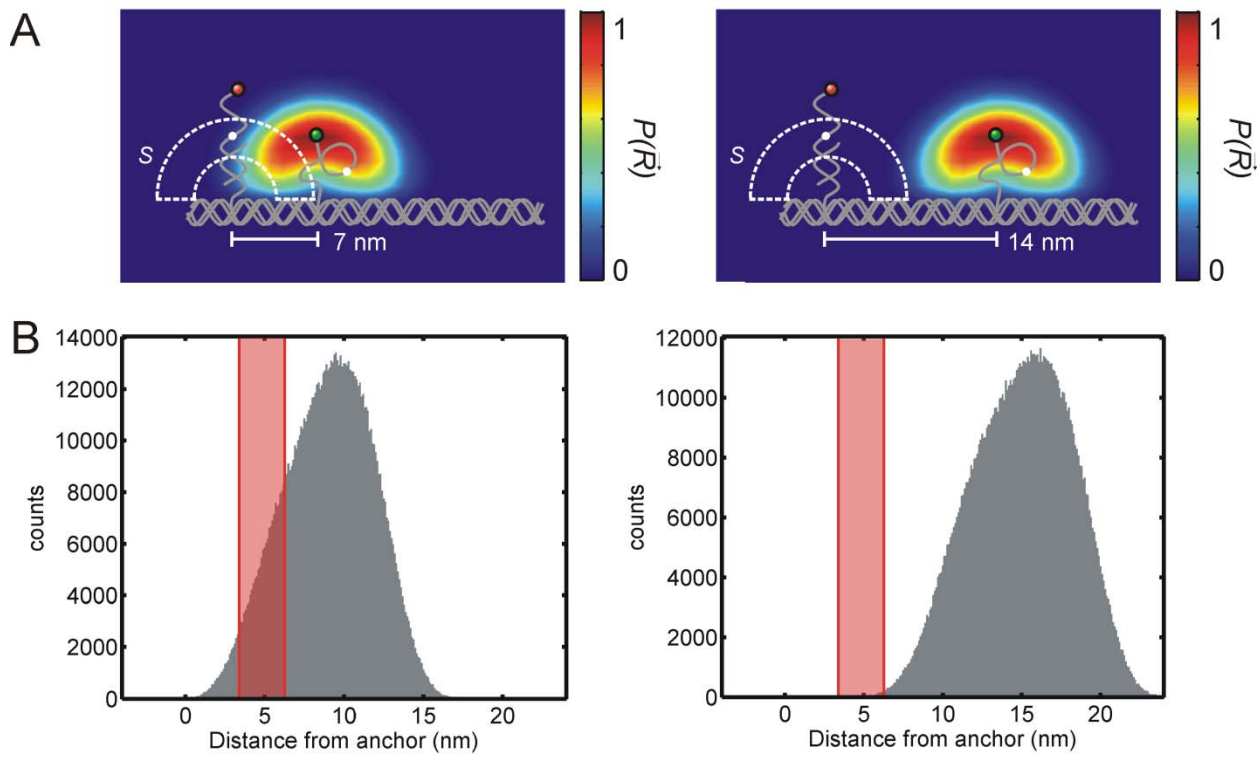


Figure S29. Modeling conformations and local effective concentration of the swinging arm.

(A) Schematic illustration of the model. The swinging arm (Cy3 labeled) is modeled as a freely rotating chain using the Metropolis algorithm, giving rise to a distribution of conformations. A 5-nm-wide cross-section of the conformational probability distribution is represented by a rainbow color map. The Cy5-labeled probe is assumed to evenly explore a hemispherical shell S (white dotted lines). A conformation is considered compatible with hybridization if it can bring the two proximal ends of the arm-probe duplex (white circles) into close proximity. (B) Histograms of the distance between the swinging arm and the anchor site for the Cy5-labeled probe as determined by modeling of 10^6 conformations. The red shaded region corresponds to the hemispherical shell S , the region compatible with hybridization.

Table S4. Comparison of predicted and measured local effective concentration of the swinging arm in the vicinity of Cy5-P*-1 (DNA-only model structures)

	$d = 7 \text{ nm}$	$d = 14 \text{ nm}$
$C_{\text{eff},\text{pred}} (\mu\text{M})$	607	4.5
$C_{\text{eff},\text{meas}} (\mu\text{M})$	250	2.7

$C_{\text{eff},\text{pred}}$ is the predicted local effective concentration of the Cy3-arm in the vicinity of the **Cy5-P*-1 probe**, calculated from the Metropolis Monte Carlo simulations as described in Methods and Figure S29. $C_{\text{eff},\text{meas}}$ is the local concentration as estimated from smFRET competition assays (Figure S28).

Section 7: Enzyme activity assay methods and Michaelis-Menten analysis

- 1) Free enzymes:** The activity of freely diffusing dehydrogenases (G6pDH and MDH) is evaluated by the rate of reduction of NAD⁺ to NADH (for G6pDH) or oxidation of NADH to NAD⁺ (for MDH) as monitored by the change in absorbance at 340 nm.
- 2) Semi-swinging arm structures:** 100 nM G6pDH-NAD⁺ or MDH-NAD⁺ semi-swinging arm structures (with one enzyme and the swinging arm anchored 7, 14 or 21 nm apart on the DX tile) were prepared into 100 μL total volume with substrate in 1×TBS buffer (pH 7.6) for the activity assay. The assay was performed using a SpectraMax M5 96-well plate reader (Molecular Device, Sunnyvale, CA) following method outlined in (14). The activity of semi-swinging arm structures was measured using a coupled assay utilizing PMS (phenazine methosulfate) and resazurin in which PMS first oxidizes NADH to NAD⁺, then reduces resazurin to resorufin with the appearance of a fluorescence signal (excitation max ~ 544 nm, emission max ~ 590 nm), as shown in Figure S30A. For a typical reaction, 100 nM G6pDH-NAD⁺ structure was incubated with 1 mM glucose-6-phosphate (G6p), 500 μM PMS and 500 μM resazurin; and 100 nM MDH-NAD⁺ structure was assayed with 1 mM malic acid, 500 μM PMS and resazurin and 100 nM oxaloacetate decarboxylase (OAD) in 1×TBS buffer (pH 7.5).
- 3) Fully assembled swinging arm structures:** 100 μL reactions containing 100 nM complete G6pDH-NAD⁺-MDH swinging arm structures were assayed with 1 mM G6p, 1 mM oxaloacetic acid (OAA) in 100 mM HEPES buffer (pH 8) as shown in Figure S30B. The overall activity of the cascade was measured by monitoring the absorbance decrease at 250 nm due to the reduction of OAA to malic acid (Figure S30C). NAD⁺ and NADH have slight difference (~ 10%) at 250 nm as compared to the change between OAA and pyruvate. For example, OD at 250 nm decreases ~ 0.05 for 40 μM NAD⁺ converting to NADH, while the G6pDH/MDH cascade reaction with the same concentration of NAD⁺ causes an OD decrease of ~ 0.5 in half an hour due to the conversion of OAA to pyruvate. In the experiments, we kept NAD⁺ at low micromolar concentration to minimize its interference with the assay. Mg²⁺ and Tris were removed from the solution using size exclusion FPLC with 100 mM HEPES (pH 8) because they would induce the auto beta-decarboxylation of OAA to pyruvate (Figure S31) (15).

4) Lactate dehydrogenase (LDH) competition assay: The activity of LDH was characterized using a coupled assay of lactate oxidase (LOX)-horseradish peroxidase (HRP), in which LOX first oxidizes lactate produced by LDH to hydrogen peroxide, then HRP catalyzes the oxidation of Amplex Red to the strongly fluorescent product resorufin (ex 544 nm/ em 590 nm) using hydrogen peroxide (16, 17). A typical LDH competition assay was performed with 100- μ L reactions containing 100 nM each of LDH and the G6pDH-NAD⁺-MDH structure 1 mM each of Glucose-6-phosphate, oxaloacetic acid and pyruvate, 10 nM each of LOX and HRP, and 200 μ M Amplex Red in 100 mM HEPES (pH 8) buffer.

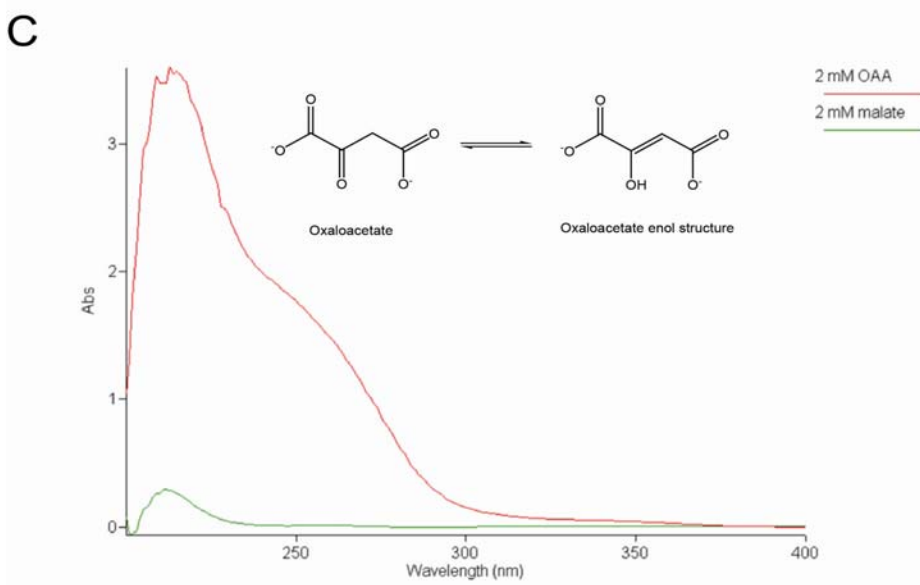
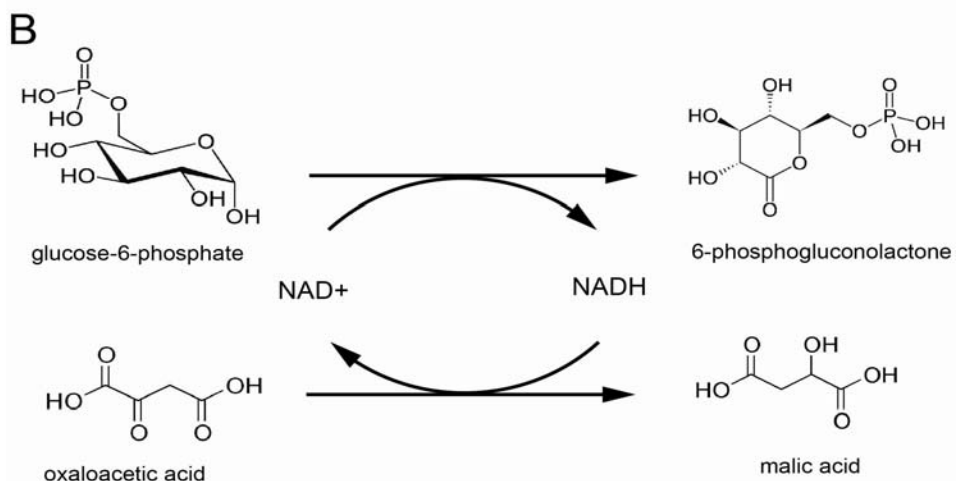
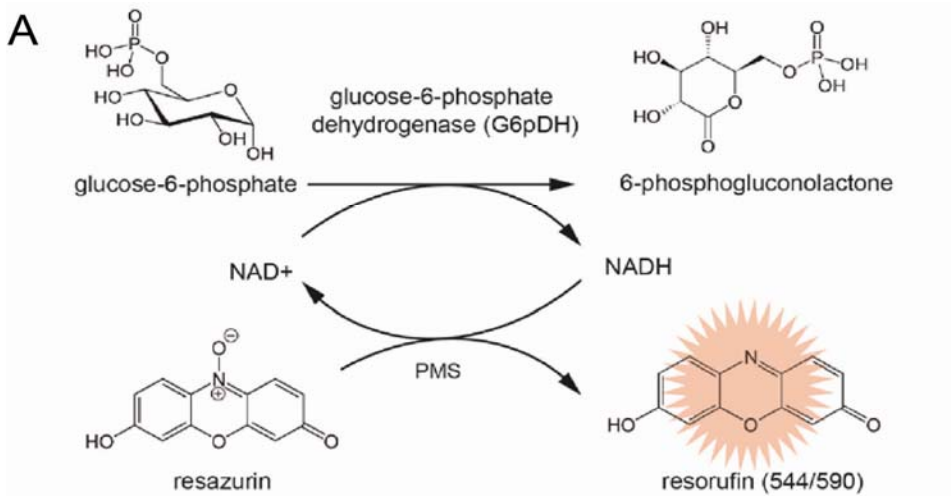


Figure S30. Reaction schemes for detection of enzymatic activity in the G6pDH-NAD⁺ semi-swinging arm structure and the G6pDH-NAD⁺-MDH full swinging arm structure. (A) PMS/resazurin coupled assay for G6pDH-NAD⁺ activity. NAD⁺ is first reduced to NADH by G6pDH. Next, PMS catalyzes electron transfer from NADH to resazurin producing the strongly fluorescent product resorufin with an emission maximum ~590 nm. MDH-NAD⁺ activity is assayed similarly using malic acid as the substrate. (B) Assay for G6pDH catalyzes the oxidation of glucose-6-phosphate (G6p) and the reduction of NAD⁺ to NADH. Subsequently, MDH catalyzes the reduction of oxaloacetic acid (OAA) to malic acid using the NADH produced by G6pDH. (C) Oxaloacetic acid absorbs strongly at 250 nm due to its enol resonance structure, while malic acid has very little absorbance at 250 nm. The overall cascade activity of G6pDH-NAD⁺-MDH can be measured by monitoring the absorbance decrease at 250 nm due to the reduction of oxaloacetic acid to malic acid.

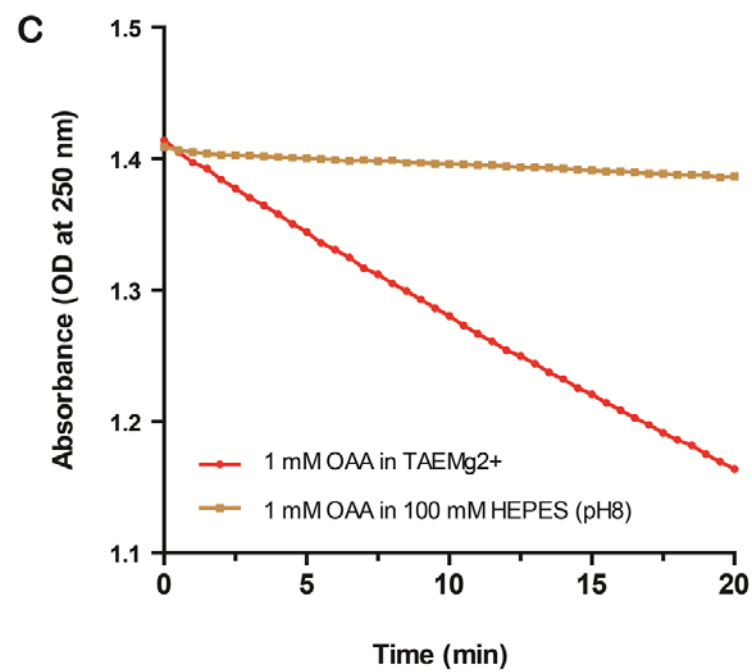
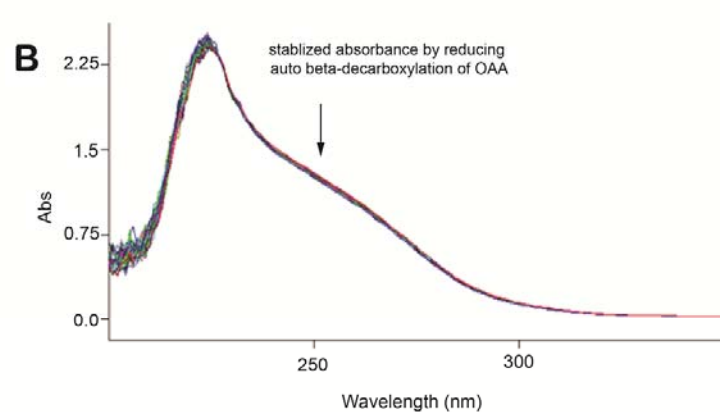
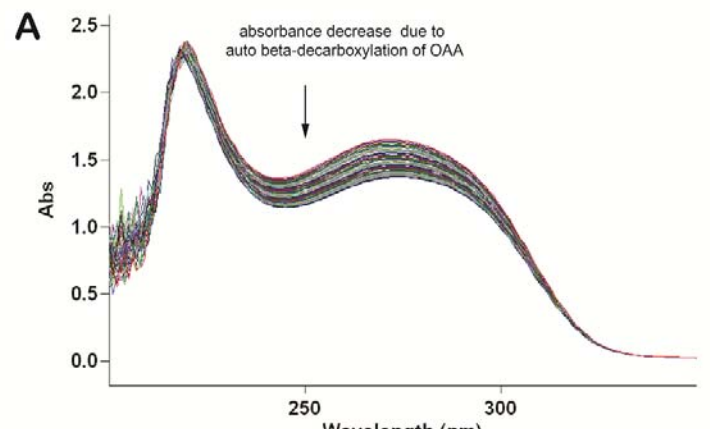


Figure S31. **(A)** Strong autocatalysis of 1 mM oxaloacetic acid (OAA) in pH 7.5, 1× TAE/Mg²⁺ buffer (12.5 mM MgCl₂), due to Mg²⁺- and primary amine-induced beta-decarboxylation of OAA to pyruvate. **(B)** Weak autocatalysis of 1 mM oxaloacetic acid in pH 8, 100 mM HEPES buffer. **(C)** Comparing the stability of OAA in 1×TAE/Mg²⁺ buffer and HEPES buffer. HEPES buffer was used in all enzyme activity assays involving oxaloacetic acid as substrate.

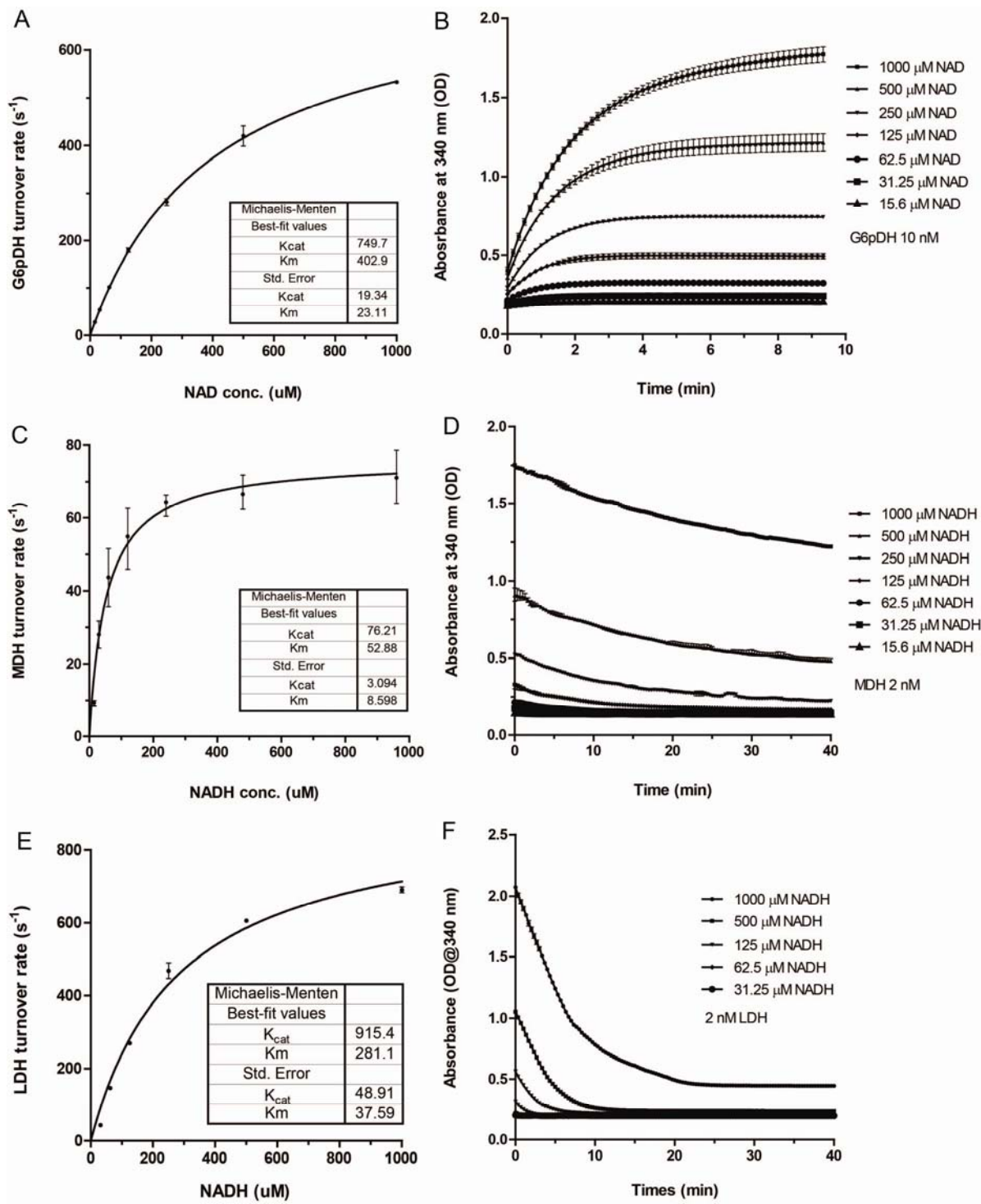


Figure S32. (A) Michaelis-Menten plot for determining the Michaelis constant of G6pDH with respect to NAD⁺. (B) Raw reaction traces of G6pDH in the presence of varying concentrations of NAD⁺ and a constant concentration of 1 mM glucose 6-phosphate. (C) Michaelis-Menten plot for determining the Michaelis constant of MDH with respect to NADH. (D) Raw reaction traces of MDH in the presence of varying concentrations of NADH and a constant concentration of 1 mM OAA. (E) Michaelis-Menten plot for determining the Michaelis constant of LDH with respect to NADH. (F) Raw reaction traces of LDH in the presence of varying concentrations of NADH and a constant concentration of 1 mM pyruvate. All the assays were performed with unmodified NAD⁺ or NADH molecules in 100 mM HEPES (pH 8) buffer.

Discussion: G6pDH has almost 10-fold higher k_{cat} than MDH, which suggests that in the G6pDH-NAD⁺-MDH swinging arm structure, the catalytic capacity of G6pDH is not fully exploited; in one catalytic cycle, G6pDH may need to wait for MDH to convert NADH back to NAD⁺ before catalyzing another reaction. At the same time, G6pDH has an ~8-fold larger K_m than MDH, suggesting that G6pDH requires a higher local concentration of cofactor than MDH for optimal activity. These differences in turnover number and Michaelis constant led us to design the G6pDH-NAD₂⁺-MDH₂ and G6pDH-NAD₄⁺-MDH₄ swinging arm structures as shown in Figure 3 (main text), which more effectively utilize the strengths of G6pDH and MDH.

LDH is used to compete with MDH for NADH to demonstrate the specificity of enzyme complexes organized by swinging arm structures. LDH has ~2-fold higher catalytic efficiency (k_{cat}/K_m value) than MDH. Hence, LDH can effectively compete with an equivalent concentration of freely diffusing MDH for NADH. However, the G6pDH-NAD⁺-MDH swinging arm structure reduces the ability of LDH to compete with MDH for NADH; as shown in Figure 4 (main text), LDH is effectively out-competed as a larger percentage of MDH is incorporated into swinging arm complexes.

Section 8: Dependence of G6pDH and MDH activity on the length, position, and orientation of the NAD⁺-modified swinging arm

Since the multi-enzyme complexes rely on local diffusive transport by the swinging arm, we expected their activity to depend on the length of the swinging arm, the distance between the anchor positions of the swinging arm and the enzyme, and the orientation of the swinging arm with respect to the protein anchor site on the DNA tile surface. We therefore investigated and optimized these parameters within our design space.

1. Dependence of the activity of G6PDH-NAD⁺ on the length of the NAD⁺-modified polyT swinging arm:

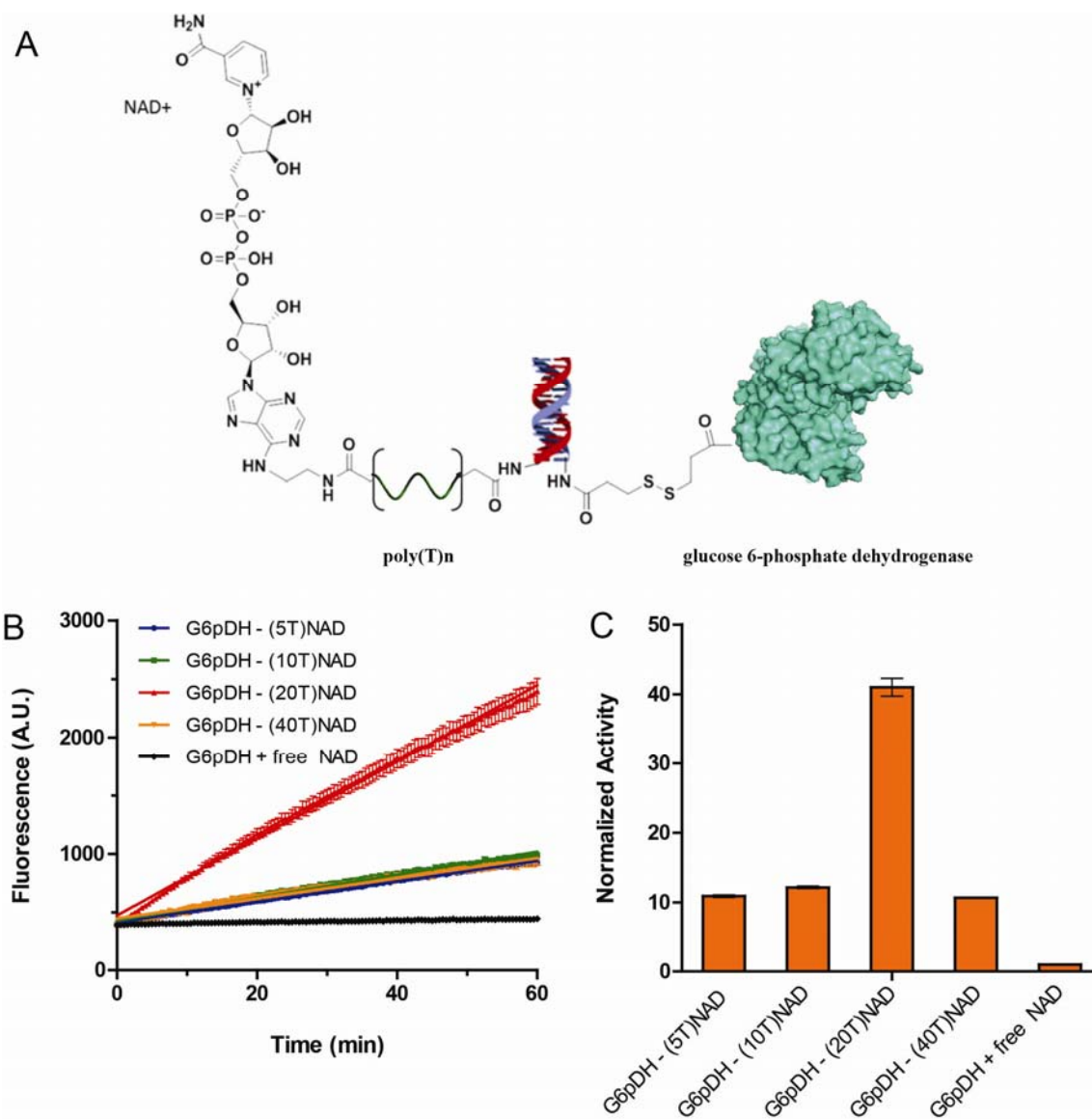


Figure S33. (A) Dependence of enzyme activity on arm length was measured by assembling an NAD⁺-modified DNA strand (the red strand, 5' AE-NAD⁺-(T)_n CCC TCC CTC C) with G6pDH labeled with the complementary strand (the blue strand, GGAGGGAGGGATTTT-G6pDH-3'). The length of the arm was varied ($n = 5, 10, 20, 40$ nt) to adjust the average distance between the NAD⁺ and the enzyme. (B) Raw activity traces for the G6pDH-NAD⁺ assembly shown in (A) using different arm lengths. Freely diffusing AE-NAD⁺ was also tested as a control to react with DNA conjugated G6pDH. (C) Normalized activity of the G6pDH-NAD⁺ arm assemblies shown in (A) as a function of arm length. Activity is normalized with respect to G6pDH in the presence of free AE-NAD⁺. Assay conditions: 100 nM G6pDH-NAD⁺ assembly, 1 mM G6p, 500 μ M PMS/resazurin in 1 \times TBS buffer (pH 7.5). The poly(T)₂₀ arm gives the highest activity of the lengths tested.

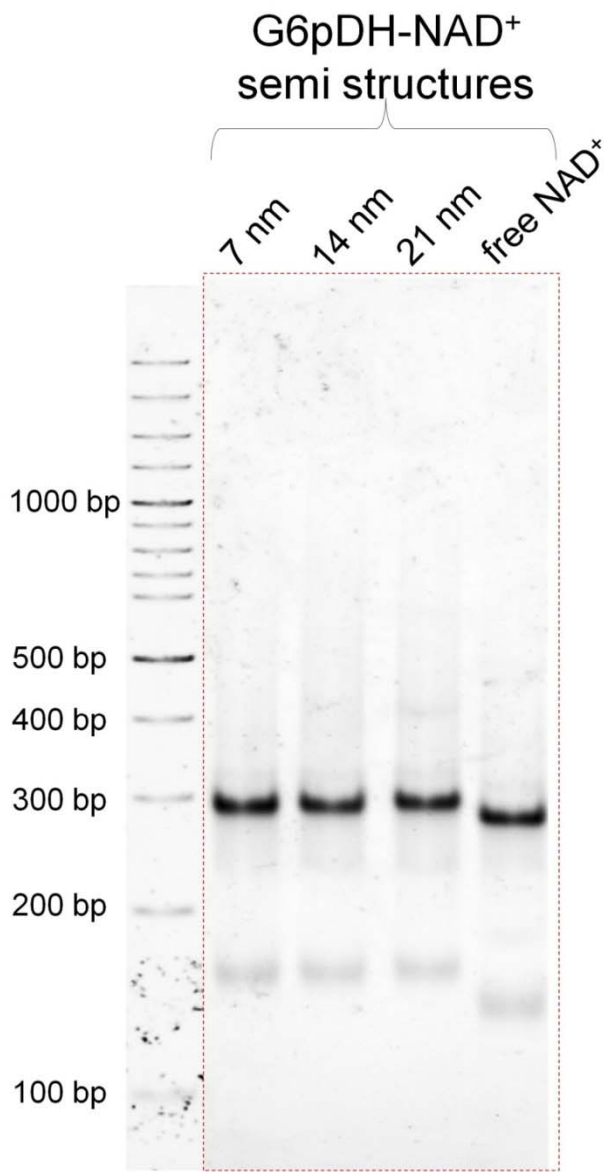


Figure S34. Native 3% PAGE characterization of G6pDH-NAD⁺ semi-swinging arm structures on DX DNA tiles with distances of 7, 14 and 21 nm between anchor sites. The dark major bands in the gel indicate that the structures (see Figure S1) assemble with high yield. The faint lower band in each lane is the DNA tile lacking G6pDH. A G6pDH-assembled DNA tile lacking the NAD⁺-labeled poly(T)₂₀ and mixed with free AE-NAD⁺ is also shown as a control.

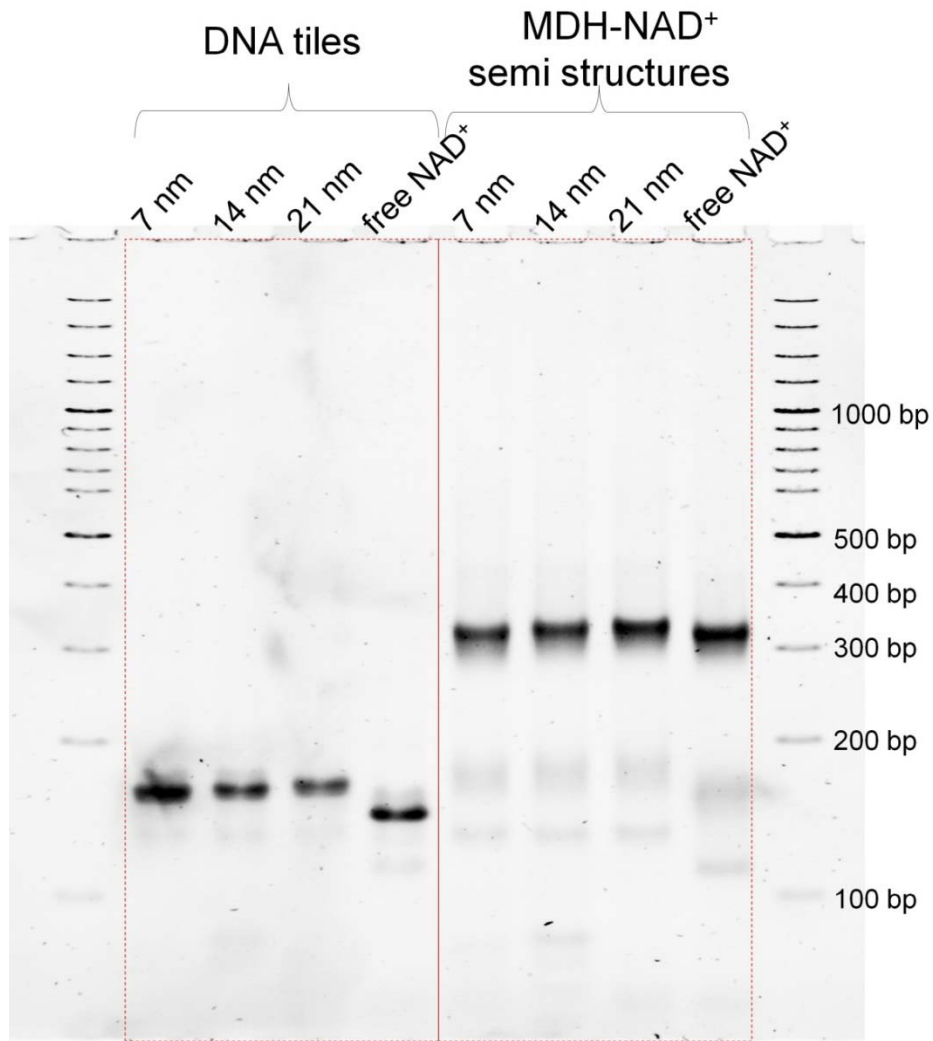


Figure S35. Native 3% PAGE characterization of MDH-NAD⁺ semi-swinging arm structures without (left) and with (right) assembled MDH. The dark major bands in the gel indicate that the structures (see Figure S2) assemble with high yield. The faint lower band in each MDH-NAD⁺ lane is the DNA tile lacking MDH. DX tiles lacking the NAD⁺-labeled swinging arm are also tested the presence of free AE-NAD⁺ as controls.

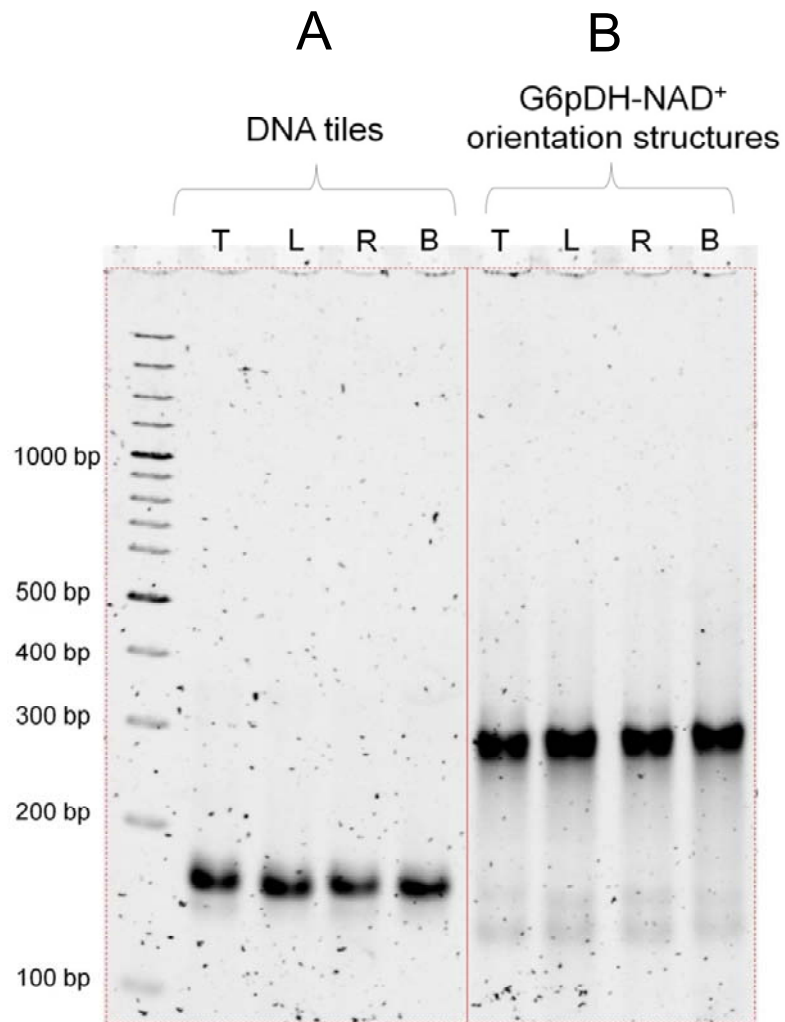


Figure S36. Native 3% PAGE characterization of (A) DNA tiles and (B) G6pDH-NAD⁺ semi-swinging arm assemblies with varying orientation of the NAD⁺ arm relative to the enzyme anchoring position (top): T (top/parallel), L(left), R (right) and B (bottom). Schematics of the structures are shown in Figure S39A and Figure 2E in the main text. The gel shows that all structures form with high yield.

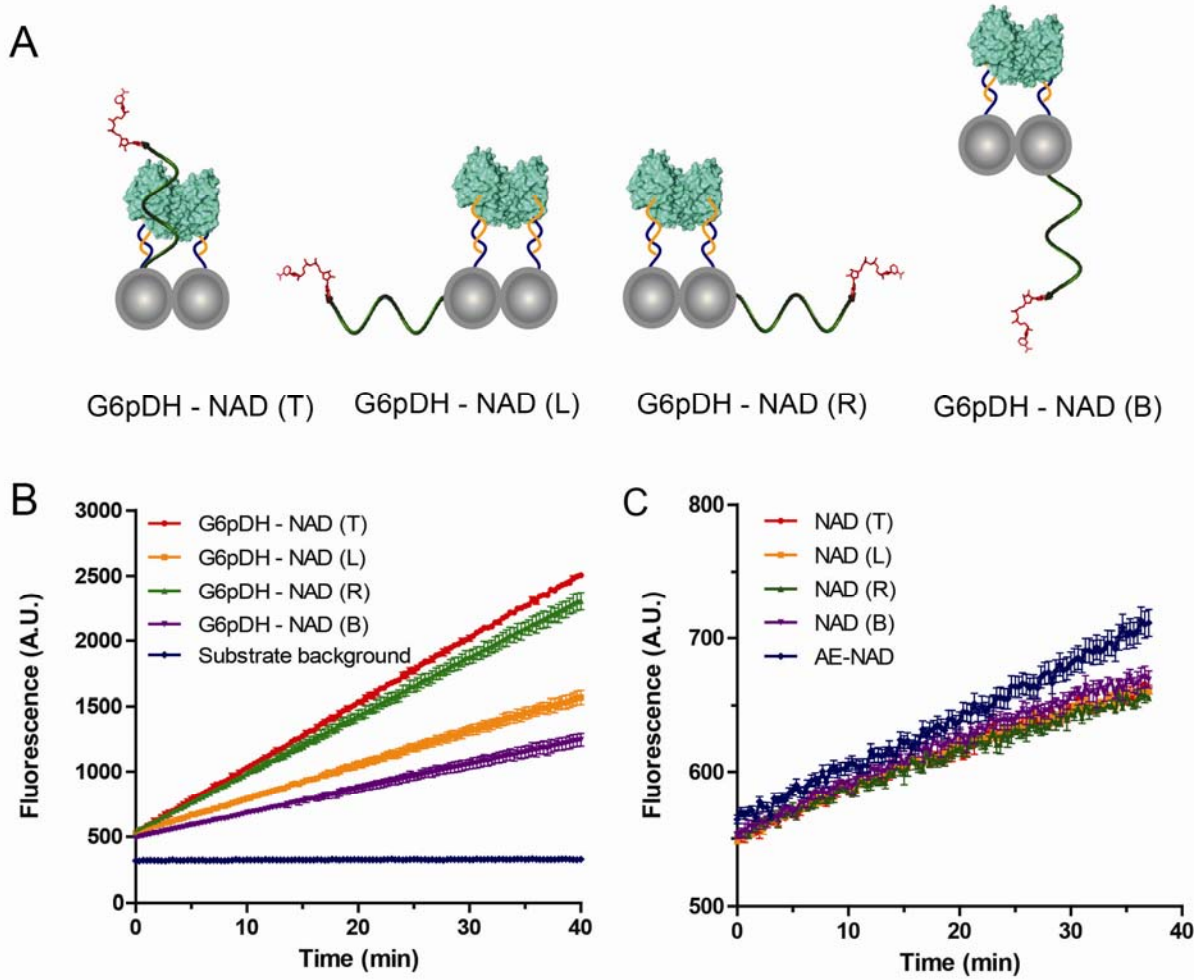


Figure S37. (A) Schematics of G6pDH-NAD⁺ semi-swinging arm assemblies with varying orientations of the anchoring position of the NAD⁺ arm relative to that of the protein (defined as “top”): T, parallel orientation on the top of the DNA scaffold; L, NAD⁺ arm oriented to the left; R, NAD⁺ arm oriented to the right; and B, NAD⁺ arm oriented to the bottom. These are viewed from the end of the DNA helices with the protein behind the NAD⁺ arm. (B) Raw fluorescence time traces of G6p oxidation catalyzed by G6pDH-NAD⁺ semi-swinging arm assemblies with different anchoring orientations. Assay conditions: 100 nM G6pDH-NAD⁺ semi-swinging arm assembly in the presence of 1 mM G6p and 500 μM PMS/resazurin in 1×TBS buffer (pH 7.5). (C) Raw fluorescence traces of 100 nM four DNA-NAD⁺ that are used in constructing orientation assemblies (shown in figure A), reacting with G6pDH in the freely diffusing systems. AE-NAD⁺ is also tested as control. Assay conditions: 100 nM G6pDH and DNA-NAD⁺ in the presence of 1 mM G6p and 500 μM PMS/resazurin in 1×TBS buffer (pH 7.5). The activity of all four conjugates is similar and comparable to that of free AE-NAD⁺.

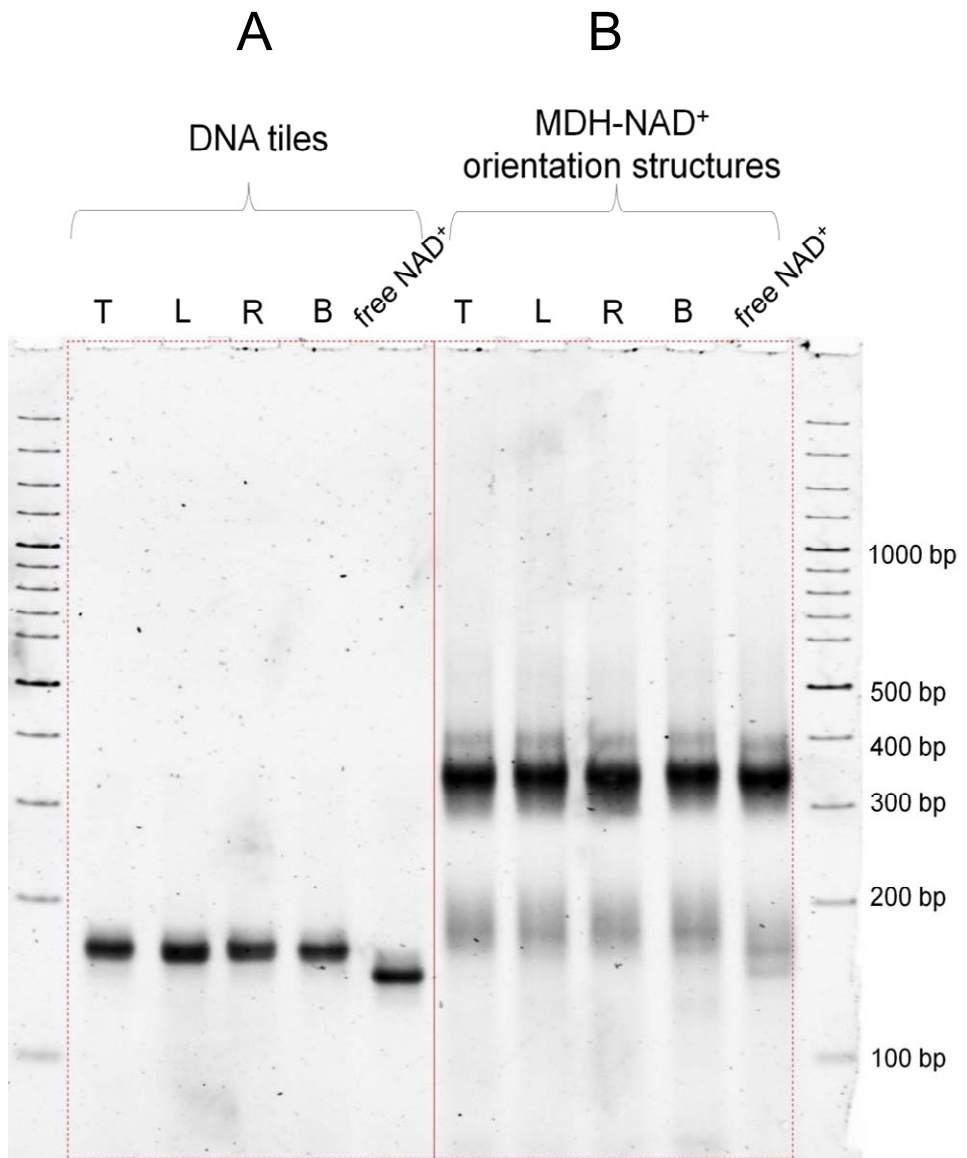


Figure S38. Native 3% PAGE characterization of (A) DNA tiles and (B) MDH-NAD⁺ semi-swinging arm structures with varying orientation of the NAD⁺ arm relative to the enzyme anchoring position (defined as “top”): T (top/parallel), L(left), R (right) and B (bottom). Schematics of the structures are shown in Figure S41A and Figure 2F in the main text. The gel shows that all structures form with high yield.

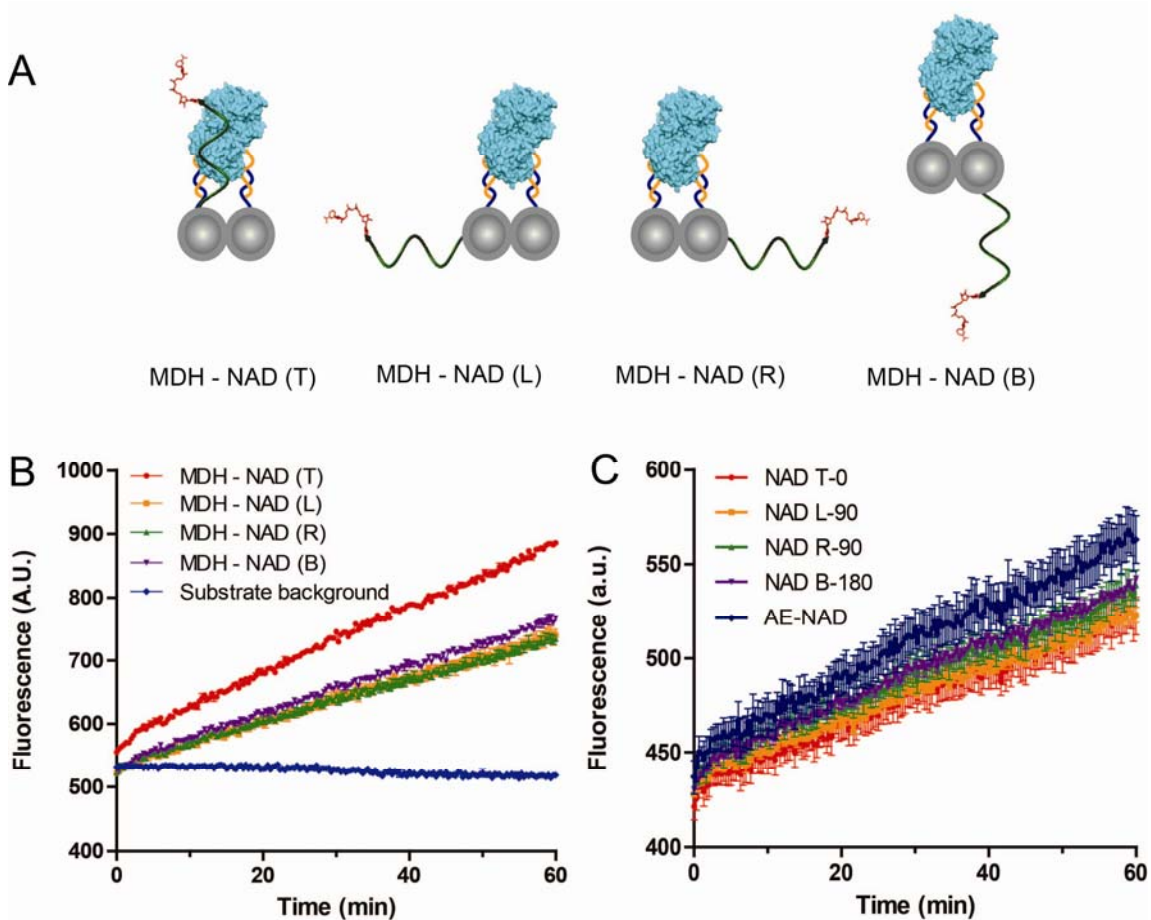


Figure S39. (A) Schematics of MDH- NAD^+ semi-swinging arm assemblies with varying orientations of the anchoring position of the NAD^+ arm relative to that of the protein (defined as “top”): T, parallel orientation on the top of the DNA scaffold; L, NAD^+ arm oriented to the left; R, NAD^+ arm oriented to the right; and B, NAD^+ arm oriented to the bottom. These are viewed from the end of the DNA helices with the protein behind the NAD^+ arm. (B) Raw fluorescence traces of malic acid oxidation catalyzed by MDH- NAD^+ semi-swinging arm assemblies with different anchoring orientations. Assay conditions: 100 nM MDH- NAD^+ semi-swinging arm assembly in the presence of 1 mM malic acid and 500 μM PMS/resazurin in 1× TBS buffer (pH 7.5). (C) Raw fluorescence traces of 100 nM four DNA- NAD^+ that are used in constructing orientation assemblies (shown in figure A), reacting with MDH in the freely diffusing systems. AE- NAD^+ is also tested as control. Assay conditions: 100 nM MDH and DNA- NAD^+ in the presence of 1 mM malic acid and 500 μM PMS/resazurin in 1×TBS buffer (pH 7.5). The activity of all four conjugates is similar and comparable to that of free AE- NAD^+ .

Discussion: The results in Figures S38B, S40B, and 2E-F (main text) indicate that orientation of the NAD⁺ arm parallel to the enzymes on the DNA scaffold gives the highest activity, as expected. Interestingly, even when the NAD⁺ arm is anchored on the opposite side of the DX tile from the protein (bottom), the assemblies possess ~40-70% of the activity of the (top) type structure. This suggests that the flexibility of the swinging arm, together with the likely heterogeneity of protein orientations (i.e., active sites may face in various directions relative to the swinging arm's anchor position), result in residual activity in structures with a variety of swinging arm orientations. Nevertheless, a parallel orientation permits the swinging arm to reach the active sites of the enzymes most effectively, resulting in the highest activity.

Section 9: Characterization of the assembly and activity of G6pDH-NAD⁺-MDH (G-NAD⁺-M) swinging arm structures and stoichiometry-optimized complexes (G-NAD₂⁺-M₂ and G-NAD₄⁺-M₄)

1. Assembly and purification of G6pDH-NAD⁺-MDH swinging arm structures. G-NAD⁺-M swinging arm structures, as well as G6PDH-NAD⁺ and MDH-NAD⁺ semi-swinging arm structures, were purified using size-exclusion FPLC to remove aggregates, incompletely assembled structures and excess proteins. The fractions collected were characterized using native PAGE to confirm the assignments of the FPLC peaks and to check the purity of the samples.

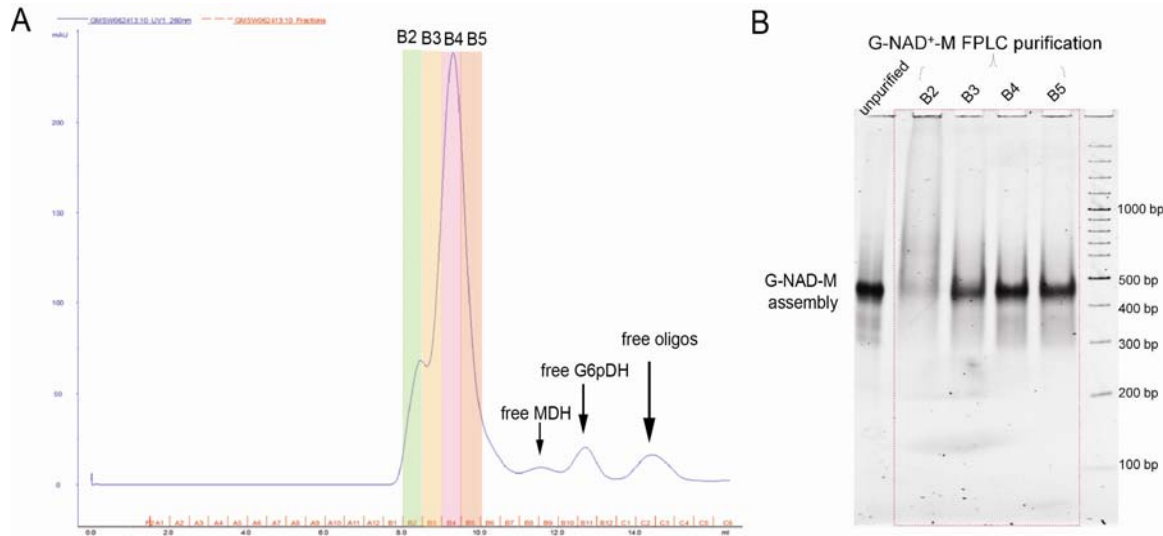


Figure S40. (A) Size-exclusion FPLC purification of fully assembled G6pDH-NAD⁺-MDH swinging arm structures to get rid of excess enzymes and free DNA oligoes. The fractions B2-B5 were collected, representing the fully assembled structure with both the enzymes and the NAD⁺ on the DX tile. (B) Native 3% PAGE characterization the structures collected in size-exclusion FPLC: Fraction B2 contains aggregated structures. Fraction B3 to B5 are the fully assembled swinging arm structures and were used for the activity test (raw data shown in Figure S44). Unpurified swinging arm structure is also shown in the left lane as a control, which contains incomplete assemblies, aggregations and free proteins.

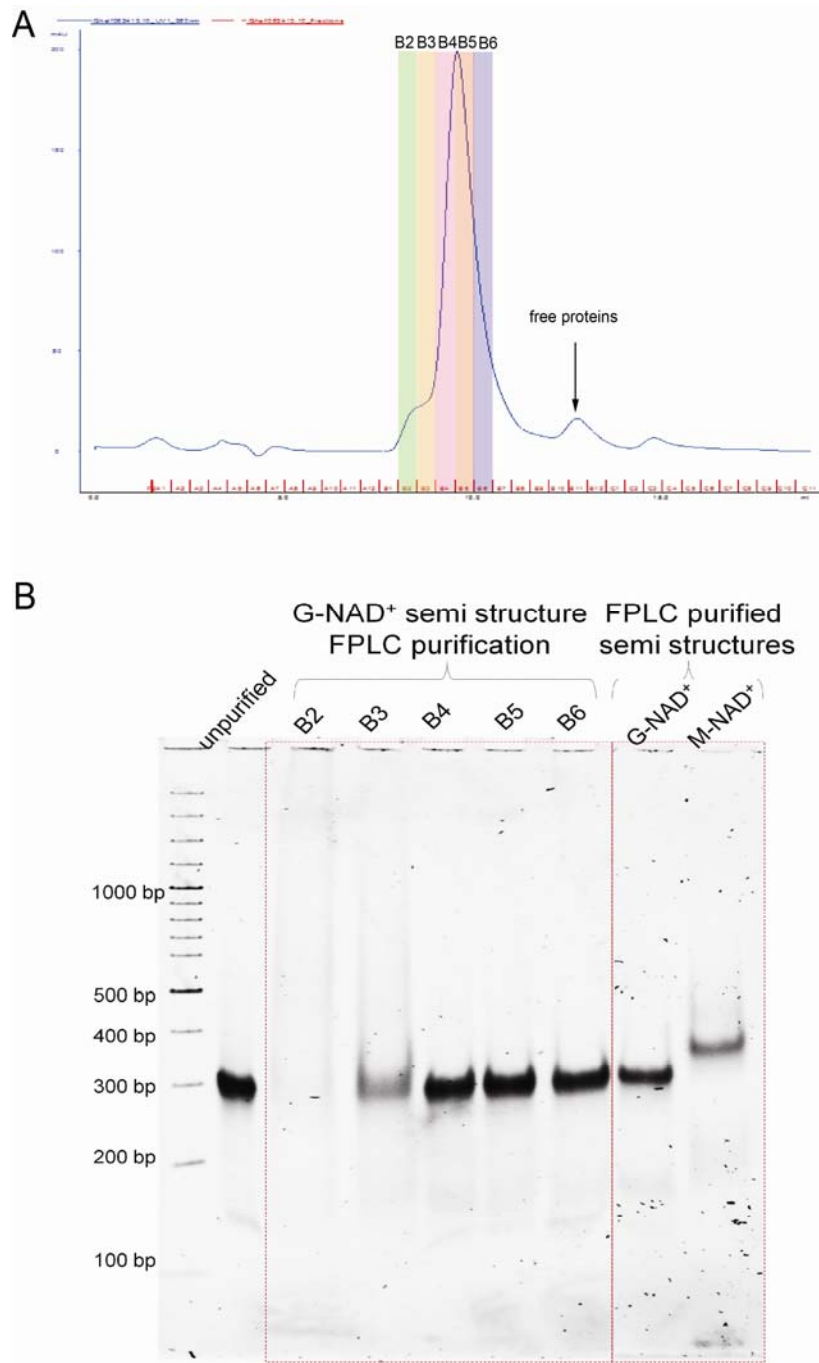


Figure S41. (A) Size-exclusion FPLC purification of G6pDH-NAD⁺ semi-swinging arm structures. Five fractions (B2-B6) were collected. (B) Native 3% PAGE characterization of the fractions collected in size-exclusion FPLC. Fractions B2 and B3 contain aggregated structures (significant smear band). Fraction B4, B5 and B6 contain the purified structure and were used in subsequent activity assays (raw data shown in Figure S44). The two rightmost lanes contain FPLC-purified G6pDH-NAD⁺ and MDH-NAD⁺ semi-swinging arm structures.

2. Raw activity traces of full swinging arm and semi-swinging arm complexes.

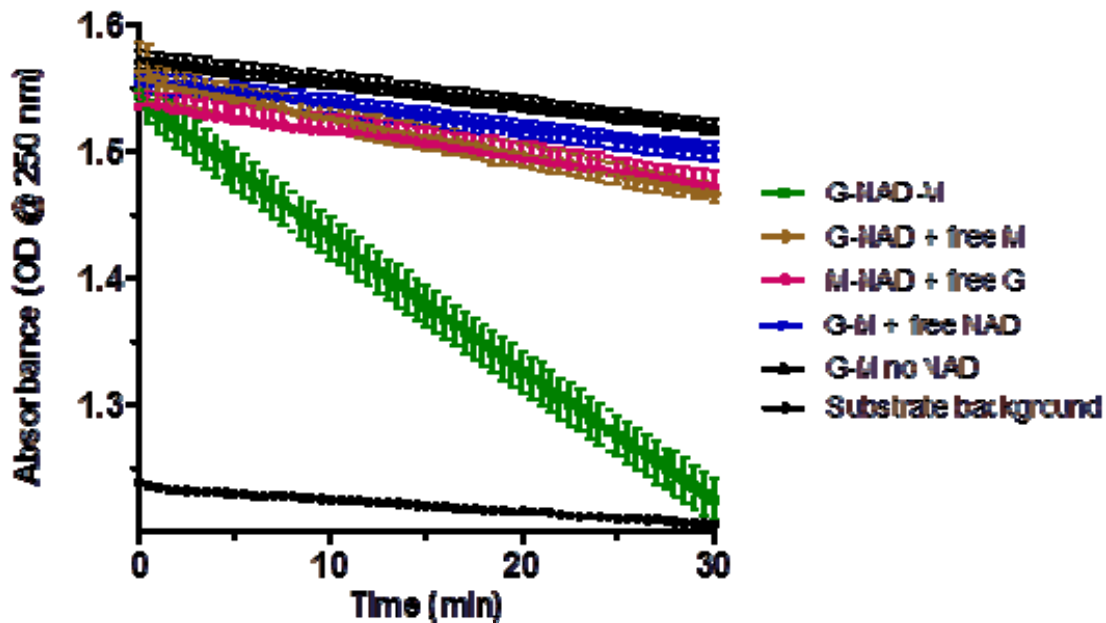


Figure S42. Raw absorbance traces for evaluating the activity of different swinging arm constructs. The normalized relative rates of reaction derived from fitting a straight line to each of these plots are shown in main text Figure 3A. Reaction conditions: 100 nM of the assembled enzyme-DX tile structures or free enzymes, 100 nM free AE-NAD⁺ (when present), 1 mM G6p, and 1 mM OAA in 100 mM HEPES buffer (pH 8). The decrease in absorbance at 250 nm due to conversion of OAA to pyruvate reports on the overall progress of the coupled reactions. Each trace represents the average of three parallel measurements. The full G6pDH-NAD⁺-MDH swinging arm structure shows significantly higher activity than any of the partially assembled structures, which show reaction rates only slightly above the background autocatalysis of OAA. The higher absorbance at 250 nm for the reaction mixtures than that of the substrates alone (1 mM G6p and 1 mM OAA) is due to the presence of NAD⁺, proteins and the DNA tile.

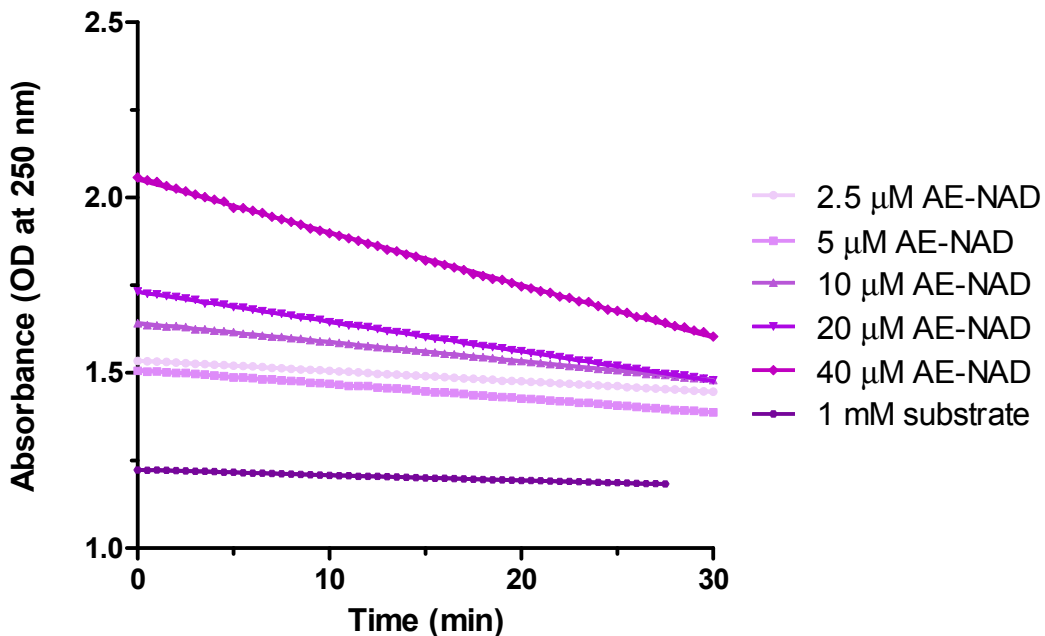


Figure S43. Raw absorbance traces for determining the effective local concentration of NAD⁺ on swinging arm structures by titrating free AE-NAD⁺ into the G6pDH-MDH assembly (lacking the NAD⁺ swinging arm) and comparing the initial rates of reaction to that of the G6pDH-NAD⁺-MDH structure. Assay conditions: 100 nM G6pDH-MDH assemblies with 2.5, 5, 10, 20 or 40 μM free AE-NAD⁺ and 1 mM each of G6p and OAA in 100 mM HEPES buffer (pH 8).

Discussion:

It is remarked in the main text that the effective local concentration of the NAD⁺-coupled swinging arm determined by enzyme catalysis (~20 μM at 7 nm) is significantly lower than the swinging arm concentration estimated from competitive hybridization (~250 μM at 7 nm in Fig. S28B). We have suggested two possible reasons for this discrepancy: (1) the stricter orientational and sterical constraints associated with the binding of tethered NAD⁺ to the active site of a nearby (anchored) enzyme; and (2) the fact that some enzymes or cofactors may be paired together permanently with inactive partners on DNA nanostructures, preventing the formation of an active cascade. As shown in Figure S11, DNA conjugated G6pDH is significantly less active

than unmodified enzyme (> 50 % decrease in activity under the assay conditions); it is thus likely that some of the DNA-conjugated enzymes are wholly or partially inactivated. When these inactivated enzymes are assembled into swinging arm structures, many will permanently pair with active NAD⁺ molecules, resulting in an incomplete cascade. Similarly in Figure S18, the amino-modified NAD⁺ used in this work is less active than unmodified NAD⁺, with a ~ 50% decrease in k_{cat} and ~ 2.5 fold increased K_m for G6pDH on average. This suggests that some amino-modified NAD⁺ or DNA-conjugated NAD⁺ are not active, and may pair with active enzymes and inhibit the catalytic function on the swinging arm structures. Conversely, in a freely diffusing enzyme system, the exchange between enzymes and cofactors happens frequently, and the inactive components can thereby be rapidly replaced by active molecules without inhibiting the entire enzyme/cofactor system. This observation and discussion address one disadvantage of swinging arms and other substrate channeling mechanisms: the malfunction of one assembled component may inhibit the entire multi-enzyme complex. This might be circumvented in part by having redundant copies of enzymes and/or cofactors in a single complex, as in the designs depicted in Fig. 3D.

3. Assembly and characterization of the G6pDH-NAD⁺₄ complex based on a 4×4 DNA tile.

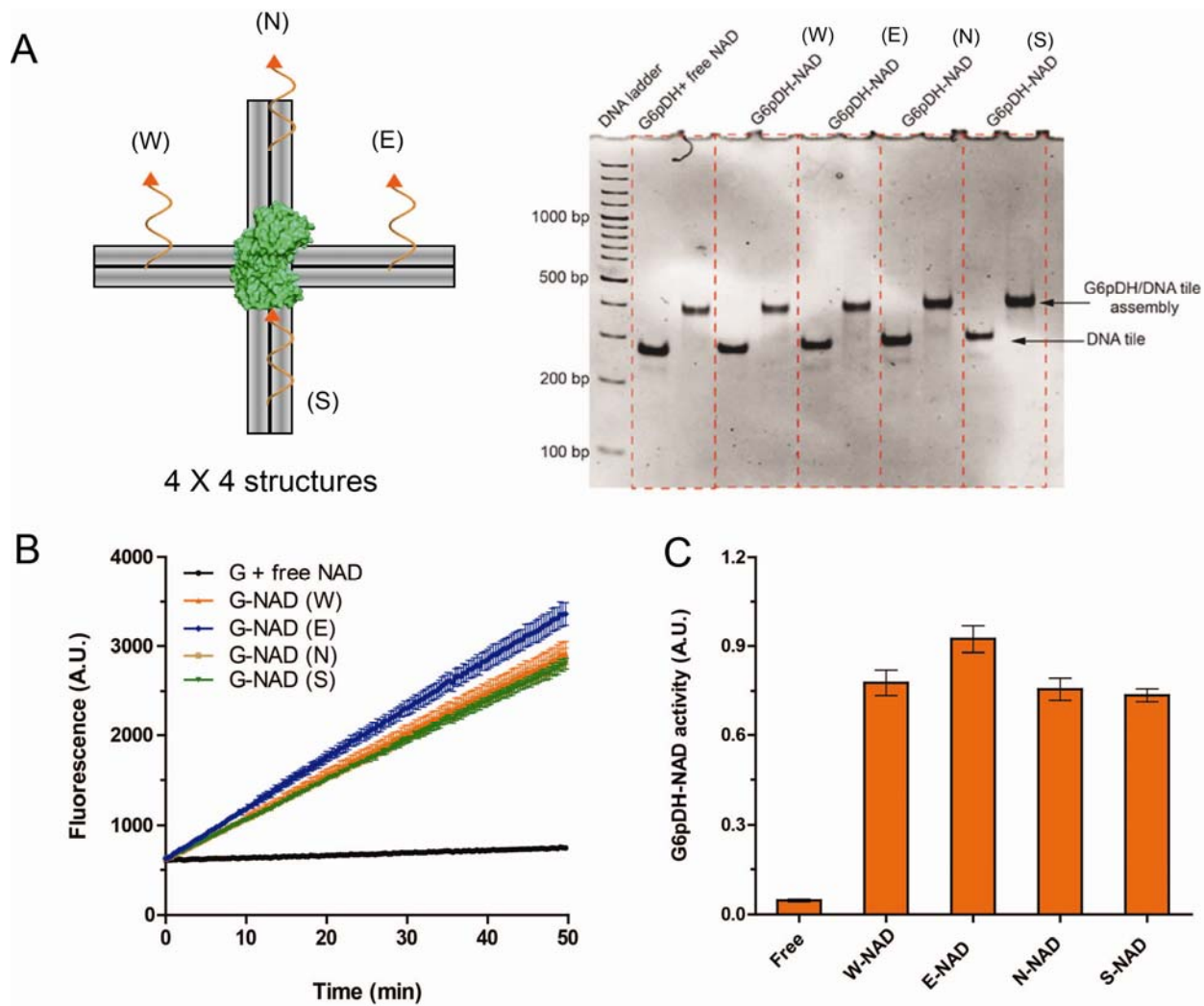


Figure S44. (A) Schematic of G6pDH assembly with four NAD⁺-modified arms on a single 4×4 DNA tile (sequence design shown in **Figure S6**). The right panel shows a native 3% PAGE characterization of G6pDH-NAD⁺ 4×4 tile structures, each containing only one of the four NAD⁺-modified arms (W, E, N, or S). Binding of G6pDH onto the 4×4 tile causes a mobility shift. (B) Activity assay of G6pDH-NAD⁺ 4x4 tile assemblies (each containing only one NAD⁺ arm). (C) Enzymatic activity as determined from the initial velocity of the raw fluorescence traces in (B), evaluated by fitting each trace to a straight line. Assay conditions: 100 nM G6pDH-NAD⁺ 4x4 tile structures, 100 nM free AE-NAD⁺ (when present) are 100 nM, 1 mM G6p, and 500 μM PMA/resazurin in 1×TBS buffer (pH 7.5).

Discussion: The activity measured for each of the constructs shown in Figure S46 is similar, varying within 20%. This suggests that there is no strong preference for a particular position of the swinging arm with respect to the enzyme on the 4×4 DNA tile. This may be due in part to the flexibility of the poly(T)₂₀ arm and (limited) rotational diffusion of the enzyme by its DNA anchors, but also is likely attributable to the random orientation of G6pDH attachment to the DNA tile. The random conjugation of two P-1 DNA probes to G6pDH *via* two of its many surface lysines (more than 10) is expected to yield a mixture of isomers, giving rise to a variety of orientations of the enzyme on the DNA tile. Since the four anchoring positions of the swinging arm on the 4×4 DNA tile are the same distance (7 nm) from the center of the protein anchoring position, the effective local concentration of NAD⁺ is almost equal for all four positions when averaged across all isomers of the enzyme-DX tile complex.

4. Assembly of G6pDH and MDH with 1-4 NAD⁺ swinging arms on the 4×4 DNA tile.

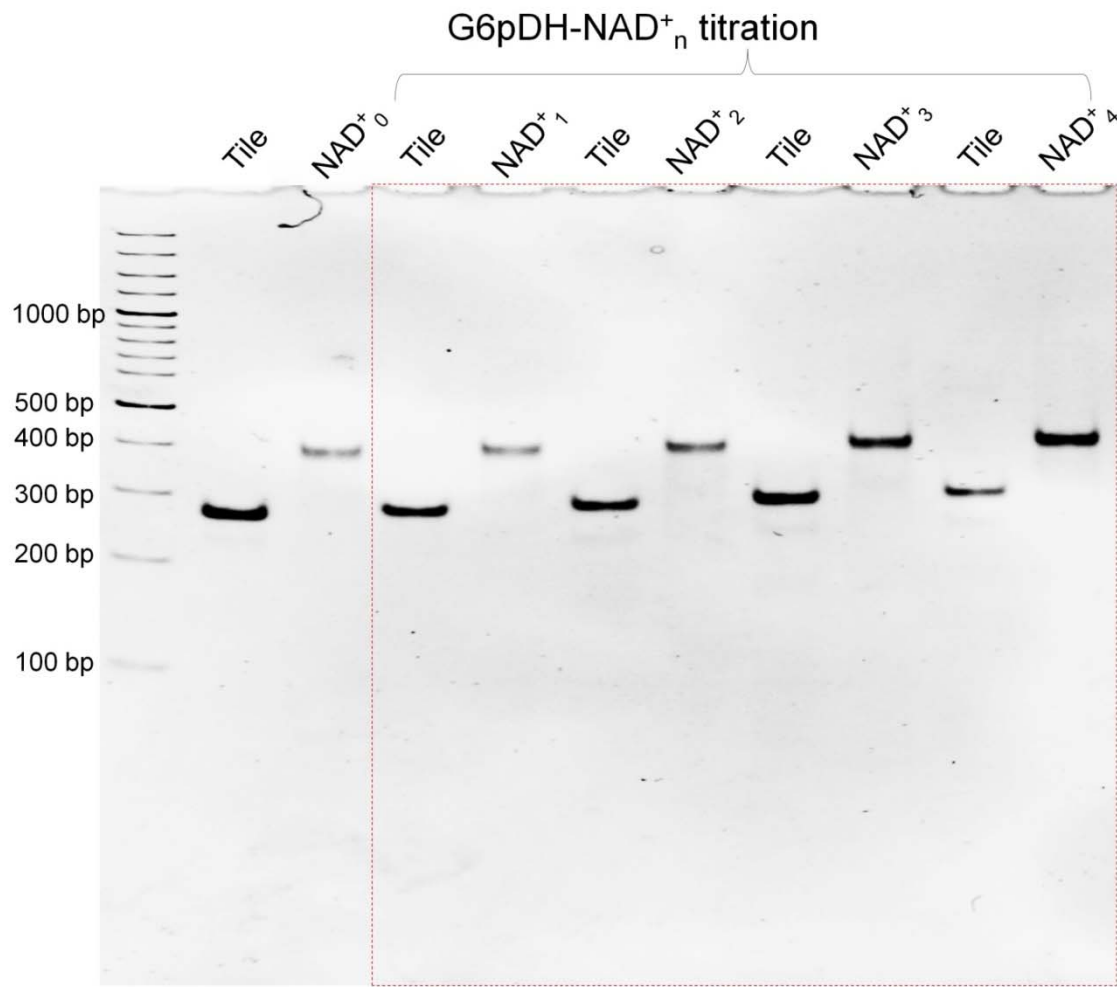


Figure S45. Native 3% PAGE characterization of the assembly of G6pDH-NAD⁺_n (n = 1, 2, 3, 4) structures, in which G6pDH is located in the center of the 4×4 tile and the each arm of the DNA tile carries one NAD⁺ swinging arm (or none). Binding of G6pDH to the DNA tile causes a significant mobility shift, while the binding of each additional NAD⁺ arm causes only a very small decrease in mobility. The gel also indicates that the structures assemble with high yield.

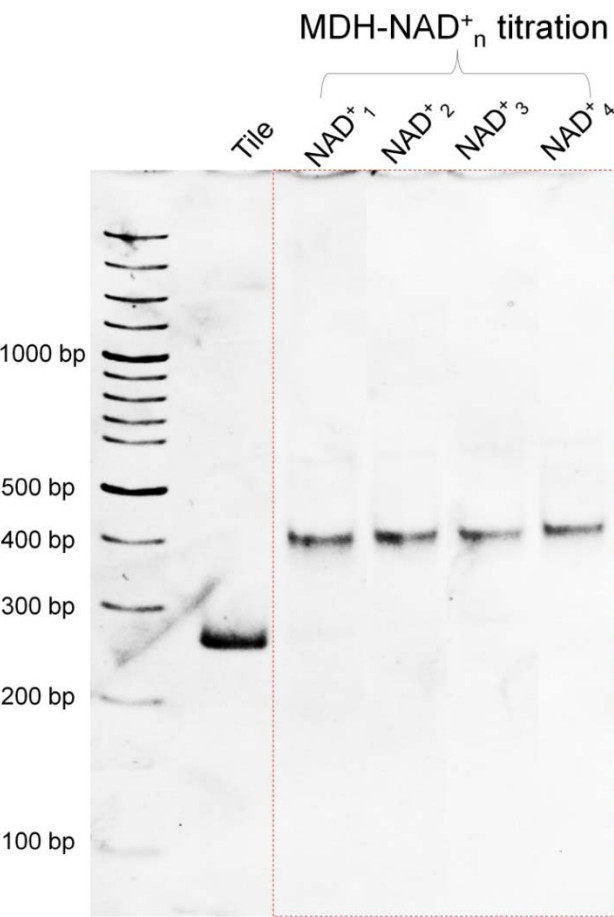


Figure S46. Native 3% PAGE characterization of the assembly of MDH-NAD⁺_n (n = 1, 2, 3, 4) structures, in which MDH is located at the center of the 4×4 tile and each arm of the DNA tile carries one NAD⁺ swinging arm (or none). Binding of MDH to the DNA tile causes a significant gel mobility shift, while the binding of each additional NAD⁺ arm causes only a very small decrease in mobility. The gel also indicates that the structures assemble with high yield.

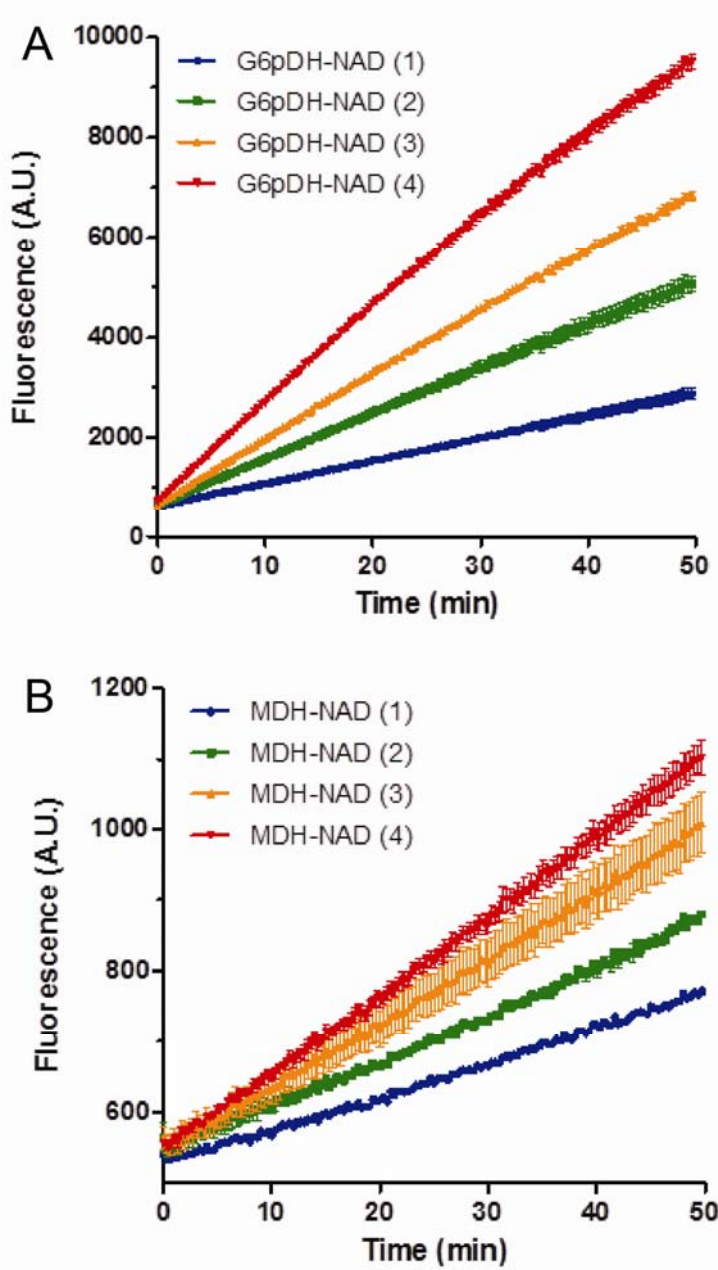


Figure S47. Raw fluorescence traces from reactions catalyzed by G6pDH (A) or MDH (B) with 1-4 NAD⁺ arms on the 4×4 DNA tile. Assay conditions: 100 nM enzyme-DNA assemblies, 1 mM G6p for the G6pDH assay or 1 mM malic acid for the MDH assay, and 500 μM PMS/resazurin in 1×TBS buffer (pH 7.5). The normalized activity of each complex is determined by fitting a straight line to these traces and is shown in main text Figure 3C.

5. Assembly and purification of the G6pDH-NAD⁺₂-MDH₂ complex based on the DX DNA tile.

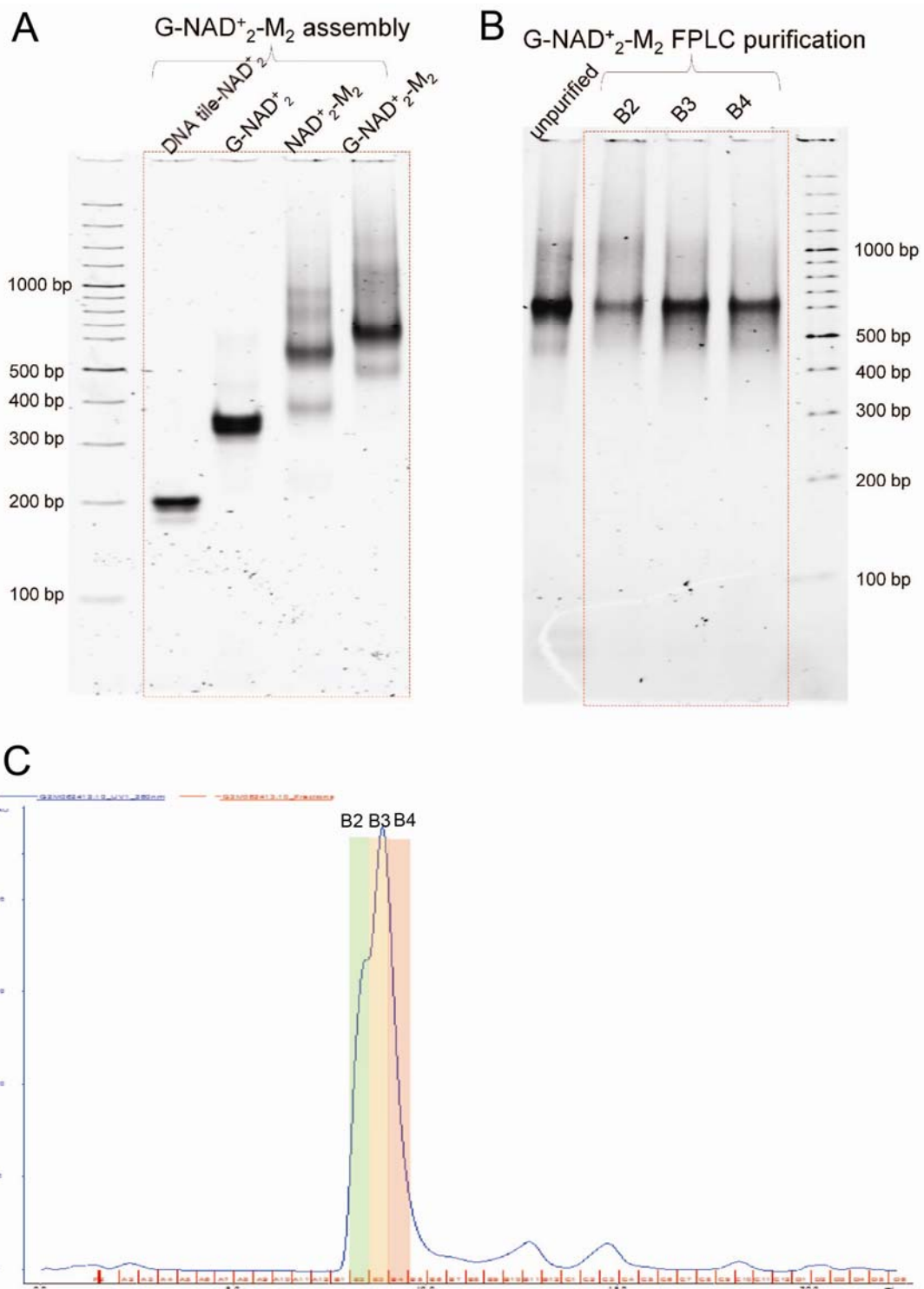


Figure S48. (A) Native PAGE characterization of the assembly of G-NAD⁺₂-M₂ structures on the DX DNA tile (shown in Figure S5 and Figure 3D in the main text). Lanes from left to right: DNA tile with two NAD⁺ arms (DNA tile-NAD⁺₂), DNA tile with G6pDH and two NAD⁺ arms (G-NAD⁺₂), DNA tile with two NAD⁺ arms and two MDH (NAD⁺₂-M), and fully assembled G6pDH-NAD⁺₂-MDH₂ structures (G-NAD⁺₂-M₂). (B) Native PAGE characterization of the fractions collected from size-exclusion FPLC of the fully assembled G-NAD⁺₂-M₂ structures. Fraction B2 contains aggregates; fractions B3 and B4 were used in subsequent activity assays. (C) Chromatogram from the size-exclusion FPLC purification of fully assembled G-NAD⁺₂-M₂ structures, removing excess protein and DNA strands. Three fractions (B2-B4) were collected for the native PAGE characterization shown in (B).

6. Assembly and purification of the G6pDH-NAD⁺₄-MDH₄ complex based on the 4×4 DNA tile.

In this design, the assembly of multiple (1-4) copies of MDH on the 4×4 DNA tile was characterized using PAGE before constructing the complete G6pDH-NAD⁺₄-MDH₄ structure.

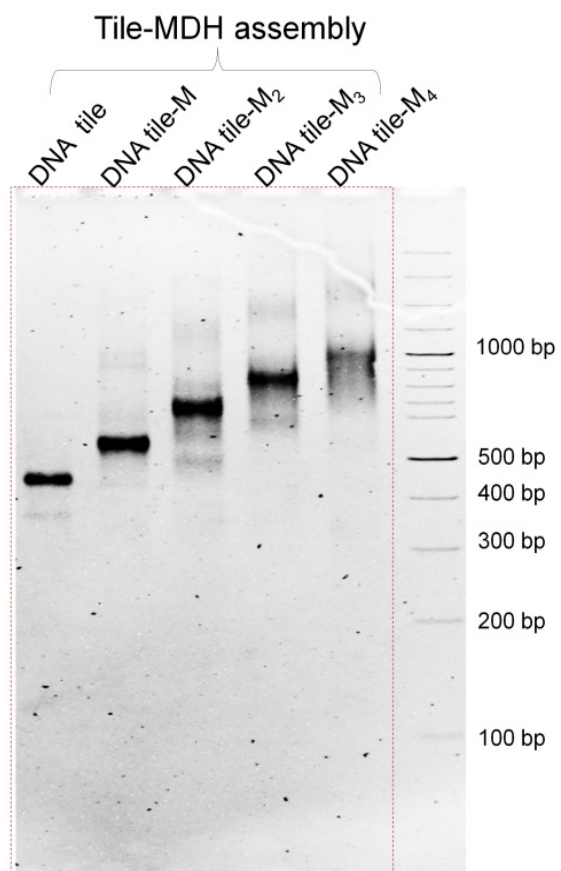


Figure S49. Native PAGE characterization of the assembly of 1-4 copies of MDH on the 4×4 DNA tile. Two capture probes for MDH extend from each of the four arms of the 4×4 DNA tile (see Figure S7). To precisely control the number of MDH assembled on each 4×4 DNA tile, the capture probes for MDH are removed from the appropriate scaffold strands during thermal annealing. Lanes, from left to right: 4×4 DNA tile with 0, 1, 2, 3, and 4 copies of MDH.

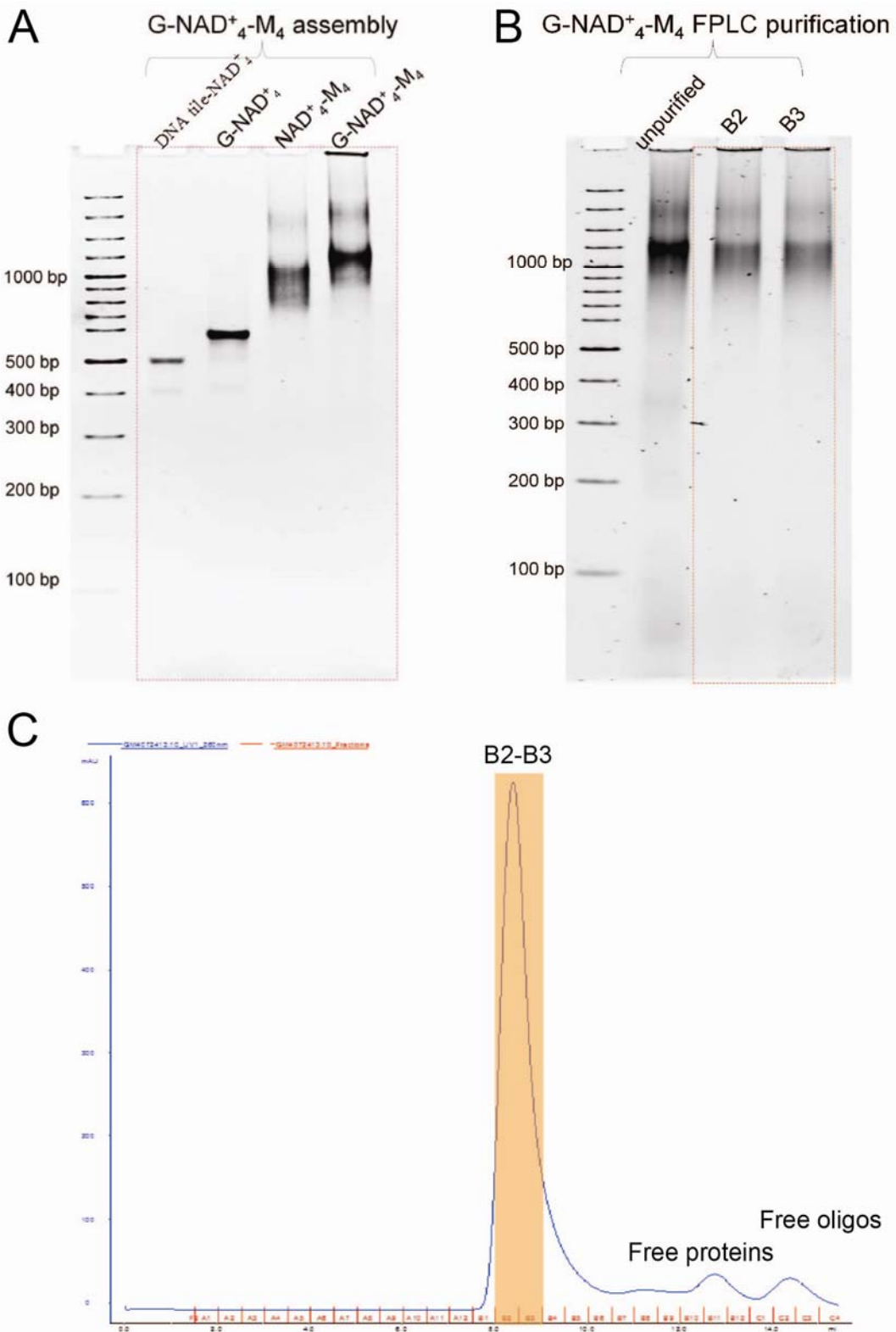


Figure S50. Native PAGE characterization of the assembly of G6pDH-NAD₄-MDH₄ structures and FPLC purification. (A) Native PAGE characterization of the assembly of G-NAD₄-M₄ structures on the 4×4 DNA tile (shown in Figure S7 and Figure 3D in the main text). Lanes from left to right: 4×4 DNA tile with four NAD⁺ arms (DNA tile-NAD⁺₄), G6pDH-NAD⁺₄ (G-NAD⁺₄), NAD⁺₄-MDH₄ (NAD⁺₄-M₄), and fully assembled G6pDH-NAD⁺₄-MDH₄ (G-NAD⁺₄-M₄). (B) Native PAGE characterization of the fractions collected from size-exclusion FPLC of fully assembled G-NAD⁺₄-M₄. Fractions B2 and B3 contained few large aggregates and free proteins, and were combined for use in subsequent activity assays. (C) Chromatogram from size-exclusion FPLC purification of fully assembled G-NAD₄-M₄, removing excess proteins and DNA strands.

7. Raw data for comparison of the activity of assemblies with different G6pDH/MDH ratios.

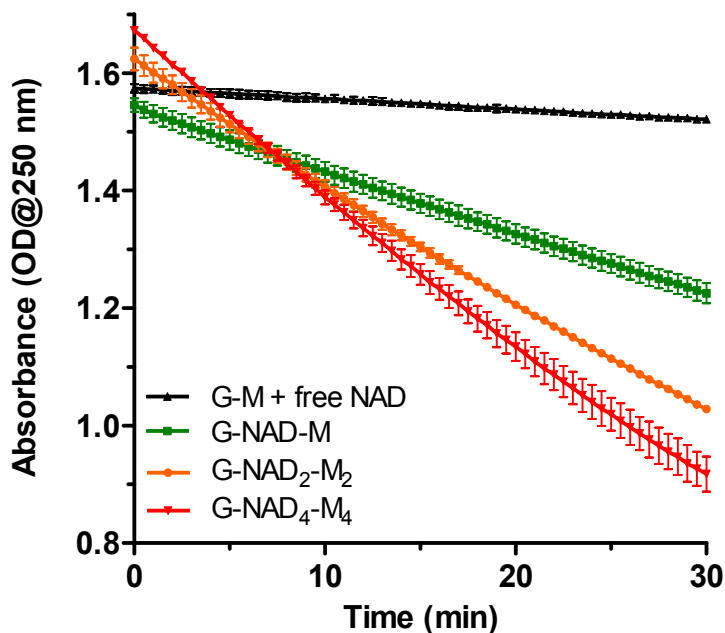


Figure S51. Raw absorbance time traces of reactions catalyzed by each construct. As the number of MDH and NAD⁺ arms increases from 1 to 2 to 4 per G6pDH, the overall activity of the complex increases. The relative activity of each complex, calculated from the slopes of these absorbance time traces, is shown in Figure 3D in the main text. Assay conditions: 100 nM swinging arm assemblies, 1 mM G6p and OAA in 100 mM HEPES (pH 8).

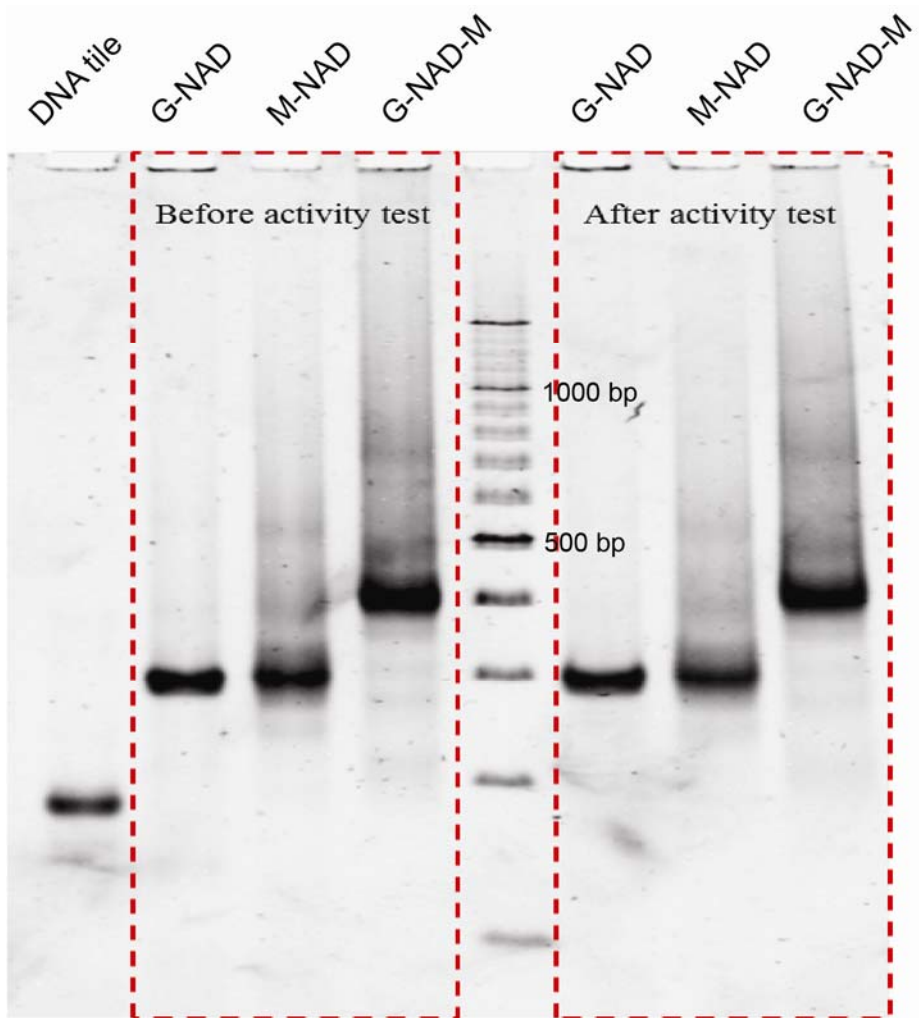


Figure S57.

Figure S52. Native PAGE (3%) characterization of the stability of swinging-arm structures before and after the catalytic reaction. Left: the structures of G-NAD, M-NAD and G-NAD-M before running the reaction. Right: the structures of G-NAD, M-NAD and G-NAD-M after running the reaction. Reaction conditions: 1 mM G6pDH and OAA were incubated with 100 nM enzyme structures for one hour in the pH 7.5 HEPES buffer.

8. Regulation of enzyme complex activity by conversion of the ssDNA arm to dsDNA.

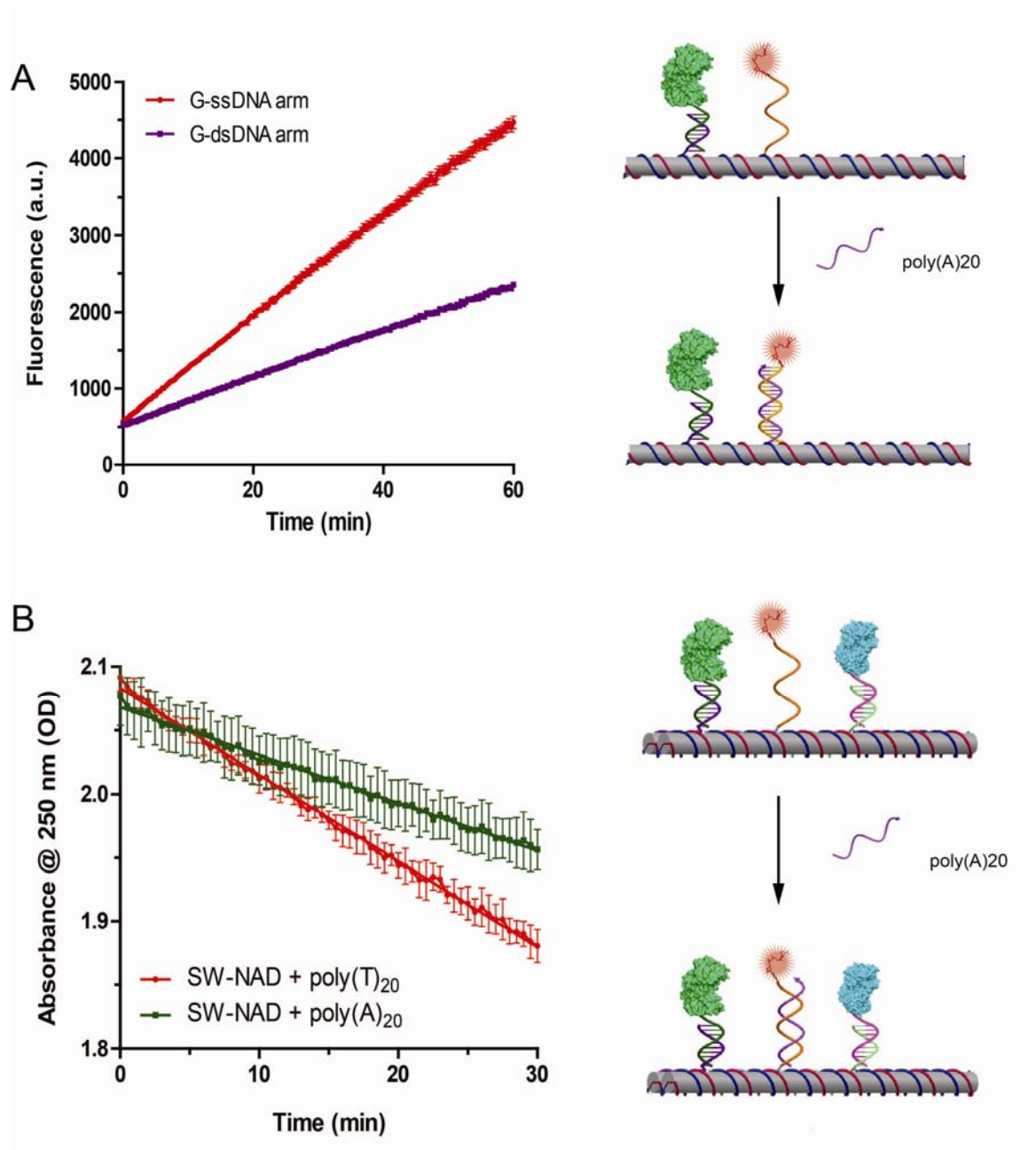


Figure S53. Regulation of enzyme complex activity by conversion of the ssDNA arm to dsDNA. (A) Regulating the activity of the G6pDH-NAD⁺ semi-swinging arm structure by adding a poly(A)₂₀ strand to hybridize with the NAD⁺-poly(T)₂₀ arm. The formation of a double-stranded arm results in a ~50% drop in activities, likely by slowing down the diffusion of NAD⁺ and decreasing the flexibility of the arm (and hence its freedom to explore the space near the enzyme). (B) Regulating the activity of the G6pDH-NAD⁺-MDH swinging arm structures by adding a poly(A)₂₀ strand to hybridize with the NAD⁺-poly(T)₂₀ arm. For control reactions in (A) and (B), an equal concentration of poly(T)₂₀ (which is unable to hybridize with the swinging arm) is added to the sample. Assay conditions: a 10-fold excess of poly(A)₂₀ is added into solution with 100 nM swinging arm complex and incubated for 30 min at room temperature (to allow hybridization to reach equilibrium) before the activity assay. The activity assay conditions are described in Section 7.

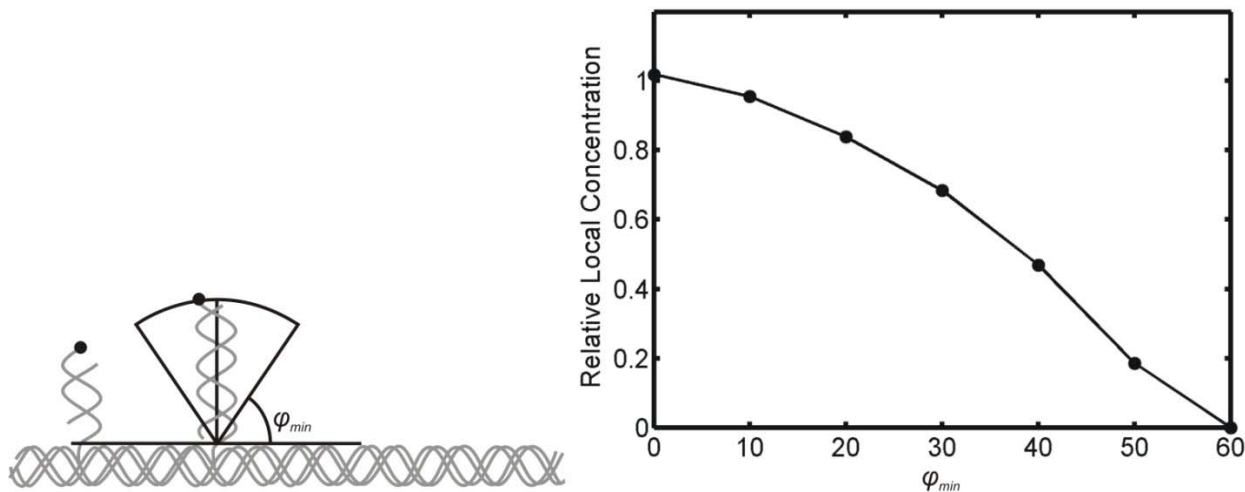


Figure S54. Predicted decrease in local effective concentration with increasing orientational rigidity of a dsDNA arm. When a poly(T)₂₀ swinging arm is hybridized to a poly(A)₂₀ complement, it forms a fully double-stranded arm that is not separated from the DNA tile by a flexible ssDNA linker, and its rotational diffusion is expected to become more hindered. The dsDNA arm is therefore modeled as a rigid rod (contour length \ll persistence length) confined to a spherical section defined by a minimum angle φ_{min} above the plane of the DNA tile and the local NAD⁺ concentration calculated according to the Monte Carlo procedure described on p. S51. While a completely unhindered dsDNA arm ($\varphi_{min} = 0$) is predicted yield nearly the same local concentration of NAD⁺ as the ssDNA arm in the vicinity of the enzyme (Relative Local Concentration ≈ 1), the experimentally determined 30%-50% drop in enzymatic activity (figs. S53 and S55) could be explained by confinement of the dsDNA arm to an angle of $\geq 30\text{--}40^\circ$ above the plane of the tile.

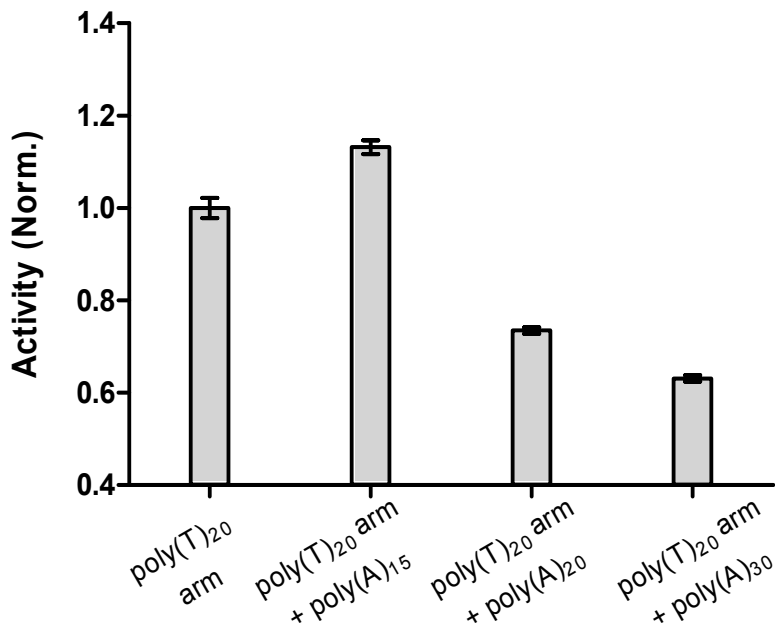


Figure S55. The dependence of swinging arm complex activity on the length of added complementary strands. The activity of the swinging arm decreases as the length of the complements increases, suggesting that the increased rigidity of the double-stranded DNA reduces activity. However, the partially double-stranded arm consisting of poly(T)₂₀ and poly(A)₁₅ is slightly more active (15%) than the single-stranded poly(T)₂₀, suggesting that a partially double-stranded DNA may more effectively present the NAD to the enzyme. The observed effect of double-stranded DNA rigidity on inhibiting the efficient interaction between the enzyme and the cofactor, is consistent with a previous study that the inhibition and activation of an enzyme-inhibitor complex were regulated by switching the linker between an enzyme and an inhibitor from a single-stranded DNA to a double-stranded DNA.¹⁸ Reaction conditions: 100 nM G6pDH-NAD semi-swinging arm structure was incubated with 1 μM poly(A) complementary strands, and assayed with 500 μM resazurin and PMS in pH 7.5 HEPES buffer.

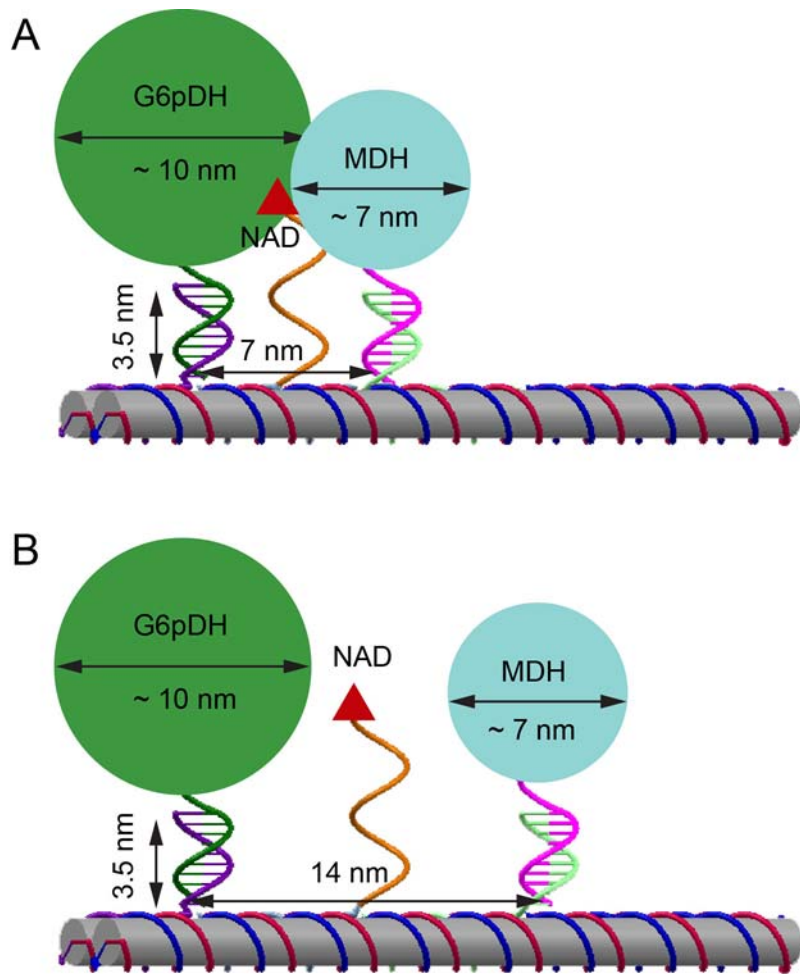
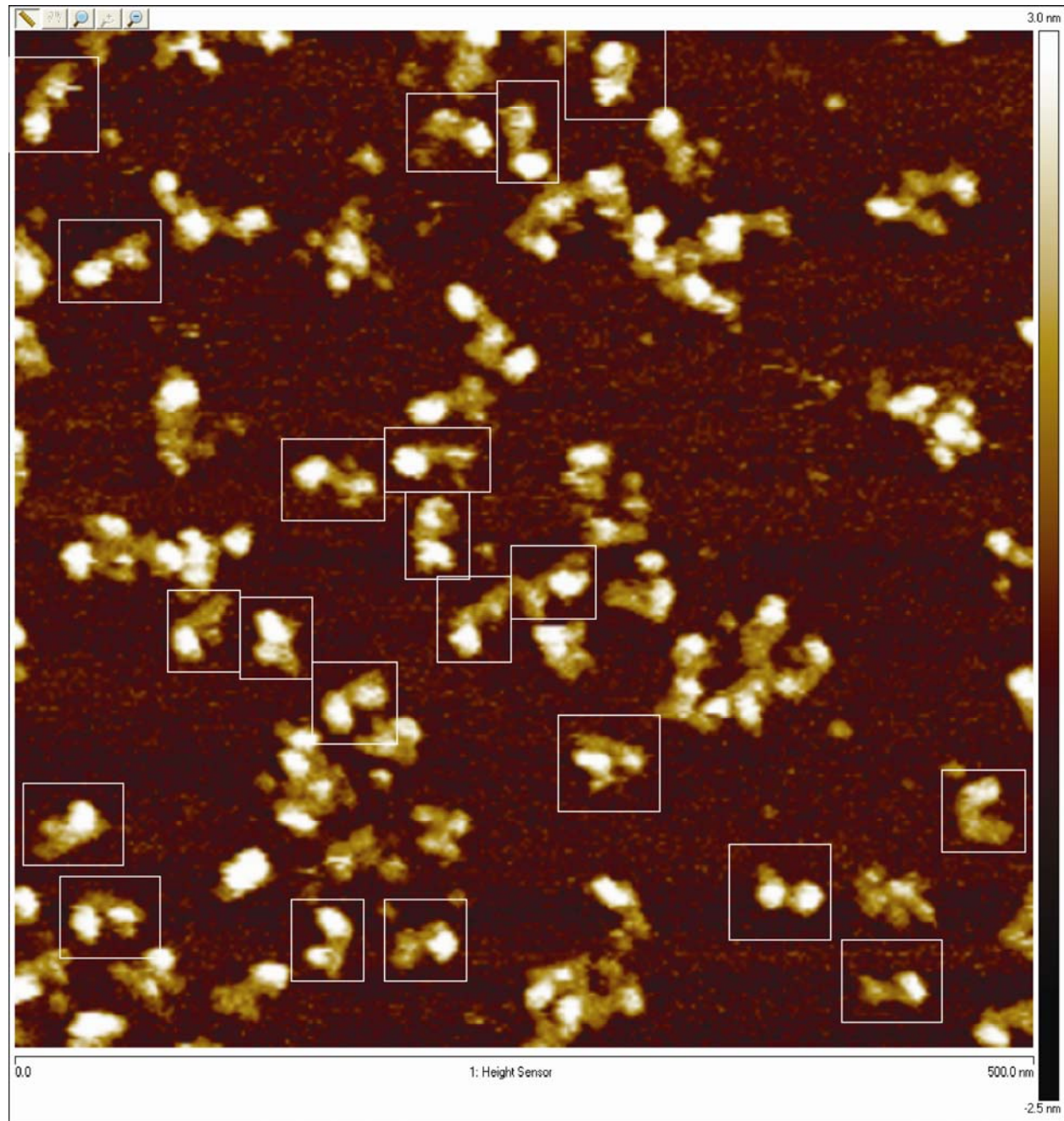


Figure S56. Steric model of G6pDH-NAD-MDH swinging arm structures. Enzymes are anchored to the DNA structures through the hybridization of a short double-stranded DNA (10 bp, ~ 3.5 nm). G6pDH (~ 100 kD) is ~ 10 nm in diameter and MDH (~70 kD) is ~ 7 nm in diameter, according to crystal structures from PDB. (A) At a 7-nm inter-enzyme distance, the two proteins are expected to be in contact (crowded). (B) At a 14-nm inter-enzyme distance, the two proteins are not as crowded, and are thus expected to co-assemble with higher efficiency.

Section 10. AFM images of the fully assembled G6PDH-NAD⁺-MDH swinging arm complex.



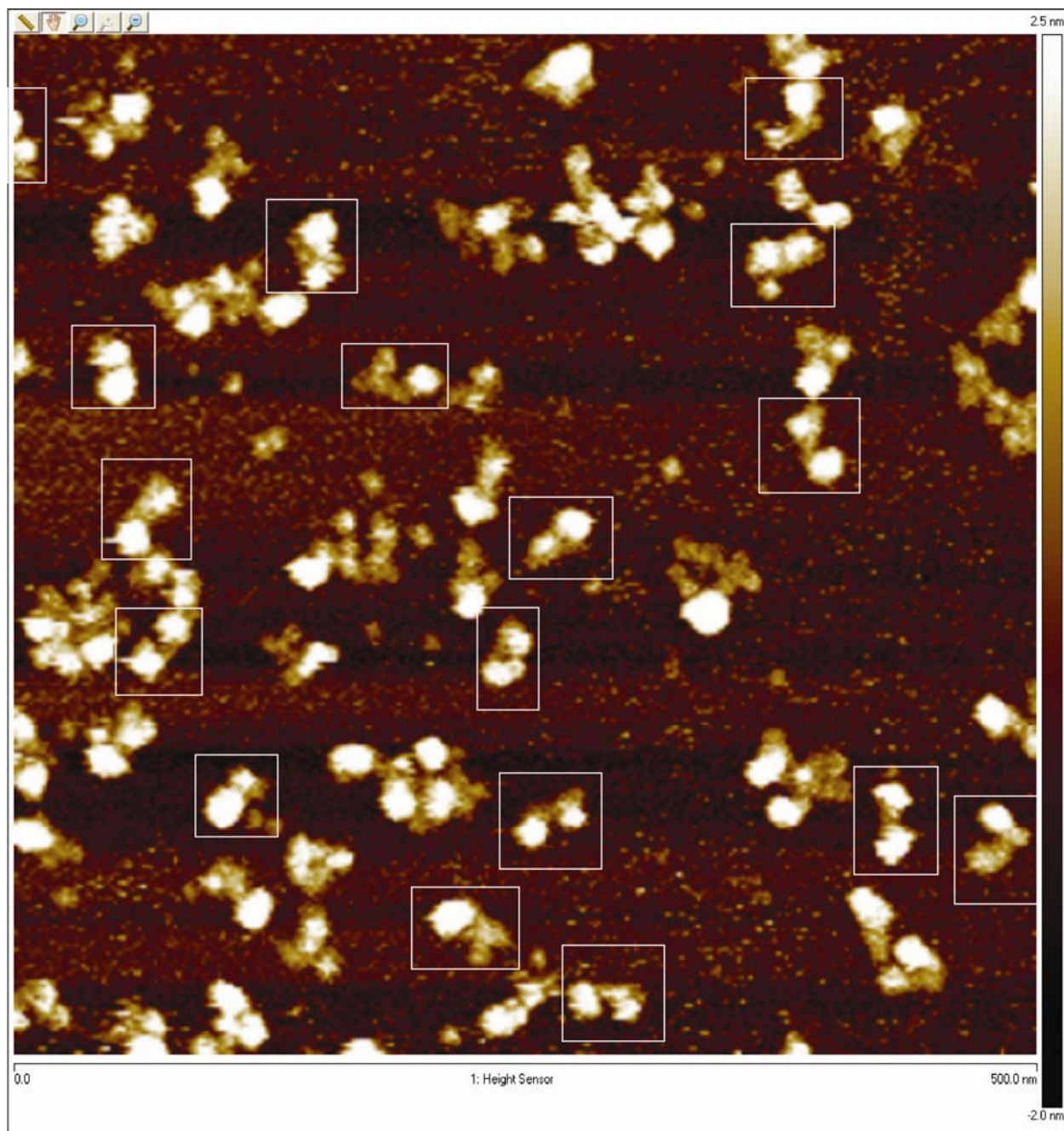


Figure S57. Zoom out AFM images of the fully assembled G6pDH-NAD⁺-MDH swinging arm complex (Figure S3). The AFM images were obtained using a FastScan AFM (Bruker) under aqueous buffer, in Peak Force mode. The thin white boxes highlight correctly assembled, well-separated structures with both of the proteins clearly distinguished (since MDH is larger than G6pDH, one protein appears brighter than the other in the AFM image of most complexes). The DX tile appears as a rod ~30-40 nm long with one protein at each end. The swinging arm (single-stranded poly(T)₂₀ labeled with NAD⁺ at the 5' end) is not resolved. Some aggregates were also

observed. Damage of sample may happen during the AFM imaging process, such as destroyed sample fragments due to strong tip force, overlapped sample deposit and sample aggregation on the mica surface. Thereby, AFM imaging cannot reflect the real yield of structure assembly.

AFM imaging protocol: 2 μ L samples were deposited onto a freshly cleaved mica surface (Ted Pella, Inc.) and left to adsorb for 2 minutes. 80 μ L of 1 x TAE-Mg²⁺ buffer was added to the sample and 2 μ L 100 mM Ni²⁺ was added to enhance DNA adsorption on mica. Extra 40 μ L of 1 x TAE-Mg²⁺ buffer was deposited to liquid cell. The samples were scanned using SCANASYST-FLUID⁺ probe (Bruker, Inc.) in “Scanasyst in fluid” mode using a FastScan AFM (Dimension FastScan, Bruker Corporation).

References

1. P. Rowland, A. K. Basak, S. Gover, H. R. Levy, M. J. Adams, The three-dimensional structure of glucose 6-phosphate dehydrogenase from Leuconostoc mesenteroides refined at 2.0 Å resolution. *Structure* **2**, 1073 (1994).
2. A. D. M. Chapman, A. Cortés, T. R. Dafforn, A. R. Clarke, R. L. Brady, Structural basis of substrate specificity in malate dehydrogenases: crystal structure of a ternary complex of porcine cytoplasmic malate dehydrogenase, α-Ketomalonate and TetrahydNAD. *Journal of Molecular Biology* **285**, 703 (1999).
3. J. Fu, M. Liu, Y. Liu, N. W. Woodbury, H. Yan, Interenzyme substrate diffusion for an enzyme cascade organized on spatially addressable DNA nanostructures. *Journal of the American Chemical Society* **134**, 5516 (2012).
4. M. Liu *et al.*, A DNA tweezer-actuated enzyme nanoreactor. *Nat Commun* **4**, 2127 (2013).
5. C. E. Aitken, R. A. Marshall, J. D. Puglisi, An Oxygen Scavenging System for Improvement of Dye Stability in Single-Molecule Fluorescence Experiments. *Biophysical journal* **94**, 1826 (2008).
6. A. Johnson-Buck, J. Nangreave, S. Jiang, H. Yan, N. G. Walter, Multifactorial Modulation of Binding and Dissociation Kinetics on Two-Dimensional DNA Nanostructures. *Nano Letters* **13**, 2754 (2013/06/12, 2013).
7. M. Blanco, N. G. Walter, in *Methods in Enzymology*, N. G. Walter, Ed. (Academic Press, 2010), vol. 472, pp. 153-178.
8. S. Swillens, Interpretation of binding curves obtained with high receptor concentrations: practical aid for computer analysis. *Molecular Pharmacology* **47**, 1197 (1995).
9. P. J. Munson, D. Rodbard, An Exact Correction to the “Cheng-Prusoff” Correction. *Journal of Receptors and Signal Transduction* **8**, 533 (1988).
10. C. Yung-Chi, W. H. Prusoff, Relationship between the inhibition constant (K_i) and the concentration of inhibitor which causes 50 per cent inhibition (I_{50}) of an enzymatic reaction. *Biochemical Pharmacology* **22**, 3099 (1973).
11. N. Metropolis, A. W. Rosenbluth, M. N. Rosenbluth, A. H. Teller, E. Teller, Equation of State Calculations by Fast Computing Machines. *The Journal of Chemical Physics* **21**, 1087 (1953).
12. S. P. Meisburger *et al.*, Polyelectrolyte properties of single stranded DNA measured using SAXS and single molecule FRET: Beyond the wormlike chain model. *Biopolymers*, (2013).
13. H. Chen *et al.*, Ionic strength-dependent persistence lengths of single-stranded RNA and DNA. *Proceedings of the National Academy of Sciences* **109**, 799 (January 17, 2012, 2012).
14. L. P. Candeias *et al.*, The catalysed NADH reduction of resazurin to resorufin. *Journal of the Chemical Society, Perkin Transactions* **2**, 2333 (1998).
15. J. V. Rund, K. G. Claus, Ligand effects on the rate of metal-ion-catalyzed decarboxylation of dimethyloxalacetic acid. *Journal of the American Chemical Society* **89**, 2256 (1967).
16. O. Lockridge, V. Massey, P. A. Sullivan, Mechanism of Action of the Flavoenzyme Lactate Oxidase. *Journal of Biological Chemistry* **247**, 8097 (1972).
17. K. J. Reszka, B. A. Wagner, C. P. Burns, B. E. Britigan, Effects of peroxidase substrates on the Amplex red/peroxidase assay: Antioxidant properties of anthracyclines. *Analytical Biochemistry* **342**, 327 (2005).

18. A. Saghatelian, K. M. Guckian, D. A. Thayer, M. R. Ghadiri, DNA Detection and Signal Amplification via an Engineered Allosteric Enzyme. *Journal of the American Chemical Society* **125**, 344 (2003).